Innovative interfaces for motor assessment

Department of Electrical and Information Engineering
ELECTRICAL AND INFORMATION ENGINEERING
Ph.D. Program

SSD: IBIO-01/A - BIOENGINEERING
SSD: IINF-04/A - AUTOMATION

Final Dissertation

Innovative interfaces for motor assessment

by

Vladimiro Suglia

Supervisors:
Prof. Vitoantonio Bevilacqua, Ph.D.
Prof. David Naso, Ph.D.

Co-supervisors:
Eng. Domenico Buongiorno, Ph.D.
Dr. Cristian Camardella, Ph.D.

Coordinator of Ph.D. Program:
Prof. Mario Carpentieri, Ph.D.

La ricerca è stata realizzata con il cofinanziamento dell'Unione europea - **POC Puglia 2014-2020 – Asse X - Azione 10.4 "Interventi volti a promuovere la ricerca e per l'istruzione universitaria". Approvazione Avviso pubblico n. 1/POC/2021 "Dottorati di ricerca in Puglia XXXVII Ciclo"**

Course n°37, 01/11/2021 - 31/10/2024

Politecnico di Bari

LIBERATORIA PER L'ARCHIVIAZIONE DELLA TESI DI DOTTORATO

Al Magnifico Rettore
del Politecnico di Bari

Il/~~la~~ sottoscritto/~~a~~ SUGLIA VLADIMIRO nato/~~a~~ a DNIPROPETROVSK (UCRAINA) il 28/12/1996

residente a MOTTOLA (TA) in via ALDO MORO, 42 e-mail vladimiro.suglia@poliba.it

iscritto al 3° anno di Corso di Dottorato di Ricerca in ELECTRICAL AND INFORMATION ENGINEERING ciclo XXXVII

ed essendo stato ammesso a sostenere l'esame finale con la prevista discussione della tesi dal titolo:

INNOVATIVE INTERFACES FOR MOTOR ASSESSMENT

DICHIARA

1) di essere consapevole che, ai sensi del D.P.R. n. 445 del 28.12.2000, le dichiarazioni mendaci, la falsità negli atti e l'uso di atti falsi sono puniti ai sensi del codice penale e delle Leggi speciali in materia, e che nel caso ricorressero dette ipotesi, decade fin dall'inizio e senza necessità di nessuna formalità dai benefici conseguenti al provvedimento emanato sulla base di tali dichiarazioni;
2) di essere iscritto al Corso di Dottorato di ricerca ELECTRICAL AND INFORMATION ENGINEERING ciclo XXXVII, corso attivato ai sensi del "*Regolamento dei Corsi di Dottorato di ricerca del Politecnico di Bari"*, emanato con D.R. n.286 del 01.07.2013;
3) di essere pienamente a conoscenza delle disposizioni contenute nel predetto Regolamento in merito alla procedura di deposito, pubblicazione e autoarchiviazione della tesi di dottorato nell'Archivio Istituzionale ad accesso aperto alla letteratura scientifica;
4) di essere consapevole che attraverso l'autoarchiviazione delle tesi nell'Archivio Istituzionale ad accesso aperto alla letteratura scientifica del Politecnico di Bari (IRIS-POLIBA), l'Ateneo archivierà e renderà consultabile in rete (nel rispetto della Policy di Ateneo di cui al D.R. 642 del 13.11.2015) il testo completo della tesi di dottorato, fatta salva la possibilità di sottoscrizione di apposite licenze per le relative condizioni di utilizzo (di cui al sito http://www.creativecommons.it/Licenze), e fatte salve, altresì, le eventuali esigenze di "embargo", legate a strette considerazioni sulla tutelabilità e sfruttamento industriale/commerciale dei contenuti della tesi, da rappresentarsi mediante compilazione e sottoscrizione del modulo in calce (Richiesta di embargo);
5) che la tesi da depositare in IRIS-POLIBA, in formato digitale (PDF/A) sarà del tutto identica a quelle **consegnate**/inviate/da inviarsi ai componenti della commissione per l'esame finale e a qualsiasi altra copia depositata presso gli Uffici del Politecnico di Bari in forma cartacea o digitale, ovvero a quella da discutere in sede di esame finale, a quella da depositare, a cura dell'Ateneo, presso le Biblioteche Nazionali Centrali di Roma e Firenze e presso tutti gli Uffici competenti per legge al momento del deposito stesso, e che di conseguenza va esclusa qualsiasi responsabilità del Politecnico di Bari per quanto riguarda eventuali errori, imprecisioni o omissioni nei contenuti della tesi;
6) che il contenuto e l'organizzazione della tesi è opera originale realizzata dal sottoscritto e non compromette in alcun modo i diritti di terzi, ivi compresi quelli relativi alla sicurezza dei dati personali; che pertanto il Politecnico di Bari ed i suoi funzionari sono in ogni caso esenti da responsabilità di qualsivoglia natura: civile, amministrativa e penale e saranno dal sottoscritto tenuti indenni da qualsiasi richiesta o rivendicazione da parte di terzi;
7) che il contenuto della tesi non infrange in alcun modo il diritto d'Autore né gli obblighi connessi alla salvaguardia di diritti morali od economici di altri autori o di altri aventi diritto, sia per testi, immagini, foto, tabelle, o altre parti di cui la tesi è composta.

Luogo e data BARI, 09/01/2025 Firma Vladimiro Suglia

Il/~~La~~ sottoscritto, con l'autoarchiviazione della propria tesi di dottorato nell'Archivio Istituzionale ad accesso aperto del Politecnico di Bari (POLIBA-IRIS), pur mantenendo su di essa tutti i diritti d'autore, morali ed economici, ai sensi della normativa vigente (Legge 633/1941 e ss.mm.ii.),

CONCEDE

- al Politecnico di Bari il permesso di trasferire l'opera su qualsiasi supporto e di convertirla in qualsiasi formato al fine di una corretta conservazione nel tempo. Il Politecnico di Bari garantisce che non verrà effettuata alcuna modifica al contenuto e alla struttura dell'opera.
- al Politecnico di Bari la possibilità di riprodurre l'opera in più di una copia per fini di sicurezza, back-up e conservazione.

Luogo e data BARI, 09/01/2025 Firma Vladimiro Suglia

Department of Electrical and Information Engineering
ELECTRICAL AND INFORMATION ENGINEERING
Ph.D. Program

SSD: IBIO-01/A - BIOENGINEERING
SSD: IINF-04/A - AUTOMATION

Final Dissertation

Innovative interfaces for motor assessment

by

Vladimiro Suglia

Referees:
Prof. Loredana Zollo, Ph.D.
Dr. Daniele Leornadis, Ph.D.

Supervisors:
Prof. Vitoantonio Bevilacqua, Ph.D.
Prof. David Naso, Ph.D.

Co-supervisors:
Eng. Domenico Buongiorno, Ph.D.
Dr. Cristian Camardella, Ph.D.

Coordinator of Ph.D. Program:
Prof. Mario Carpentieri, Ph.D.

La ricerca è stata realizzata con il cofinanziamento dell'Unione europea - **POC Puglia 2014-2020 – Asse X - Azione 10.4 "Interventi volti a promuovere la ricerca e per l'istruzione universitaria". Approvazione Avviso pubblico n. 1/POC/2021 "Dottorati di ricerca in Puglia XXXVII Ciclo"**

Course n°37, 01/11/2021 - 31/10/2024

Acknowledgements

The Ph.D. can be described as a life-changing and challenging experience that I would not have been able to accomplish without the support and guidance I received.

At the end of this academic journey the acknowledgments, besides being a right act, become a personal pleasure. Hence, I would like to thank my Ph.D. supervisors, Prof. Vitoantonio Bevilacqua and Prof. David Naso, together with my co-supervisors, Ing. Domenico Buongiorno and Ing. Cristian Camardella. Their invaluable expertise and disposability allowed me to successfully work on such interesting thematics.

A further gratitude is to be addressed to all my co-authors, who I was pleased to be accompained by and work with.

Abstract

Motor abilities may be reduced in different conditions, such as neuromotor diseases, the physiological aging, or work-related musculoskeletal disorders. In the clinical realm, motor assessment is useful to measure the severity level, thus supporting physicians' decision for diagnostic, prognostic, and rehabilitative purposes; on the other hand, an objective evaluation of the motor performance could allow for recording the exertion perceived by the subject while executing an industrial task.

However, the clinical scales may suffer from subjectivity, since they are observation-based and related to the specific background of different clinicians; the perceived exertion is conventionally estimated by self-ratings, which may be biased by the user's psychology. Therefore, quantitative and objective measurement of motor abilities are needed to pursue more generalizable outcomes in both clinical and occupational applications.

The purpose of this Ph.D. thesis is to illustrate the research works carried out during the conceptualization, design, implementation, and validation of frameworks for the quantitative assessment of motor capabilities by means of innovative interfaces based on serious game, deep-learning methods, and robotic exoskeletons.

Serious games promote the engagement of the experimental subjects, thus keeping them motivated during the execution of multiple repetitions of the experimental tasks. Deep-Learning models allow for the automatic recognition of motor patterns from raw data for a variety of applications, including human activity recognition and pathological gait recognition. Robotic exoskeletons can support humans in the execution of repetitive and exhausting motor tasks, thus preventing the injuries connected with work-related musculoskeletal disorders.

The applications considered span from visuomotor adaptation to activity recognition and power augmentation. Tasks under consideration concerned the locomotion on a treadmill while controlling a virtual avatar, the execution of activities of daily living, as well as static and dynamic lifting tasks that are typical of an industrial scenario.

A paucity has been found in the different domains of the scientific literature to which the works presented in this thesis belong. As regards visuomotor adaptation, a few works implemented SGs to elicit sensorimotor learning in children during a walking task; therefore,

more investigations are needed to perform a SG-aided evaluation of visuomotor adaptation capabilities of people in developmental age during locomotion tasks. With regards to human activity recognition, a minority of studies trained DL models with inertial data related to a separate execution of human motor actions and tested them with data acquired during an uninterrupted execution of the same activities; furthermore, there exist a few works exploiting simulated gait disorders to train DL models for recognizing pathological gaits. In the field of occupational exoskeletons, a gap has been found about the validation of such robotic devices with motor tasks resembling those of an industrial scenario with both conventional electromyographic measures and innovative methods based on graph theory.

Therefore, the technical contributions of this thesis include the conceptualization of a locomotor task for the evaluation of visuomotor adaptation based on serious game; the validation of a framework based on deep-learning for the recognition of human activities executed in an uninterrupted sequence; the preliminary validation of a similar workflow addressing the recognition of mimicked gait disorders; the validation of an occupational exoskeleton assisting humans during industrial-like motor tasks by means of both traditional electromyographic measures and innovative approaches based on muscle networks.

This thesis work is organized into two parts, each of which is divided in sections including an introduction and the works belonging to the specific context. More in detail, Chapter 1 is focused on applications for clinical purposes, giving an introduction of the objective and the technical contribution of the thesis in such context. Therefore, Section 1.2 describes the contributions proposed in the context of visuomotor adaptation assessment based on serious game, together with the related state-of-the-art. Sections 1.3 and 1.4 present the scientific literature and the contributions proposed in the context of activity recognition, concerning the classification of human motor actions performed continuously and pathological walking patterns simulated by healthy subjects, respectively. On the other hand, Chapter 2 is focused on applications for occupational purposes, giving an introduction of the objective and the technical contribution of the thesis in such context. Hence, Sections 2.2 and 2.3 report the state-of-art and the contributions proposed in the realm of the validation of occupational exoskeleton with conventional electromyographic metrics and functional connectivity analysis based on muscle networks, respectively. Lastly, final remarks and considerations are drawn in Chapter 3.

Table of contents

List of figures

List of tables

Chapter 1

Applications for clinical purposes

1.1 Introduction

Motor abilities have been found to be reduced in case of such pathologies as Parkinson's disease (PD) and Alzheimer's disease (AD), as well as the physiological aging, due to high concentration of iron in brain subregions (e.g., subthalamic nucleus, substantia nigra, red nucleus) [1].

Clinical measures are widely utilized for the assessment of pathology severity, but they suffer from different drawbacks, starting from the subjectivity of their outcomes, since they are typically based on observations [2, 3] and face-to-face questioning [4]; moreover, the different clinicians' backgrounds and experiences might lead to different interpretations of the used scale [5]. This issue is even exacerbated in specific cases, such as cognitive skills like the Sense of Agency (SoA), which is the ability to recognize oneself as the agent of an action (e.g., a motor action) [6]. In fact, due to the retrospective nature of SoA, a cognitive bias occurs and leads to its overestimation when participants are asked to self-quantify this awareness in an explicit way [7]. This could negatively impact in the assessment of the severity of pathologies, such as the cerebral palsy, which is associated to the SoA [8, 9]. Hence, quantitative evaluation of motor abilities aims at a higher outcome generalizability and supports clinicians by saving the time for data collection and consequently prioritizing the decision-making process [1].

Remarkably, the assessment of the subject's performance can benefit from the development of an effective framework oriented to the recognition of the executed motor actions, which lies in the field of human activity recognition (HAR) [10]. For this purpose, the exploitation of Deep Learning (DL) models allows for the automatic learning of patterns from

raw data, thus avoiding time-demanding feature engineering operations on domain-specific knowledge [11].

1.1.1 Objective and Research Question

Innovative interfaces integrating either SGs or DL methods have allowed for the design of objective evaluations for clinical applications [2, 3, 8].

Despite the advances of these systems, some research questions still remain to be addressed.

A few SGs have been developed to stimulate sensorimotor learning during a locomotion task and extract metrics to draw conclusions about the motor performance [12], which could be associated with the cognitive evaluations in children with cerebral palsy. DL has been little used to perform either continuous HAR (CHAR) through kinematic data [10] or pathological gait recognition (PGR) with inertial data related to normal and simulated pathological walking patterns [13].

Based on the prior discussion concerning opportunities and difficulties of interfaces for motor assessment, the main objective of the research conducted for this thesis has regarded the conceptualization, development, and implementation of frameworks to advance the state-of-the-art in this field. The workflows have been developed with the aim of pursuing their feasibility and usability in clinical scenarios.

The applications considered mainly lies in the field of rehabilitation. Tasks under consideration concerned HAR and performance evaluation. Data under consideration were provided by clinical structures.

1.1.2 Contribution

In the aforementioned scenario, the main purpose of this thesis is to develop new frameworks based on either serious games [12] or Deep Learning for recognizing motor actions prior to their assessment [10, 13].

As regards frameworks for VMA, the majority of works have entailed the upper limbs in order to execute either a reaching or a drawing task. Some researchers have employed a screen and a mirror to project the virtual scenario on a plane that is parallel to the physical workspace, in which an external grabbed object, e.g., a joystick, a stylus, or a robotic manipulandum, is exploited to control the cursor correspondent to the hand motion [14–18]. Alternatively, other studies have displayed directly on a screen the trajectory followed by a cursor, which is utilized for allowing the subject to visualize the path they trace in the real

world on a tablet through a stylus [19, 20]. To introduce the visual perturbation eliciting adaptation, the cursor moving direction has been rotated [16–18, 21, 22] or even gained [15]. However, such VR-based frameworks can be made more motivating by representing the human body in a more realistic way. For this purpose, Lin et al. have mapped real movements as those of two hand-held controllers, which are exploited to interact within the VE that is shown through a HMD; in addition, they included either a consistent or a reverted mapping between the real and virtual paths followed during a reaching task [23]. On the other hand, Cristella and colleagues have proposed three SGs requiring the participant to perform trunk inclination, elbow flexion/extension, and forearm supination/pronation; they have also implemented a coherent or reversed correspondence between the motor command in the real world and the visual feedback [8]. These are only some of the several studies targeting VMA during upper-limb motor tasks, whereas a few works have proposed workflows stimulating VMA during locomotion activity. As instance, Kannape and colleagues have set up a motion tracking area in which subjects have to perform a reaching walking task; besides, a screen has been employed to show a whole-body avatar in a virtual room and an angular deviation has been applied to the captured position to stimulate VMA [24, 25]. The work presented in Section 1.2 offers an addition to the state-of-art in the extent that the proposed SG-based framework addresses VMA in a locomotion activity by controlling a full-body moving avatar in a custom VR environment [12].

As regards human activity recognition, the majority of workflows adddressing HAR based on DL test classifiers on inertial data that are related to a separate execution of ADLs. Only a few works test the DL architecture on data that come from an uninterrupted sequence of activities and are previously trained on IMU signals corresponding to stand-alone activities [26–30]. Most related works proposed a CHAR-oriented approach with a setup based only on radar sensors [26–29]; however, their applicability to outdoor environments is limited by their measurement area [28]. Furthermore, it has been found only one work that performs CHAR with DL methods based only on kinematic data: Jaramillo et al. measured the evolution of the hip joint angle by means of inertial sensors and encoders integrated in an exoskeleton, and included both separate and continuous acquisition protocols [30]. The work presented in Section 1.3 differs from the related literature to the extent that it entails the implementation of a DL algorithm that is fed by inertial measures and is capable of recognizing ADLs executed in a continuous way [10]. Pathological gait recognition is a subfield of HAR aimed to recognize whether a walking pattern is healthy or pathological. In this realm, there exist a few studies that simulate pathological walking patterns to train PGR-oriented AI algorithms, whether ML or DL models, by acquiring inertial data. For instance, Robles et al. [31]

utilized Artificial Neural Networks (ANNs) to classify simulated gait disorders (those of Parkinsonian, ataxic, and hemiplegic) by analyzing accelerations of the center of mass of healthy subjects. Ghobadi et al. [32] discriminated normal gait from mimicked foot drop (FD) by training a support vector machine (SVM) with the data coming from a single IMU placed on the subject's right leg. Yin et al. [33] exploited two accelerometers to feed DL architectures, such as a CNN, with the aim of automatically classifying pathological gaits (e.g., hemiplegic, diplegic, and Parkinsonian), which were emulated by healthy participants. Consequently, the work in Section 1.4 address the limitations of the related works by means of the implementation of a frameworks exploiting the simulation of abnormal walking patterns to train DL-based models for the final aim of recognizing actual pathological gaits [13].

Ultimately, the technical contributions can be summarized as follows: innovative frameworks based on SG and DL have been developed for respectively evaluating VMA and recognizing lower-limb motor actions, whether normal or abnormal.

1.1.3 Chapter Outline

This chapter is organized into the following sections. This chapter introduces the objective and the technical contribution of the clinical-oriented applications of this thesis.

Section 1.2 describes the state-of-art and the contributions proposed in the field of SG-based frameworks for the evaluation of visuomotor adaptation; Sections 1.3 and 1.4 present the scientific literature and the contributions in the field of human activity recognition and pathological gait recognition, respectively.

1.2 A Serious Game for the Assessment of Visuomotor Adaptation Capabilities during Locomotion Tasks Employing an Embodied Avatar in Virtual Reality

The study of visuomotor adaptation (VMA) capabilities has been encompassed in various experimental protocols aimed at investigating human motor control strategies and/or cognitive functions. VMA-oriented frameworks can have clinical applications, primarily in the investigation and assessment of neuro-motor impairments caused by conditions such as Parkinson's disease or post-stroke, which affect the lives of tens of thousands of people worldwide. Therefore, it could enhance the understanding of the specific mechanisms of such neuromotor disorders, thus being a potential biomarker for recovery with the aim of

integrating conventional rehabilitative programs. Virtual Reality (VR) can be entailed in a framework targeting VMA, since it allows the development of visual perturbations in a more customizable and realistic way. Moreover, as it has been demonstrated in previous works, a serious game (SG) can further increase the engagement also thanks to the use of full-body embodied avatars.

Most studies implementing VMA frameworks have focused on upper limb tasks and utilized a cursor as visual feedback for the user. Hence, there is a paucity in the literature about VMA-oriented frameworks based on serious game and targeting locomotion tasks.

This chapter presents the design, development, and test of a SG-based framework that addresses VMA in a locomotion activity by controlling a full-body moving avatar in a custom VR environment. This workflow includes a set of metrics to quantitatively assess the participants' performance. Thirteen healthy children have been recruited to evaluate the framework. Several quantitative comparisons and analyses have been run to validate the different types of introduced visuomotor perturbation, and to evaluate the ability of the proposed metrics in describing the difficulty caused by such perturbations. During the experimental sessions, it emerged that the system is safe, easy to use, and practical in a clinical setting.

This section is organized as follows: Subsection 1.2.1 illustrates the state-of-art regarding frameworks oriented to visuomotor adaptation and Subsection 1.2.2 describes materials, i.e., the VMA-oriented framework that includes a body tracking system for data acquisition, a treadmill for performing locomotion, a SG for promoting the participant's engagement, and a calibration stage for coping with inter-session spatial modifications of the setup and inter-subject differences in gait characteristics; Subsection 1.2.2 also exposes the methodology adopted in this work, which comprises metric extraction and statistical analysis. The outcomes of the experimental study are provided in Subsection 1.2.3 and discussed in Subsection 1.2.4. Ultimately, Subsection 1.2.5 draws the final remarks about the conducted study and delineates ideas for future works.

1.2.1 Related Works

Visuomotor adaptation is a form of sensorimotor learning that allows humans to learn how to adapt, or correct for, an external visual perturbation [34]. Learning how to compensate for the effects of external perturbations relies on the formation of an internal model that computes the difference between anticipated errors of the intended movement and actual errors from sensory feedback, which is then used to plan the next motor action.

A number of studies have proposed different experimental protocols with the aim to evaluate visuomotor adaptation abilities in a large variety of tasks, such as drawing [35–37], target reaching [14, 38] and walking [39–41]. Since VMA mainly deals with the learning of the motor adjustment to be executed for reducing the visual perturbation effects to accomplish the given task [34], visual perturbations eliciting VMA may be included in experimental protocols to investigate motor learning and motor control abilities of healthy subjects [42–49]. Moreover, several studies have investigated how to integrate the VMA evaluation in cognitive assessment protocols. In fact, visuomotor adaptation has been found to be correlated with cognitive functions, e.g., working memory, executive functions, and processing speed [16, 19, 21, 50–53], and also related to motion awareness and cognitive load [24, 25].

Experimental setups for VMA capability evaluation have been also largely employed in clinical scenarios for multiple purposes, such as, to evaluate the aging effect on motor skills, e.g., human balance, gait parameters, or adaptive processes [39, 54, 55], or to verify the relationship between the decline in adaptation and age-related deterioration of cognitive functions [20, 56–58]. Experiments entailing VMA have been also proposed to investigate and assess the capabilities of subjects affected by neuro-motor disorders, such as: people with cerebellar degeneration [59], children with autism spectrum and developmental coordination disorder [60, 61], teenagers with cerebral palsy [8], patients affected by Parkinson's disease [15, 62, 63], hemispheric lateralization of stroke survivors [18], multiple sclerosis patients [64], dystonic subjects [17], autistic individuals [65] and people affected by essential tremor [66].

A typical VMA experimental protocol encompasses a phase in which the subject under evaluation is asked to perform a motor task in a scenario featuring an altered condition. A framework targeting VMA is mainly composed of three fundamental elements: the scenario, or the environment, in which the goal-oriented task is executed; the motor command input system, which is necessary to detect the performed motor action in the real world and encode it in an action within the scenario/environment; and a set of possible perturbations used to alter the "normal" mapping between the real world and the scenario/environment. These aspects have to be tailored to the research purpose, as well as to the human body part that is involved during the requested motor task. VMA may be evaluated in a real scenario by interposing prism lenses between the subject's view and the workspace [67]; on the other hand, the motor task can be visualized in a virtual environment (VE), which can be provided to the user by means of either a screen [14–18, 38–41, 47, 51, 55, 68] that is optionally combined with a mirror projecting computer-generated images on the workspace

[14–18, 38, 47, 51, 55], or a head-mounted display (HMD) [49, 54, 69–72]. Hence, while the visual feedback given to the user is altered, the activity to execute might consist in reaching a target through a cursor [14–18, 38, 47, 51, 73], or in keeping balance [39–41, 54, 69, 70]. Moreover, the motor actions performed by the subject can be guided in different ways, such as: by recording the position of a device mediating the interaction, e.g., a joystick [8, 14, 38, 60], a stylus [19–22, 35, 37, 42, 44, 53, 55, 61], or a robotic manipulator [17, 74]; by tracking the motion performed by the human body [24, 25, 39–41, 54, 69, 70]; or even by measuring the force exerted on a handle or acquiring the myoelectric muscle activations [68, 75, 76]. The VMA-directed discrepancy between the expected and the visually perceived outcome can be introduced by altering the input action in the form of a translation [42, 69, 77], a rotation [14, 16, 19, 21, 24, 25, 37, 42, 50, 55, 60, 68, 78, 79], or a reversal [8, 35, 51, 52] of the path that is traced, or even a set of sinusoidal oscillations on the visual field that is presented [39–41, 49, 54, 70].

The employment of virtual reality (VR) leads to more adaptable and customizable synthetic scenarios/environments. In fact, a virtual scenario simplifies the integration between the task that has to be done in the environment and the subject's motor command. On the other hand, a fully virtual scenario allows the design of a large variety of perturbation types that can be also modulated and changed without any restriction during the experimental protocol [54]. Furthermore, it is well known that a VR-based serious game (SG) amplifies the individuals' engagement, which should be ensured since participants could stop feeling motivated because of the repetitiveness that is typical of scientific experiments [80, 81]. VR can also provide a greater sense of embodiment by mapping human body parts more realistically [82] and this feeling may be even increased by recurring to a full-body avatar representation [83].

1.2.2 Materials and Methods

This subsection is articulated in the description of the framework utilized for VMA assessment (Subsubsection 1.2.2.1) and in its experimental test (Subsubsection 1.2.2.2).

1.2.2.1 The proposed framework

The framework that is proposed for experiments eliciting and evaluating VMA is made up of three main components (see Figure 1.1), which are: a human skeleton tracking system, a treadmill, and a fully-customizable VR-based serious game.

The technical requirements and the features of the presented framework have been discussed and defined during a number of meetings with the clinical staff of the IRCCS Fondazione Don Carlo Gnocchi ONLUS (Florence, Italy), who expressed the need of a customizable VR-based serious game to evaluate the visuomotor adaptation capabilities of children with neuromotor disorders during locomotion tasks. In particular, the following requirements have been defined and used for the design and implementation phases of the presented framework:

- the subject has to control the position of an embodied avatar in a custom virtual environment during a locomotion task;
- the subject has to collect pseudo-random objects that are located on the virtual ground along a path - the avatar can collect objects by hitting them;
- the subject has to walk on a treadmill while collecting the virtual objects, and the treadmill must allow the mediolateral (ML) movement of the entire body to pick up objects that are positioned on the sides of the path;
- the subject must also experience two kinds of perturbation that alter the position mapping between the real ML position of the subject and the ML position of the avatar in the VE, i.e., GAIN and REVERSAL, that aim at amplifying and reverting the avatar's movement (respectively);
- the use of a marker-less solution to track the human skeleton body should be preferred to speed up the experimental setup phase;
- motivating soundtracks should be used.

Fig. 1.1 The experimental setup.

The subject skeleton tracking system The first subsystem of the proposed framework is a real-time body tracking system that is used to let the participant control the avatar's position within the virtual environment and the modeled articulation joints. In this study, a 3D Azure Kinect that has been positioned 0.5 m away from the subject in order to acquire the scene and the whole front part of the subject's body. In particular, the Azure Kinect Body Tracking SDK has been used to automatically extract the human skeleton, i.e., the poses of all modeled joints and links of the skeleton (see Figure 1.2), with a frame rate of 50 Hz [84]. It is worth mentioning that the large use of the Microsoft Kinect in clinical setups during the last decade is mainly motivated by the low price and its high accuracy considering the cost [85–88].

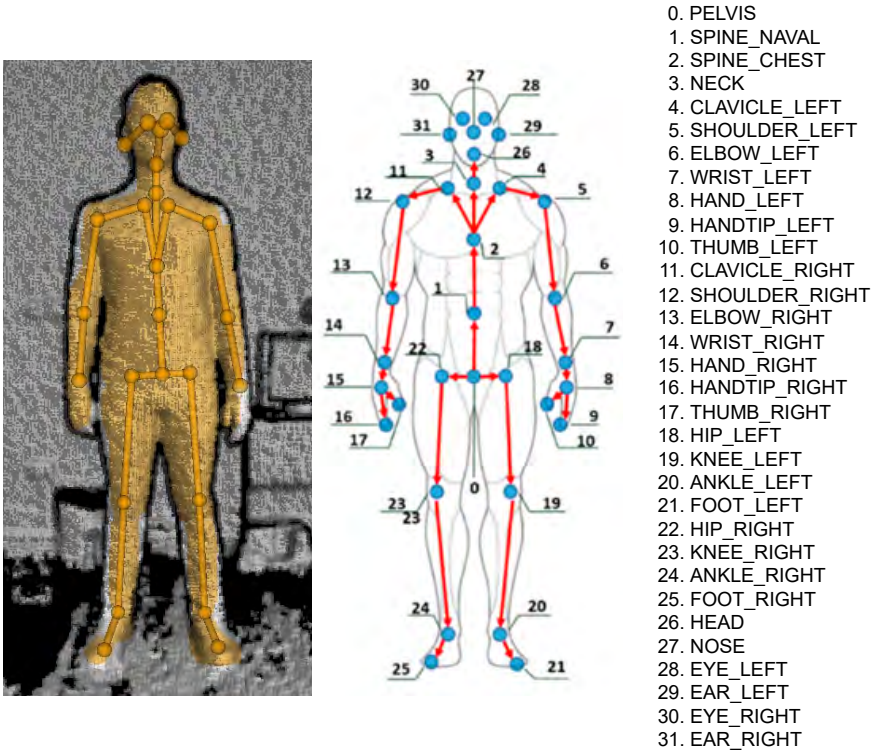

Fig. 1.2 Skeleton tracked by the Azure Kinect SDK.

The treadmill A treadmill has been chosen as a locomotion surface since it allows walking continuously, thus keeping subjects focused on the task to execute. The treadmill width has to be such that a comfortable walking area allows mediolateral movements to the participants during the whole session. In this specific study, the employed treadmill is the C-Mill VR (by Motek®, Amserdam NL). It is equipped with a safety frame and two adjustable handrails to prevent subjects from the risk of falling (e.g., due to loss of balance) and also provides the possibility to measure some gait parameters that can be exploited to tailor the locomotion to the individual characteristics. It is worth mentioning that the proposed framework is independent of the type of adopted treadmill. Therefore, even a simple cheap treadmill that is not able to compute the position of the subject's center of gravity and make it available in real-time can be employed.

The serious game According to the defined requirements, the designed and developed SG allows a subject that is walking on a treadmill to control the position of an embodied avatar with the aim at collecting objects along a path. Specifically, the subject can pick up an object, which may be located either at the center or at the sides of the virtual road, by controlling

the ML position of the avatar. The subject can thus translate the avatar along the ML axis by moving his/her body on the treadmill along the real ML plane within a feasible range of motion (RoM). More in detail, the ML position of the subject's pelvis is used to directly control the ML position of the avatar's pelvis.

The SG, which has been developed using the Unity3D framework (Release 2020.3.27f1, Unity Technologies, San Francisco, CA, USA), implements also the link between the human joints tracked by the Kinect Azure SDK and the corresponding avatar's joints by using a Unity 3D demo available on the Microsoft GitHub webpage [89].

The game permits placing a series of rewarding objects (e.g., candy) on a straight virtual road in any position. The software also enables collecting these targets by moving a full-body avatar on the virtual endless walkway while walking on the treadmill. Besides, a trial has been associated with each object, whose collection entails the game score update. Any object is rendered one at a time and stays visible until it is collected or surpassed by the avatar while advancing in the scene. Subsequently, in order to adapt the difficulty of the task to the specific anthropometric characteristics of each subject, the distance in the real world between two subsequent objects has been set equal to eight strides. In addition, the SG continuously regenerates the virtual road with the aim of rendering the endless walkway that corresponds to the treadmill in the real world. It also makes the avatar advance in the scene along the locomotion direction by linearly incrementing the avatar's position of a quantity that depends on the subject's velocity.

In this work the virtual environment has been shown on a 2D monitor that is positioned in front of the subject. The screenshots in Figure 1.3 depict the avatar moving on the virtual road and the target to be picked that are shown within the VE.

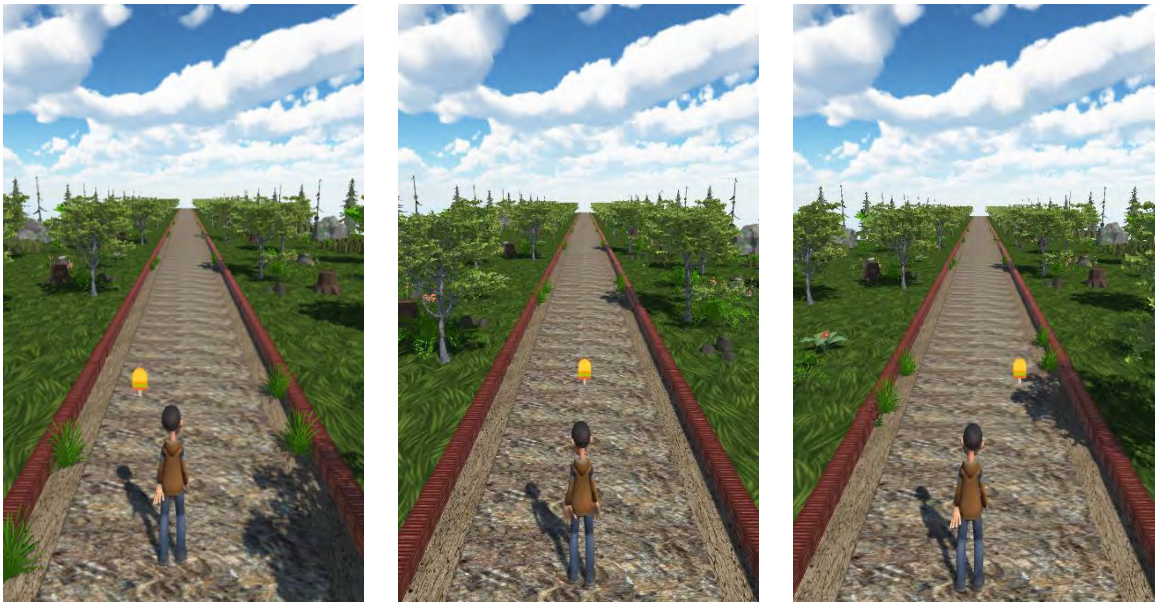

Fig. 1.3 Different screenshots of the main scenario of the serious game.

Furthermore, a proper mapping between real and virtual displacements enables that the boundaries in the virtual space correspond to those of the real workspace, which is defined by the participant's range of motion along the ML axis. Such a basic mapping constitutes the game functioning in the absence of perturbations.

Concerning the possible visual perturbations that might characterize a single trial, it has been decided to allow the manipulation of the mapping between the ML position of the avatar on the virtual road and the ML position of the subject on the treadmill. In particular, four possible mapping conditions between the real and virtual environments have been implemented (see Figure 1.4) and listed below:

- *No Perturbations*: the mapping is not altered - the avatar moves as the subject - when the subject reaches the side of the treadmill the avatar is on the side of the virtual road;
- *Gain*: the mapping is altered - the avatar moves following the same sense of the subject's movement - the avatar's movements on the ML plane are amplified by a specific gain factor;
- *Reversal*: the mapping is altered - the avatar moves following the opposite sense of the subject's movement (i.e., when the subject moves to the right, the mapping leads the avatar to the left, and vice versa) - when the subject reaches the left side of the treadmill the avatar is on the right side of the virtual road and vice versa;

- *Reversal+Gain*: the mapping is altered - the above-mentioned perturbations are simultaneously applied, thus amplifying and reverting the avatar's position at the same time.

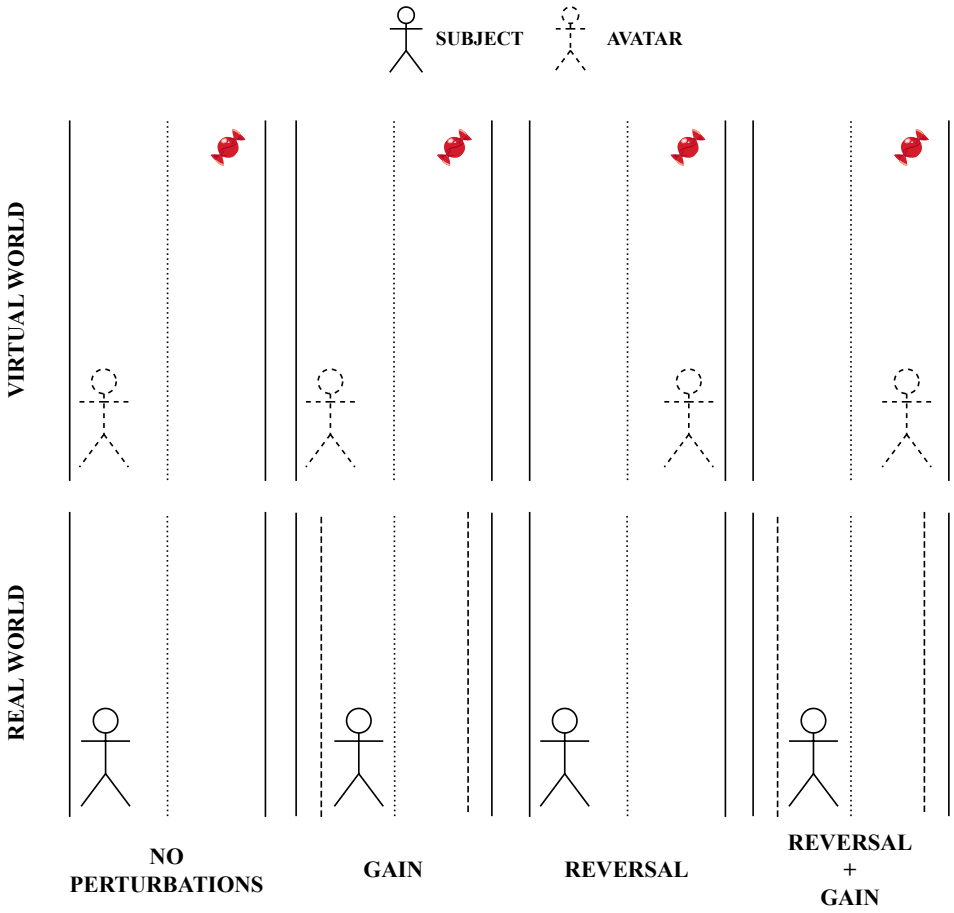

Fig. 1.4 Graphical representation of the effects of the four positional mapping conditions. Vertical continuous lines indicate the boundaries of the treadmill and the virtual road, whereas the dashed lines refer to the sides of the reduced real space due to the gain factor.

Note that, due to the gained mapping, the avatar may go beyond the limits of the road when the subject reaches the treadmill boundaries. Hence, the SG guarantees that the avatar is always visible thanks to a saturation that is imposed on its lateral position. The SG has been implemented as a sequence of several scenes, each of which is provided with a soundtrack that aims to keep subjects motivated and prevents them from getting bored or loosing motivation. Finally, it is worth reporting that the implemented SG also provides a user-friendly form allowing the clinical staff to build a customized experimental protocol, i.e., the specific sequence of objects to collect and the type of perturbation that can be applied within specific phases of the protocol.

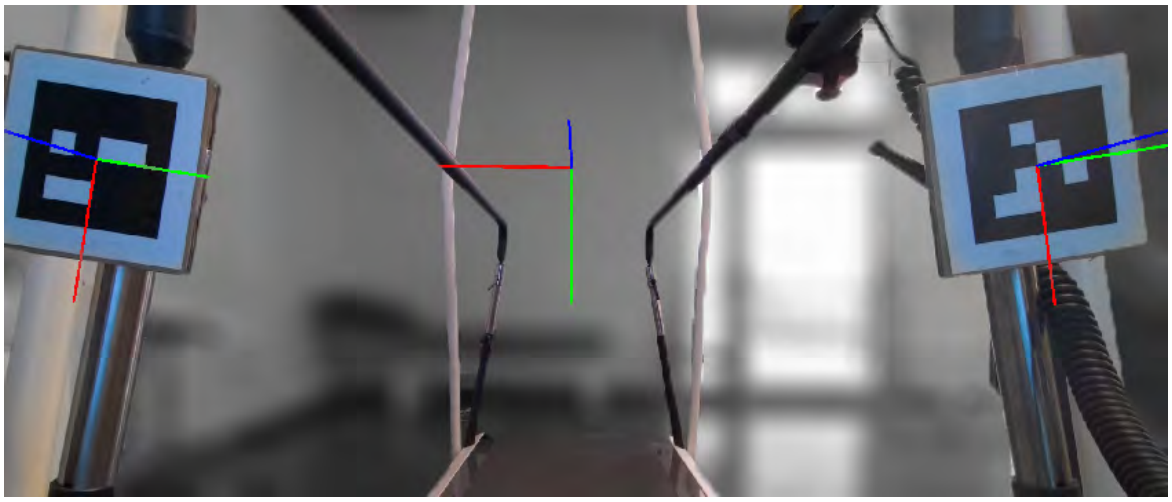

Fig. 1.5 A processed frame acquired by the Azure Kinect that shows the two ArUco markers positioned on the lateral handrails of the treadmill and a 2D representation of both the markers and the treadmill reference frames.

Initial calibration procedures A set of initial calibration procedures has been also designed both for adapting the task to the specific anthropometric characteristics of the subject and for managing the unknown pose of the Azure Kinect reference frame and treadmill reference frame. As a first step, the following three parameters are acquired with dedicated tests and inserted within a specific form of the SG concerning the subject data:

- the *preferred walking speed (PWS)*: the treadmill speed is kept fixed and equal to the PWS during the entire experimental session - such speed is also used to translate the avatar's center of mass along the locomotion direction - this speed is experimentally found with the help of the clinical staff by gradually increasing the belt speed until the participants reported that they were walking at their PWS [90, 91];
- the *mean step length*: the parameter that is used to define the distance between two subsequent objects to collect - in this specific work the step length has been automatically extracted by the C-Mill software, even though any other solution based on the skeleton data processing can be used;
- the *range of motion* of the subject's pelvis on the treadmill along the mediolateral axis - such measure is used to adapt the real subject's RoM to the avatar's RoM.

As a second step, a procedure that is able to define the relative pose between the Azure Kinect camera and the treadmill is executed, since it is necessary to correctly map the real and virtual worlds. ArUco, an open-source library that allows to define and track 2D markers [92], is

exploited. As shown in Figure 1.5, two different ArUco markers have been positioned on the two lateral handrails of the treadmill so that they can be both visible to the Azure Kinect that is capturing the entire scene. For each marker, the ArUco library is able to compute the pose of the relative reference system with respect to the camera reference system. Finally, the final reference system of the treadmill is defined as follows: it is positioned at the midpoint of the origins of the two marker reference systems, and its x-axis is oriented as the line that crosses the two origins, whereas the y-axis is oriented as the gravity vector.

Performance metrics Besides the system that has been presented above, the proposed framework also considers a set of metrics that can be used to quantitatively evaluate the performance of each subject. The percentage of collected targets (CT) is an obvious metric that has been examined to evaluate the visuomotor adaptation capability. However, the CT metric does not encode any information concerning the trajectory that the subject followed for each target. Hence, for each object to be collected, three metrics have been computed to quantify three different characteristics of the 2D trajectory of the avatar's pelvis. More in detail, considering the avatar trajectory between its 2D position at the end of the previous trial and its 2D position at the end of the current trial, i.e., when the avatar either hits or surpasses the object:

- Normalized Path Length (NPL): the length of the actual path divided by the length of the minimum length path (MLP), which is the straight line that passes through 2D points, i.e., start and end positions;
- Normalized Area (NA): the area between the actual path and MLP, divided by MLP length;
- Initial Angle Error (IAE): the angle between MLP and the segment joining the avatar's initial position with the point of the real path that corresponds to the first peak of the distance from the MLP.

In view of the definition of the trajectory-based features, it is inferable that the higher their value the worse the performance. The meaning of the extracted kinematic-based metrics is graphically explained in Figure 1.6.

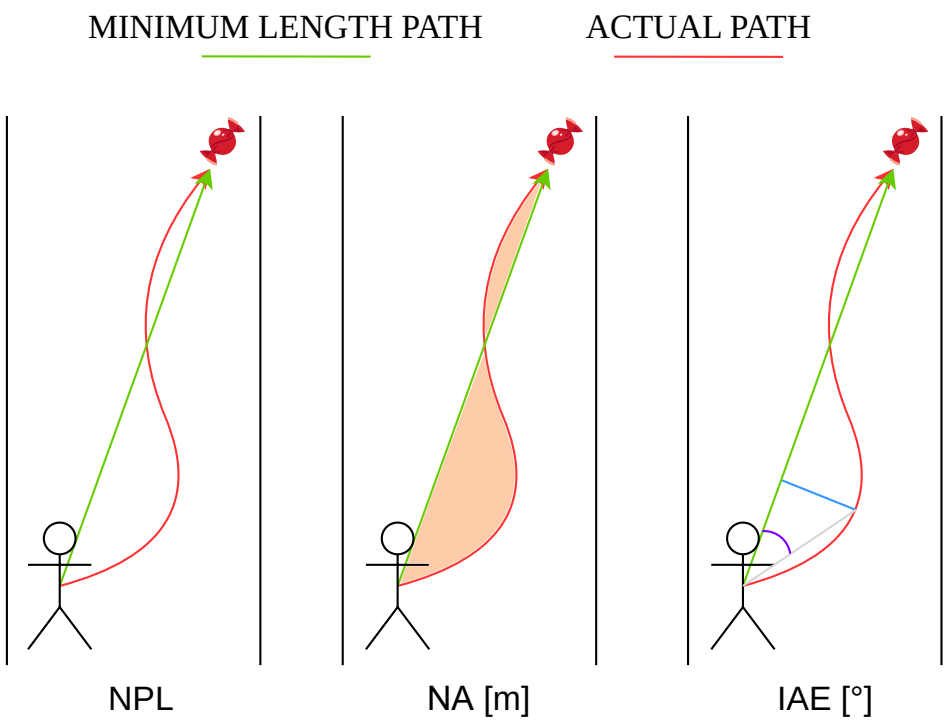

Fig. 1.6 Kinematic-based features selected for assessing difficulty modification: NPL is the ratio between the length of the actual path and the one of the MLP; NA measures the area between the actual path and the MLP, divided by the length of the MLP; IAE is the angle between the MLP and the segment joining the avatar's initial position with the point of the actual path that corresponds to the first peak of the distance from the MLP.

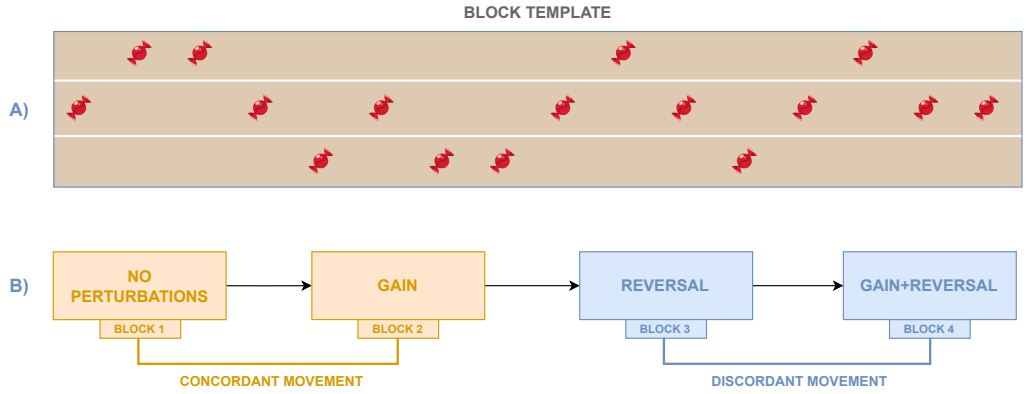

Fig. 1.7 A) Arrangement of the targets (e.g., candy) in each block. Sixteen objects are placed on the virtual road such that their number on the right side is the same as those on the left side, thus preventing the avatar from direct movements between the two extremities. B) Sequence of the four blocks defined by the experimental protocol and associated with the mapping conditions explained in Subsection 1.2.2.1.

1.2.2.2 Framework test

The framework test is intended to prove the quality of the game development and the features extracted within the post-processing phase in terms of capturing the task difficulty related to the mapping perturbations. Moreover, the proposed workflow has been tested from the point of view of usability and safety, which are important requirements to be met in a clinical-oriented context. For this purpose, this work has involved healthy subjects as participants and has included an experimental protocol to be followed for a correct task execution. Furthermore, the proposed features, which encode the outcomes obtained in the different mapping conditions, have been compared and statistically analyzed.

Participants Thirteen healthy children (10.2 ± 1.7 years old, six males) have been recruited from the IRCCS "Don Carlo Gnocchi". Inclusion criteria were: 1) children that exhibit neither neurological nor cognitive disorders (such conditions have been verified through two batteries of neuropsychological tests, which are WISC-IV and NEPSY-II [93, 94]), 2) children that usually spend between one and three hours a week playing video games. Each subject has been informed about the task execution and the game details, without mentioning any information about the visual perturbations to prevent results from being influenced by this awareness.

Experimental protocol The experimental protocol has been arranged with the clinicians in such a way as to make the SG suit the subject's characteristics, thus being more realistic in terms of gait simulation. Hence, prior to the game session, subjects' parameters, which are the preferred walking speed, the step length, and the range of motion along the ML axis, have been measured by means of the sensors embedded in an instrumented treadmill (C-Mill VR by Motek®). It is worth noting that if the setup is based on a standard non-instrumented treadmill, such subject's parameters can be derived by analyzing the 3D data of the human skeleton extracted by the Kinect Azure.

A customized experimental protocol is proposed to test the presented framework that will be detailed just below; however, multiple experimental protocols featuring a different target sequence, different target positions, or a different sequence of perturbations might be used according to the specific needs. In this specific test study, a template block (see Figure 1.8A) is defined considering a predefined sequence of targets that are positioned at the center or the sides of the virtual road. The used sequence has been chosen to ensure that the number of targets on the right side is equal to the number of the ones on the left side, and the avatar must not directly move between the two road sides. It is worth reminding that the targets

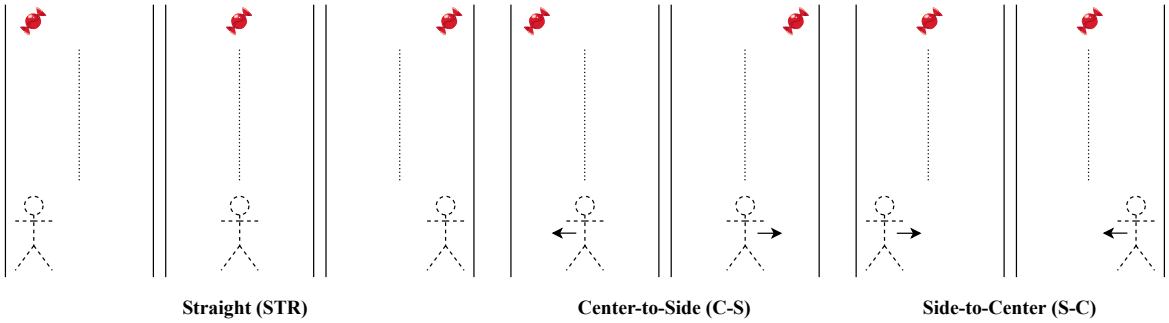

Fig. 1.8 Three directions can be recognized for the line connecting two consecutive targets: for accomplishing the collection task, the avatar can either keep the direction in the straight (STR) case, or move from the center to one of the sides in the center-to-side (C-S) case, as well as from one of the sides to the center in the side-to-center (S-C) case.

are rendered one by one so that the subject is fully focused on just one target at a time, thus avoiding any anticipatory effect.

Given the definition of a block, the experimental protocol consisted of four subsequent blocks, each of which is characterized by a different mapping condition. As shown in Figure 1.8B, the defined sequence of the conditions is as follows: 1) *No Perturbations*, 2) *Gain*, 3) *Reversal* and 4) *Reversal+Gain*. The fixed order of succession of the conditions does have an impact on the results due to the learning effect and that the specific tested experimental protocol has not been properly designed for a standard motor control/learning study. In fact, the objective of the study is to propose a system that can be used to assess visuo-motor adaptation capabilities and verify that the introduced perturbations produce some effects that can be captured by the performance metrics. More specifically, the avatar's motion on the ML plane occurs in the same sense (concordant) as the real one in the first two blocks, whereas its lateral movements occur in the opposite sense (discordant) with respect to the participant's ones in the last two blocks. In the first block no perturbation is included, thus making the lateral movement of the virtual character occur in the same direction and with no amplification with respect to the real displacement; in the second block the avatar's position along the ML axis is amplified such that the needed real range of motion is reduced by 25%. The third block is characterized by the *Reversal* condition, and, finally, in the last block the *Reversal+Gain* condition has been applied using the same gain factor of the second block.

Comparisons and Statistical analysis The metrics extracted in the different conditions have been compared to ascertain whether they are able to capture the differences among

the defined mapping conditions. Moreover, the direction of the minimum length path (i.e., the straight line that passes through the initial avatar position and the target position) is believed to be an important factor that can be analyzed, since it might have an impact on the performance. In detail, as shown in Figure 1.8, three directions may be recognized: straight (STR), center-to-side (C-S), and side-to-center (S-C), where the side may be either left or right. Therefore, the following comparisons are performed considering all subjects:

- Comparison 1 - among mapping conditions;
- Comparison 2 - among mapping conditions grouped by directions;
- Comparison 3 - among directions grouped by mapping conditions.

Concerning comparison 1, for each subject, the mean of kinematic features and the percentage of collected objects have been computed within the mapping condition; regarding comparison 2, for each subject, the mean of kinematic features and the percentage of collected objects have been computed within the mapping condition considering each direction independently; in addition, as regards comparison 3, for each subject, the mean of kinematic features and the percentage of collected objects have been computed within the direction considering each mapping condition independently. These comparisons are pictorially depicted in the boxplots reported in Figures 1.9-1.13.

After that, statistical comparisons have been performed with the non-parametric Friedman's test, since the hypothesis of Gaussian distribution is excluded by the limited number of children involved in this study. When finding a significant difference in this way, a deeper analysis has been performed through a pairwise post-hoc test with Bonferroni's correction, whose significant level has been set to $p < .05$. All the analysis has been conducted by using Matlab 2021b.

1.2.3 Results

This subsection presents the results of the twofold test that have been performed for the proposed framework: the outcomes concerning the usability, safety, and feasibility in a clinical context are reported in Subsubsection 1.2.3.1, whilst the results about the efficacy of the designed features in capturing the difficulty modification due to mapping perturbations are described in Subsubsection 1.2.3.2.

1.2.3.1 Feasibility in a clinical context

The proposed framework targeting VMA has met different feasibility requirements such that it is usable in a clinical context. At first, setting up an experimental session is not excessively time-consuming since very few and fast calibration procedures are needed and, particularly, a marker-less human-skeleton tracking system has been employed. It is well known that clinical experimental sessions should be characterized by fast procedures also because it is important to keep participants interested and motivated during the entire experimental procedure.

Moreover, the user-friendliness of the software has been guaranteed by offering a protocol that is simple to follow for clinicians. Another aspect that played an important role is related to the possibility to define protocols that are tailored to the individual anthropometric characteristics, thus aiming to adapt the game difficulty to the specific subject and allowing for inter-subject comparisons.

Finally, the proposed framework has proved to ensure children's safety, since neither forms of sickness (e.g., vertigo) nor losses of balance have been reported by participants; nevertheless, the risk of falls coming from the potential loss of balance is prevented by means of the supporting components with which the used treadmill is equipped.

1.2.3.2 Quantitative metric validation

This subsubsection describes the obtained results concerning the comparisons listed in Paragraph 1.2.2.2. More in detail, mapping conditions, mapping conditions grouped by directions, and directions grouped by mapping conditions have been compared. Such comparisons are illustrated in the boxplots reported in Figures 1.9-1.13.

Differences among mapping conditions Statistically significant differences have been revealed for each feature when comparing mapping conditions regardless of the direction. The outcomes of the proposed metrics for evaluating difficulty alteration among mapping conditions are pictorially depicted in the boxplots reported in Figure 1.9.

CT (Collected Targets) is the percentage of the objects collected by the avatar. In this regard, Friedman's test has revealed that the CT significantly differs among mapping conditions with $p < .001$. Besides, according to post-hoc tests the CT in the conditions with reverted mapping is significantly lower than the CT in both mappings without reversal; instead, no statistically significant differences have been found in the CT between the two conditions without reversal, as well as between the two mappings including reversal. In fact,

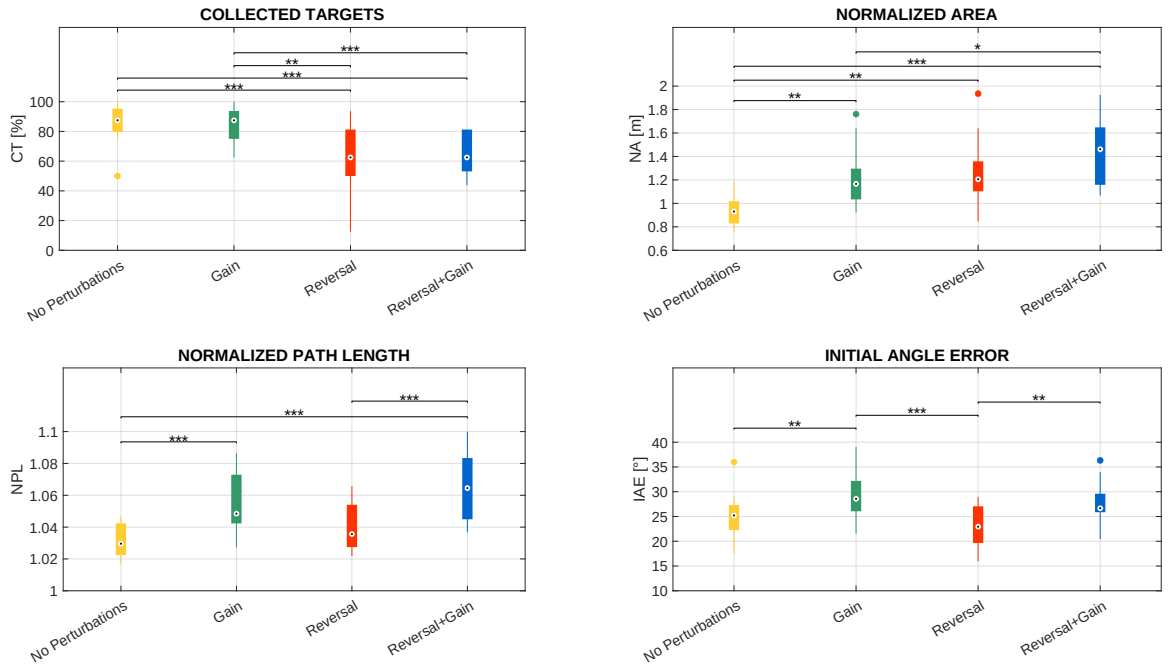

Fig. 1.9 The boxplot of the distribution of the chosen features computed in each mapping condition with * representing statistically significant comparisons with $p < .05$, ** representing statistically significant comparisons with $p < .01$, and *** representing statistically significant comparisons with $p < .001$.

the CT in *Reversal* is significantly lower than the one in *No Perturbations* with $p < .001$ and the one in *Gain* with $p < .01$. Similarly, the CT in *Reversal+Gain* is significantly lower than the one in *No Perturbations* and the one in *Gain*, with $p < .001$ in both cases.

Reminding that NA (Normalized Path Integral Error) is a normalized measure of the area between the actual path and the length of the MLP, Friedman's test has shown statistically significant differences in NA among mapping conditions with $p < .001$. Post-hoc tests have revealed the mapping without perturbations is significantly different from the mappings including either one or two perturbations: in particular, the NA in *No Perturbations* is significantly lower than the one in *Gain* and *Reversal* with $p < .01$, and the one in *Reversal+Gain* with $p < .001$.In addition, the NA in *Gain* is significantly lower than the NA in *Reversal+Gain* with $p < .05$.

As concerns NPL (Normalized Path Length), which is the length of the path actually covered by the avatar divided by the length of the MLP, Friedman's test has led to statistically significant differences in NPL with $p < .001$ among mapping conditions. Remarkably, in the mapping conditions characterized by the *Gain* the NPL is significantly higher than the NPL observed within the conditions without *Gain*: in fact, the NPL in *Gain* is significantly higher

than the one in *No Perturbations*, as well as the one in *Reversal+Gain* is significantly higher than the one in *Reversal*, with $p < .001$ in both cases. The NPL in *Reversal+Gain* is also significantly higher than the one in *No Perturbations* with $p < .001$, whilst no statistically significant differences have been reported between the NPL in *Gain* and the one in *Reversal*.

With regards to IAE (Initial Angle Error), which indicates the initial angular deviation from the MLP direction, Friedman's test has revealed that the IAE significantly differs among all conditions with $p < .001$. The IAE trend among the tested conditions is very similar to the NPL trend. The IAE measured in the mapping conditions characterized by the *Gain* is higher than the IAE observed within the conditions without the *Gain*: the IAE in *Gain* is significantly higher than the one in *No perturbations*, and the IAE in *Reversal+Gain* is significantly higher than the one in *Reversal*, with $p < .01$ in both cases. Besides, the IAE in *Reversal* is significantly lower than the one in *Gain* with $p < .001$.

Differences among mapping conditions grouped by directions The comparisons that have been presented above are useful to provide a general overview of the differences that have been observed among the different mapping conditions. However, a deeper analysis is necessary and has been performed to investigate the role of the different MLP directions (see Figure 1.8). In particular, this Subsection presents the results obtained when comparing the different conditions focusing on each of the three possible directions: straight (STR), center-to-side (C-S), and side-to-center (S-C). The results of these comparisons are pictorially depicted in the boxplots reported in Figure 1.10-1.11.

Friedman's test has revealed that CT significantly differs among mapping conditions within all directions with $p < .01$. Within each direction the trend of differences among the mapping conditions is almost similar both to each other and to the differences observed in the general comparison (Subsubsection 1.2.3.2). In fact, it turned out that the CT in *No Perturbations* is higher than CT in *Reversal+Gain* in all directions, but this difference is statistically significant only within the STR and the S-C directions with $p < .01$. Similarly, the CT in *Gain* is higher than the one in *Reversal+Gain*, but this comparison is statistically significant only in the STR and S-C directions with $p < .01$ and $p < .001$ respectively. On the other hand, the CT in *Reversal* is lower than the one in *Gain* in all directions, but this relation is statistically significant only in the S-C direction with $p < .05$. Moreover, the CT in *Reversal* always lessens the one in *No perturbations*, but this is statistically significant only in the C-S direction with $p < .05$.

Concerning the NPL, it is worth noting that within each direction the relative differences among the mapping conditions are almost identical both to each other and to the differences

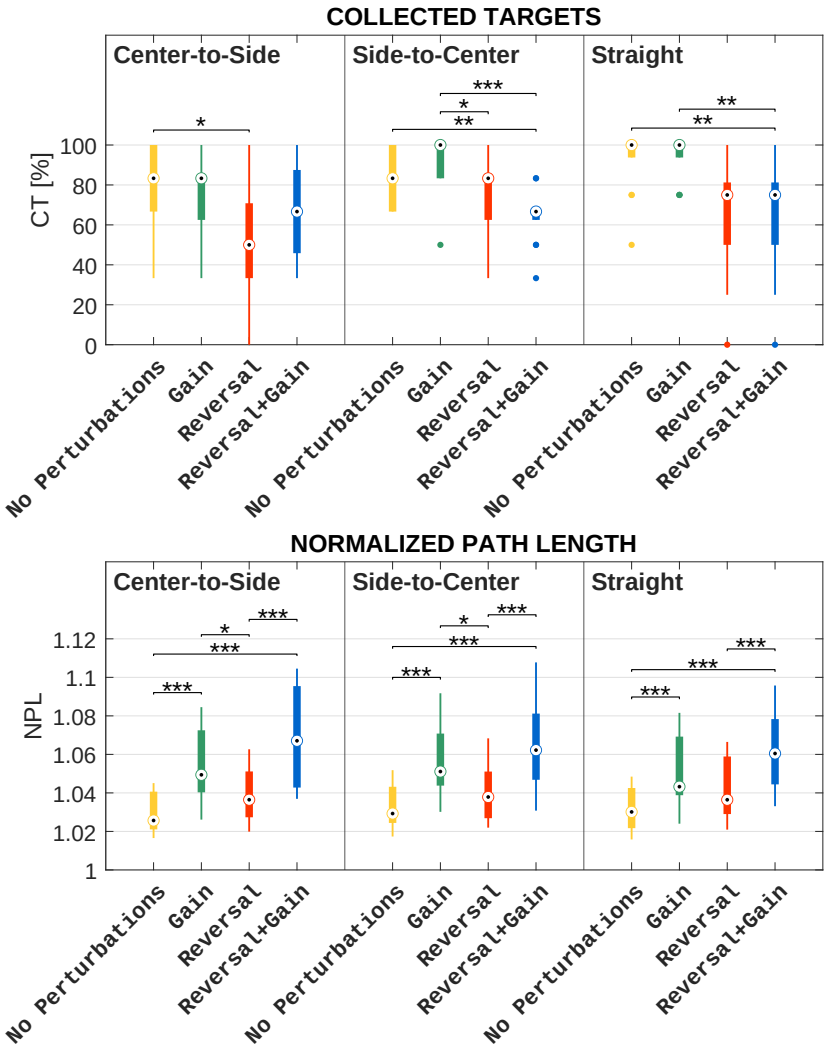

Fig. 1.10 The boxplot of the distribution of the chosen features computed in each mapping conditions grouped by directions with * representing statistically significant comparisons with $p < .05$, ** representing statistically significant comparisons with $p < .01$, and *** representing statistically significant comparisons with $p < .001$.

observed in the general comparison (Subsubsection 1.2.3.2). Friedman's test has proved that this metric is significantly different among mapping conditions with $p < .001$ within all directions. More specifically, within all directions the NPL in *No Perturbations* has proved to be significantly lower than the one in *Gain*, and the NPL in *Reversal* significantly lower the one in *Reversal+Gain*, with $p < .001$ in both cases. In addition, post-hoc tests also revealed that the NPL in *No Perturbations* is significantly lower than the one in *Reversal+Gain* with $p < .001$ within all directions. On the other hand, the NPL in *Reversal* is higher than the one in *No Perturbations* within all directions, but this relation has not resulted statistically significant in any direction. Similarly, the NPL in *Gain* is higher than the one *Reversal* within all directions, but significant differences have been yielded only within the C-S and S-C directions with $p < .05$ in both cases.

Concerning NA, Friedman's test has shown significant differences in NA among mapping conditions within all directions with $p < .001$. The relative differences among conditions of *No Perturbations*, *Gain* and *Reversal+Gain* are similar both to each other and to the differences observed in the general comparison (Subsubsection 1.2.3.2). The main observed difference concerns the NA values measured during the *Reversal*: in S-C and STR the values are comparable to the *No Perturbations* ones, whereas in C-S the NA values are higher than both *No Perturbations* and *Gain* values. More in detail, the NA in *No Perturbations* is significantly lower than the one in *Reversal+Gain* within all directions with $p < .001$; the NA in *No Perturbations* also lower the one in *Gain* in all directions, but this difference is statistically significant only within the C-S and S-C directions with $p < .05$ and $p < .01$ respectively. Furthermore, the NA in *Reversal* is significantly higher than the one in *No Perturbations* only within the C-S direction with $p < .001$, whilst their medians are almost the same in the remaining directions. However, the NA in *Reversal* is always lower than the one obtained in *Reversal+Gain*, although this difference is statistically significant only within the S-C and STR directions, with $p < .01$ and $p < .05$ respectively.

Ultimately, regarding the IAE values, it is worth noting that the relative difference among the conditions in the S-C and STR directions are analogous both between these two directions and with respect to the general comparison (Subsubsection 1.2.3.2). Differently, the IAE values of *Reversal* and *Reversal+Gain* registered in C-S are comparable with values acquired in *No Perturbations* and *Gain*. According to Friedman's test, the IAE significantly differs among mapping conditions within all directions with $p < .001$. Nonetheless, post-hoc tests have led to statistically significant differences only within the C-S and S-C directions. In fact, the IAE in *No Perturbations* is always lower than the one in *Gain*, but this difference is statistically significant only within the C-S direction with $p < .01$. On the other hand,

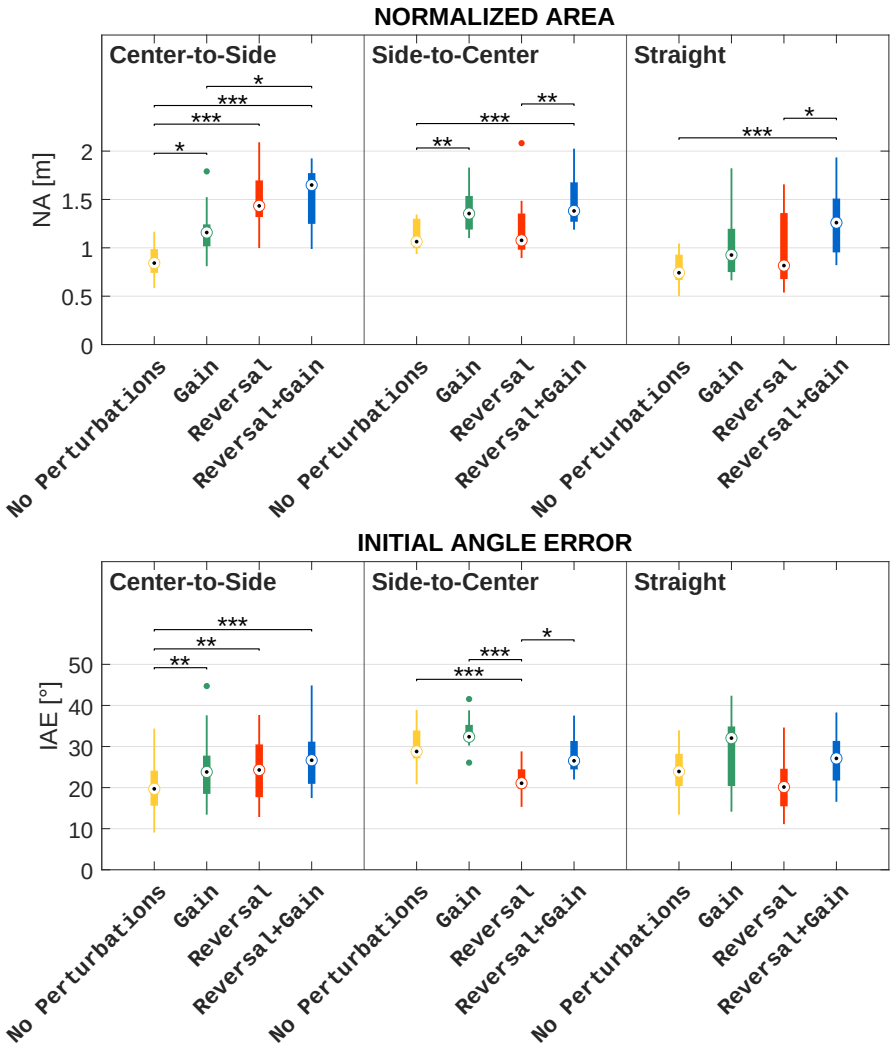

Fig. 1.11 The boxplot of the distribution of the chosen features computed in each mapping conditions grouped by directions with * representing statistically significant comparisons with $p < .05$, ** representing statistically significant comparisons with $p < .01$, and *** representing statistically significant comparisons with $p < .001$.

the IAE in *Reversal* always lessens the one in *Reversal+Gain*, but a statistically significant difference has been yielded only within the S-C direction with $p < .05$. Furthermore, the IAE in *Gain* is higher than the one in *Reversal* within the S-C direction with $p < .001$, whereas no statistically significant differences have resulted within the remaining directions. Similarly, the IAE in *No Perturbations* is either significantly lower or higher than the one in *Reversal* within the C-S and S-C directions, with $p < .01$ and $p < .001$ respectively.

Differences among directions grouped by mapping conditions In this subsection the results related to the comparisons among the three directions for each specific mapping condition are presented (see the Figure 1.12-1.13). The comparisons presented in the previous subsection allowed for scrutinizing the dependence between the differences among the mapping conditions and the directions. The comparisons presented in this section allow for directly investigating the role of the direction given a specific mapping condition.

Friedman's test has revealed that CT does not significantly differ among the directions within *Reversal+Gain*, whereas it has happened for all the remaining conditions with $p < .05$. Furthermore, the CT in the C-S direction is always lower than the one in the STR direction within all conditions, but this relation is statistically significant only within *No Perturbations* and *Gain*, with $p < .05$ and $p < .01$ respectively. On the other hand, the CT in the STR direction is higher, but not significantly, than the one in the S-C direction only within *No Perturbations* and *Reversal+Gain*, whilst the CT median in the STR direction is either equal or lower than the one in the S-C direction within the *Gain* and *Reversal* respectively. Similarly, the CT in the C-S direction significantly lessens the one in the S-C direction within *Gain* and *Reversal*, with $p < .05$ in both cases, whereas the medians in the C-S and S-C directions are the same within *No Perturbations* and *Reversal+Gain*.

When focusing on the NPL, it mainly emerges that this feature does not depend on the direction with very few not marked exceptions. In fact, the only significant findings are: the NPL in the S-C direction is significantly higher than both the one in the C-S direction within *No Perturbations* and than the STR direction within *Gain*, with $p < .05$ in both cases.

With regard to NA Friedman's test has reported statistically significant differences among directions within all conditions with $p < .001$. Two different behaviors emerged when comparing the mapping conditions without reversal with the mapping conditions characterized by the reversal. Specifically, the NA values measured in S-C are higher than the values acquired in the other two directions in both *No Perturbations* and *Gain*. For what concerns the *Reversal* and *Reversal+Gain*, it turned out that the NA values in C-S are higher than the NA values in S-C, which in turn are higher than the NA values acquired in

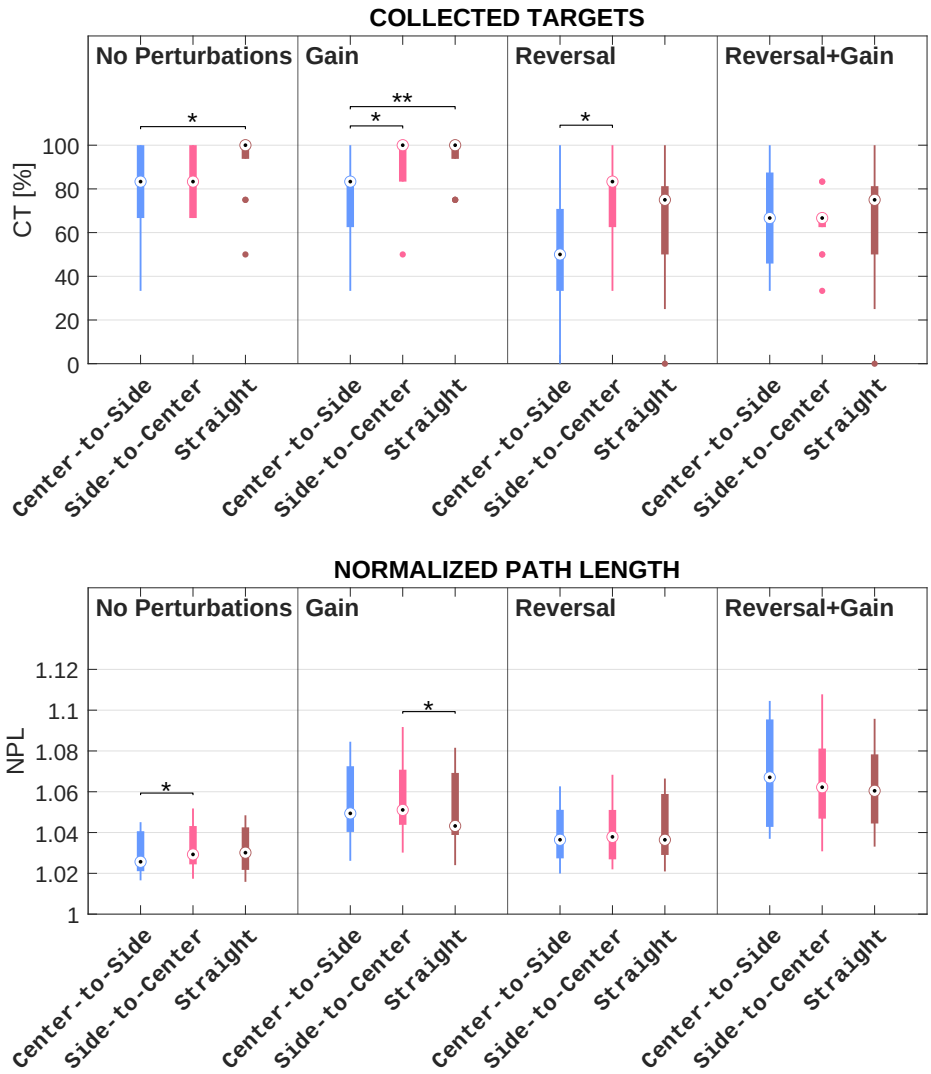

Fig. 1.12 The boxplot of the distribution of the chosen features computed in each direction grouped by mapping conditions with * representing statistically significant comparisons with $p < .05$, and ** representing statistically significant comparisons with $p < .01$

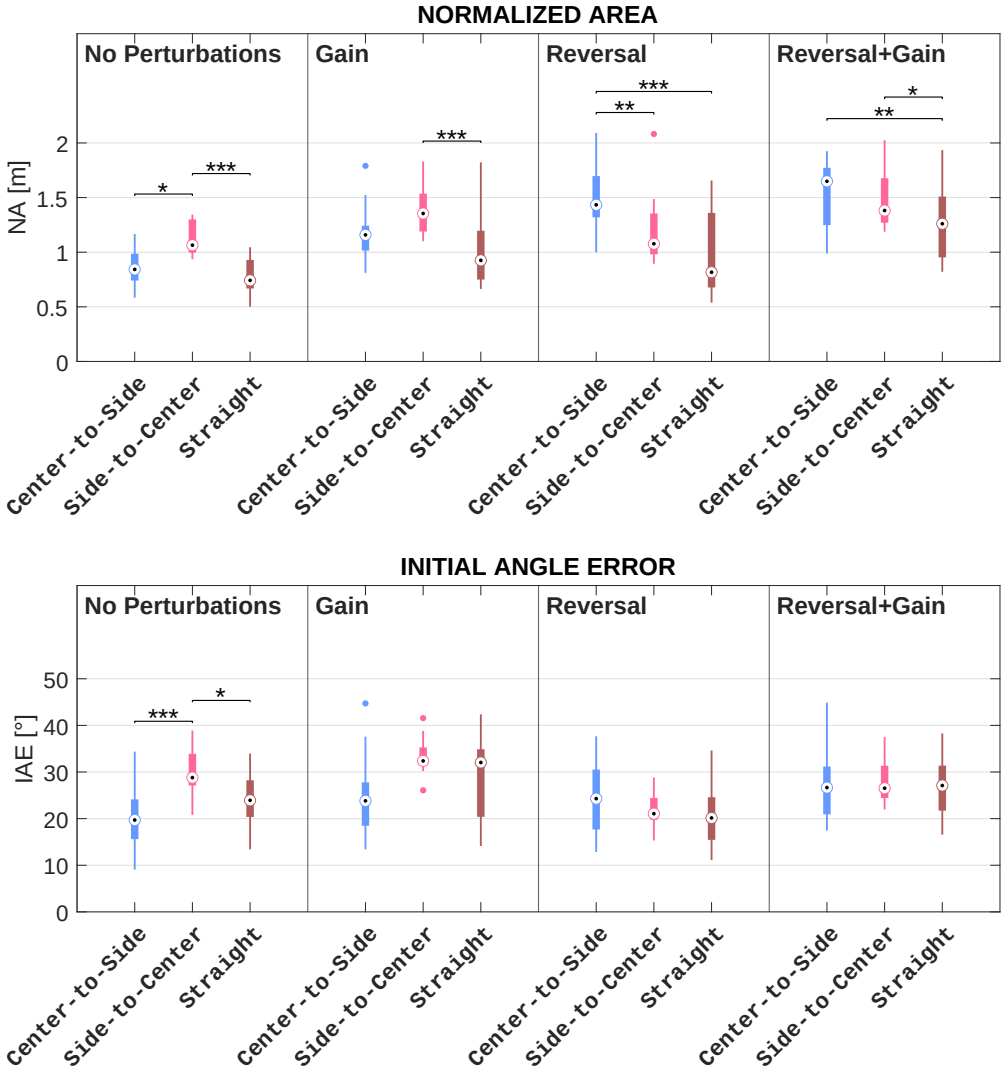

Fig. 1.13 The boxplot of the distribution of the chosen features computed in each direction grouped by mapping conditions with * representing statistically significant comparisons with $p < .05$, ** representing statistically significant comparisons with $p < .01$, and *** representing statistically significant comparisons with $p < .001$.

STR. More in detail, the NA in the C-S direction is higher than the one in the STR direction within all conditions, even if this relation has proven to be statistically significant only within *Reversal* and *Reversal+Gain*, with $p < .001$ and $p < .01$ respectively. Analogously, the NA in the STR direction lessens the one in the S-C direction within all conditions, although this difference is statistically significant only within *No Perturbations* and *Gain* with $p < .001$, as well as within *Reversal+Gain* with $p < .05$. The NA in the S-C direction is also higher than the one in the C-S direction within *No Perturbations* with $p < .05$ and *Gain* with no statistically significant differences; instead the NA in the S-C direction significantly lessens the one in the C-S direction within *Reversal* with $p < .01$, and within *Reversal+Gain* though with no statistically significant differences.

Ultimately, the IAE has proved by Friedman's test to be significantly different among directions only within *No Perturbations* with $p < .001$; post-hoc analysis has revealed statistically significant differences among directions within *No Perturbations*. In particular, the IAE values in the C-S direction are lower than the ones in the S-C direction within *No Perturbations* with $p < .001$, and within *Gain* though with no statistically significant differences; on the other hand, the median in the C-S direction is either slightly higher or equal with respect to the one of the S-C direction within *Reversal* and *Reversal+Gain*, respectively. Similarly, the IAE in the C-S direction is lower than the one in the STR direction within *No Perturbations* and *Gain*, although not significantly, whereas the IAE median in the C-S direction is either slightly higher or equal with respect to the IAE median in the STR direction within *Reversal* and *Reversal+Gain* respectively. Furthermore, the IAE in the STR direction is lower than the one in the S-C direction within *No Perturbations* with $p < .05$, as well as within *Reversal* although with no statistically significant differences; on the other side, the IAE median in the STR direction is equal to the IAE median in the STR direction within *Gain* and *Reversal+Gain* respectively.

1.2.4 Discussion

This work presents a VR-based framework that has been designed and implemented to evaluate the visuomotor adaptation capabilities during locomotion tasks. The experimental protocol considers a subject who is asked to directly control the position of an embodied avatar in a custom virtual world with the goal of collecting random objects that appear along a predefined path. The real locomotion task is performed on a treadmill, which allows a translation of the subject's pelvis along the mediolateral axis. The positional mapping between the subject and the avatar can be altered in specific phases of the game to assess the

adaptation abilities of the subject by introducing two kinds of perturbation: the amplified and reversed movement of the avatar with respect to the subject's one. The proposed framework integrates also a set of scores/metrics that can be used to quantitatively evaluate how well the task has been performed in each phase of the game. Such metrics are the percentage of collected targets (CT), and three variables extracted from the trajectories covered by the avatar during the game: the normalized path length (NPL), the Normalized Area (NA), and the Initial Angle Error (IAE). It is worth mentioning that the more the value of any trajectory-based feature, the worse the performance and the more challenging the exploration task.

Thirteen healthy children were recruited to preliminary test the proposed system and validate the designed set of metrics. Each subject was asked to collect 64 objects placed in a pseudo-random position along the path. As described in Paragraph 1.2.2.2, four different kinds of mapping have been tested during each session: *No perturbations*, *Gain*, *Reversal*, and *Reversal+Gain*. During the experimental sessions, the framework proved to be safe, since participants neither have reported any forms of sickness nor have risked falling. Besides, subjects' motivation has been preserved through a quick initial calibration procedure, a markerless tracking configuration, an intuitive interface for clinicians, and a realistic gait simulation that is tailored to individual motor abilities and anthropometric characteristics.

Concerning the tested experimental protocol, the virtual objects have been placed so that the avatar should ideally move in three directions within the virtual road to ensure a path variability, i.e., straight (STR), center-to-side (C-S), and side-to-center (S-C), under the four mapping conditions. In order to evaluate the capability of the visuomotor perturbations in making the task more difficult and validate the relevance of the proposed features, a set of comparisons has been performed and here listed:

- Comparison 1 - among mapping conditions;
- Comparison 2 - among mapping conditions grouped by directions;
- Comparison 3 - among directions grouped by mapping conditions.

The quantitative results related to all comparisons and metrics have been presented and reported in detail in the previous subsection. The results have surely shown that there are statistically significant differences among both the proposed mapping conditions and the different considered directions for all computed metrics. Even though the presented work is not a proper/traditional motor control or motor learning study, the obtained results have been deeply analyzed and the related discussion are reported below. The proposed

comparisons and the corresponding argumentations might be useful to analyze the results that would be observed in a study designed to examine human motor control under visuomotor perturbations in either healthy or pathological subjects. Before running all the experimental sessions, the following hypotheses were made:

- the *Reversal* is more challenging than the *Gain*, and *Reversal+Gain* is more difficult than *Reversal* and *Gain*;
- the targets positioned along the STR direction are easy to pick, since no movement along the ML axis is required if the previous object has been collected.

Visual perturbations have effectively made the exploration task more complicated (see Subsubsection 1.2.3.2). Analyzing the comparisons among the mapping conditions, it turned out that the "reversal factor" (see *Reversal* and *Reversal+Gain*) had a higher influence on the percentage of collected targets and the normalized area, whereas the "gain factor" worsened the values of normalized path length and initial angle error. These results indicate that the reversal actually makes the target difficult to collect, whereas the gain produces several corrections of the trajectory, i.e., higher NPL values, and an initial bigger deviation, i.e., higher IAE values.

When comparing the different mapping conditions within each specific direction (see Paragraph 1.2.3.2), it emerged that the observed differences for the percentage of collected targets and the normalized path length are similar to the general differences among the values averaged among the directions. Such similarity in terms of relative differences is also confirmed for the normalized area and initial angle error with the exception of the Center-to-Side direction. In fact, in this specific direction, the relation between the metric values acquired during the "reversed" mappings and the ones acquired during the "not reversed" mappings is different if compared with the general comparison (see Subsubsection 1.2.3.2). In particular, the Center-to-Side direction seems to require more effort than the other directions. The following motivation could explain such results: if the avatar is at the center of the virtual road and the target is on the side, the subject has a higher chance to choose the wrong direction since he/she can physically move either on the left or on the right; on the contrary, if the avatar is on the side of the road (this means that the subject is on the side of the treadmill) and the target is at the center of the road, the movement allowed to the subject can only be in one sense because of the physical boundaries, i.e from the side on the center of the treadmill.

This work also focused on the direct comparison of the values acquired in each direction for each specific mapping condition (see Paragraph 1.2.3.2). The normalized path length is a metric that is almost independent of the direction of the path towards the target. More

specifically, Straight has proved to be the direction in which picking up objects is easier than in the other directions, since both CT and NA values in the STR direction are better than the ones acquired in both the C-S or S-C directions within almost all mapping conditions. On the other hand, the collection task was more complicated in the C-S direction than in the S-C direction when a reversal is introduced, since the CT, NA, and IAE in the C-S direction are worse than the ones in the S-C direction within *Reversal*. Interestingly, the angular error obtained in the S-C direction is worse than in either the STR direction or the C-S direction when no reversal is applied, as IAE in the S-C direction is higher than the one in the remaining directions within *No Perturbations* and *Gain*. This may be due to the fact that subjects tend to align as soon as possible the avatar to the target location, i.e., the center of the road, thus increasing the angular error at the beginning of the trial.

1.2.5 Conclusions

This work presents a framework based on serious games in virtual reality for the evaluation of visuomotor adaptation (VMA) capabilities during a motor task. This latter consists in the control of a whole-body avatar in a visually perturbed virtual scenario while walking on a treadmill. Besides, the serious game has ensured participants' motivation during experimental sessions by means of quick calibrations and a realistic gait simulation of the avatar, which is supposed to collect virtual targets pseudo-randomly positioned along the virtual path. All the performed experimental sessions have qualitatively proved the feasibility of using the framework in a clinical context, due to the setup safety and the software user-friendliness. In addition, it effectively stimulated visuomotor adaptation through the mapping alterations (e.g., gain and reversal of the avatar's position along the ML axis), as encoded by a set of metrics that is made up of the percentage of collected targets and three features extracted by the avatar's trajectory. The comparison of the computed metrics in different game conditions has demonstrated the efficacy of the implemented visuomotor perturbations and the validity of the introduced metrics in describing the quality of the performed task. Most notably, the results indicate that the reversal increases the difficulty of the object collection, whereas the gain leads to correct the trajectory many times and to deviate with a higher angle at the beginning of the trajectory. The main limitation of the study is related to the experimental sample size, which is unarguably small. Such a limitation could be the beginning of a further recruitment campaign aimed to perform future investigations in the field of either motor control or motor learning. Another important limitation of the study is represented by the fixed succession of the mapping conditions, since the results might be biased by the

learning effect. Furthermore, the proposed system may be exploited in practical clinical settings since it might offer novel insights into the quantitative assessment of neuro-motor disorders. Several objective parameters can be measured and exploited for analyzing gait, as well as to corroborate studies that are focused on human upper districts. In addition, new proposed biomarkers may be correlated with traditional clinical scores that are associated with pathological conditions of either a cognitive or a motor nature. Such deep study could be used to better cluster the patients with the aim at proposing customized and targeted therapies. Therefore, the proposed feature-based approach can pave the way for clinical assessments of pathologies that determine either motor or cognitive impairments: for instance, VMA capabilities can be assessed to study the alteration of the sense of agency in children with cerebral palsy. In so doing, it would be possible to integrate and enhance the conventional rehabilitative programs by giving additional biomarkers and thus propose new solutions to integrate the existing clinical pathways [95]. In addition, a HMD may be used to design balance experiments while offering an even higher sense of embodiment through a more immersive experience and allowing for the simulation of high-fidelity in a safe manner [96–99]. However, specific feasibility tests must be run since an excessive mismatch between real and virtual movements with an HMD might cause cyber-sickness effects [100, 101] and serious losses of balance [102]. Ultimately, another important challenge that might be addressed concerns the possibility of using artificial intelligence to automatically adapt the game difficulty to the specific capabilities of the subject by the real-time analysis of the variables and metrics recorded by the system [103].

1.3 A Novel Framework Based on Deep Learning Architecture for Continuous Human Activity Recognition with Inertial Sensors

Frameworks for human activity recognition (HAR) can be applied in the clinical environment for monitoring patients' motor and functional abilities either remotely or within a rehabilitation program. Deep Learning (DL) models can be exploited to perform HAR by means of raw data, thus avoiding time-demanding feature engineering operations. Most works targeting HAR with DL-based architectures have tested the workflow performance on data related to a separate execution of the tasks. Hence, a paucity in the literature has been found with regard to frameworks aimed at recognizing continuously executed motor actions.

This section presents the design, development, and testing of a DL-based workflow targeting continuous human activity recognition (CHAR). The model was trained on the data recorded from ten healthy subjects and tested on eight different subjects.

This section is organized as follows: Subsection 1.3.1 illustrates the related works in the context of human activity recognition; Subsection 1.3.2 describes materials, which includes the system for collecting inertial data during the execution of ADLs, and the methodology adopted in this work, which comprises a preprocessing phase, a DL architecture based on a custom CNN, and statistical analysis. The outcomes of the ADLs classification are provided and discussed in Section 1.3.3 and discussed in Subsection 1.3.4. Ultimately, Subsection 1.3.5 draws the final remarks about the conducted study and delineates ideas for future works.

1.3.1 Related Works

The recent advances in medicine have improved life conditions and increased life expectancy so that healthcare systems have to cope with the aging of the global population [104, 105]. In addition, there are multiple categories of people experiencing motor disorders, from Parkinson's patients [106] to post-stroke individuals [107]. The psycho-motor frailty of these subjects can result in sedentary lifestyle choices that may aggravate their condition, thus raising the impact on the health system [108]. On the contrary, to pursue safety and well-being, the degeneration of their motor skills ought to be prevented by stimulating beneficial motor behaviors like an active lifestyle; therefore, recognizing activities of daily living (ADLs) can help monitor human habits and assess motor actions [109].

The scientific literature has given more and more attention to the field of human activity recognition (HAR), which aims to classify human actions by exploiting sensor data [110]. HAR has covered various contexts, from industry [111, 112] to sport [113], but a wider application lies in the medical field [110, 113–117]: in this realm, subjects' activities can be remotely registered outside the clinic [118] and clinicians can evaluate their functional abilities after treatment [119, 120]. HAR can also enhance a rehabilitative program inside the clinic for the sake of an assist-as-needed approach: in particular, recognizing the motor actions performed by patients (e.g., post-stroke individuals or people with psychomotor dysfunction) can allow for correcting motions or encouraging further exercise when required [121].

In addition, even patients with mental disorders (e.g., children with autism spectrum disorder) can be continuously monitored so that stereotypical actions (e.g., arm flapping) that are symptoms of anxiety may be identified and promptly counteracted [122].

A typical HAR experimental protocol encompasses a set of activities that the subject is asked to perform. These motor tasks may involve mainly upper body [112, 123], or lower body (e.g., walking or climbing/descending stairs) [118, 120, 124, 125], or even require the individual to drive upper- and lower-extremities in a proper combination (e.g., lying in bed) [126–132]. Furthermore, the protocol to collect data for HAR purposes tends to be designed such that ADLs are performed separately, i.e., a batch of repetitions of one of the activities to be recognized is asked to be executed by every subject [28]. However, this separate execution does not account for the continuous nature of human activities, which are more likely made successively [27]; therefore, the data collection should entail the recognition of uninterruptedly performed ADLs, namely continuous human activity recognition (CHAR) [30]. Such workflow can address the natural transition from one activity to another that humans execute in daily life, thus making the recognition system more spendable in the field of remote health monitoring [27].

A framework targeting HAR comprises two main components: the acquisition system, which collects several signals that are descriptive of the movement performed by the subject, and the classification pipeline, which processes the collected data and returns the type of activity [132].

The acquisition system may differ in the type of adopted sensors and the modality employed to acquire the signal describing human movement. There exist two main categories in which to classify the type of sensors: fixed sensors (e.g., videocameras, proximity and light sensors) are installed at specific locations of the environment and monitor activities in a confined area, whereas wearable sensors are directly worn by the subject, as in the case of inertial measurement units (IMUs), pressure and heart rate sensors [108]. Though being previously utilized to accurately label activities [109, 118], fixed sensors like cameras are not very suitable when ADLs execution requires subjects to move outside the area covered by them [127]; besides, cameras suffer from variable illumination, occlusion occurrence, presence of shadows, and time-varying contrast, especially in outdoor environments; such disadvantages, together with privacy issues and their lack of portability prevent them from continuously monitoring human activities [133]. In light of these limitations, most of the research in the HAR field, especially for remote monitoring, has preferably adopted wearable sensors because of their low cost and higher flexibility in providing continuous monitoring [134].

The number of types of sensors comprised in a HAR-oriented setup leads to distinguishing two approaches for data acquisition, which are unimodal and multimodal approaches. The unimodal approach refers to the use of only one modality (i.e., type of sensor) [111, 129–

131, 135], whereas the multimodal approach aims to integrate data from different sources by using multiple types of sensors, e.g., wearables like electromyography (EMG) sensors [125]. However, EMG signals are not widely used in HAR frameworks since their measurement are affected by electrical noise and motion artifacts due to human sweat [136]. Therefore, most of the frameworks addressing HAR have focused on the unimodal approach, thanks to which information from different sensors of the same type (e.g., IMU sensors) can be integrated [105, 137–139]. Ultimately, the acquisition paradigm of a HAR system exploiting IMUs may change according to the configuration of the sensors, which is given by both their number and their location on the human body. The amount of sensors in a HAR-targeting setup depends on the activities to be recognized: the exploitation of a single sensor may be enough when ADLs require to drive only one degree of freedom of one human joint (e.g., wrist flexion/extension in case of upper-limb driven actions [123] or leg extension from sitting position and leg flexion from standing position for lower-limb tasks [140]); on the other hand, a higher number of sensors is needed in case of more complex ADLs that target multiple joints (e.g., walking, sitting on a chair, lying-down on a surface). The activities to be classified have an impact on the sensor placement, which may be determined starting from anatomical landmarks which are body areas that are close to anatomical points of interest (e.g., lower-limb joints for recording human locomotion).

The recognition of human actions in a workflow targeting HAR requires a pipeline entailing a sequence of steps that may include data processing, feature extraction and artificial intelligence (AI) techniques to perform classification: at first, the signals acquired from sensors are processed to reduce noise [141], cope with missing values and remove possible artifacts [112, 142]; secondly, data are segmented to identify the portion of the preprocessed signals that are informative of the executed activities [143]; signals can be optionally converted into images as well [118, 120, 123, 131, 144, 145]; afterward, features are extracted for each segment from either images or time-series data [104, 105, 138, 146] to capture meaningful characteristics of the performed activities; ultimately, these features and their corresponding ground truth labels are used as input to train a classifier, whose performance is evaluated based on quantitative criteria, such as accuracy [11].

The HAR-oriented pipeline may differ according to the AI model used to discriminate ADLs. On the one hand, Machine Learning (ML) procedures are trained on hand-crafted features [127, 132], but implies a manual extraction based on domain knowledge that can be increasingly time-consuming as the dataset dimensionality enlarges due to the need for the high amount of repetitions and subjects for the sake of generalizability [131]. On the other side, Deep Learning (DL) architectures can be directly fed by raw data and automatically

learn patterns through the process of backpropagation without any prior knowledge of the signals [11].

Convolutional Neural Networks (CNNs) are the most widely employed among the DL architectures proposed in the studies addressing HAR [30, 111, 125, 126, 130, 138, 143, 146]. CNNs usually work on images by means of two-dimensional convolutions for practical problems as defect detection [11, 147]; notwithstanding, their one-dimensional variant is preferred because it allows working directly on time-series signals instead of their corresponding images, thus reducing the computational cost [30]. Furthermore, CNNs employed in HAR frameworks may have either a sequential or a multi-branch structure: in the former case, layers process all the IMU signals of the input dataset [126], whereas in the latter case each branch, which may be fed by one of the IMUs included in the experimental setup, is computed in parallel with the others [111, 130].

1.3.2 Materials and Methods

The framework that is proposed to address continuous human activity recognition is comprised of two main stages, which are a data collection stage explained in Subsubsection 1.3.2.1, and a classification pipeline reported in Subsubsection 1.3.2.2.

The acquisition of inertial data is accomplished by means of four IMU sensors, whose components are given in input to a DL-based model. For the sake of performing CHAR, this architecture is trained on IMU signals coming from multiple separate executions of four ADLs before being tested on the inertial data that are related to a multiple uninterrupted execution of motor tasks. This framework targeting CHAR is depicted in Figure 1.14.

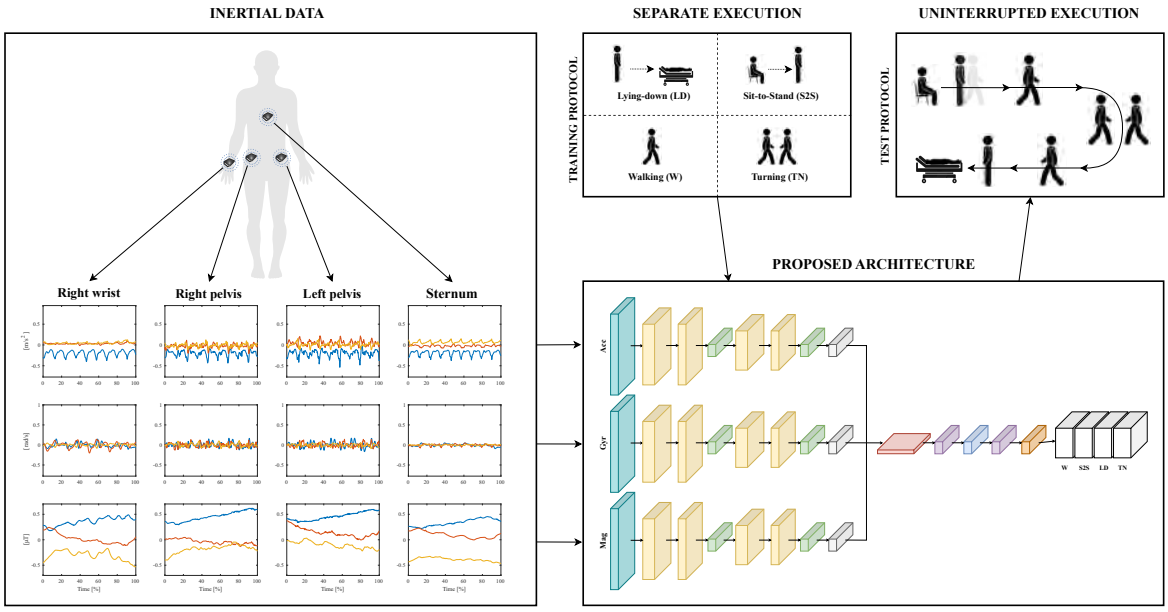

Fig. 1.14 The framework oriented to CHAR: inertial data are collected from four sensors placed on the human body; each component of the IMU sensors is used to feed a multi-branch DL-based architecture; this model is trained on the data related to a separate execution of four ADLs that are Lying-down (LD), Sit-to-stand (S2S), Walking (W), and Turning (TN); then, it is tested on the signals coming from motor actions that are performed uninterruptedly.

1.3.2.1 Data Collection

Participants Eighteen healthy subjects (34.94 ± 11.58 years old, eight males) are recruited from the staff of the IRCCS Maugeri (Bari, Italy). These participants differ in age, weight, height, and anthropometric characteristics (e.g., length of body segments) for the sake of higher data heterogeneity.

All subjects are right-handed with no motor or cognitive pathologies. Each subject is informed about the execution of the required activities prior to the experimental session. Besides, they were asked to perform tasks freely (i.e., with no restrictions on their body movements) to resemble a daily life situation.

Activities The activities to be executed were defined in accordance with the clinical staff of the IRCCS Maugeri. Four ADLs were selected among the ones identified as the most frequently performed in everyday life in a survey about ADL occurrence in HAR datasets [148].

The ADLs of this study differ in their biomechanical characteristics and can be described as follows.

- *Walking* on a surface with no asperities mainly requires alternating flexion-extension movements of the three lower limb joints (i.e., hip, knee, ankle) and may be combined with arm swinging. Note, that leg motion during walking is often associated with arm swinging to provide increased balance.

- *Turning* while walking typically requires the coordination of various movements, including the intra- and extra-rotation of both lower-limb joints (mainly hips) and trunk.

- *Sit-to-stand* transition, i.e., rising from a chair, principally entails hip and knee extension, as well as trunk rotation to bend/straighten the torso for keeping balance; it possibly involves additional leverage on arms or hands when the individual needs them for a lift that is both greater and safer.

- *Lying-down* on a surface (e.g., a couch), consists of two phases: the subject first reaches a sitting position, and then moves to the lying position through motor actions that mostly include hip and knee flexion/extension, trunk rotation and hip and knee abduction/adduction. In addition, this transition from the standing to the lying position can be supported by recruiting the wrist to lean hands on the couch for the sake of either a safer or a more comfortable motion. Subsequently, this motor action is completed by fully relaxing the body with the flexion/extension of the hip, knee, and trunk, as well as by resting their hands and arms on the bed.

IMU Sensors The number and placement of IMUs must be properly designed since they can have an impact on the performance of a HAR pipeline.

Hence, four sensors have been chosen and placed on the two sides of the human pelvis, the right wrist (i.e., the wrist of the dominant arm), and the sternum (see Figure 1.15), since they are anatomically close to the human joints that are driven during the execution of the selected ADLs. More in detail, the bilateral placement on the pelvis enables accurate monitoring of the pelvis movements; the sensor on the right wrist is essential for recording the arm swing that assists walking, as well as the use of hands to support lying-down action; the sensor placed on the sternum is useful to monitor the trunk, which mainly contributes in sit-to-stand and lying-down activities.

These sensors are attached to the subjects by straps because they are easy to wear and adaptable to the different body sizes of the subjects.

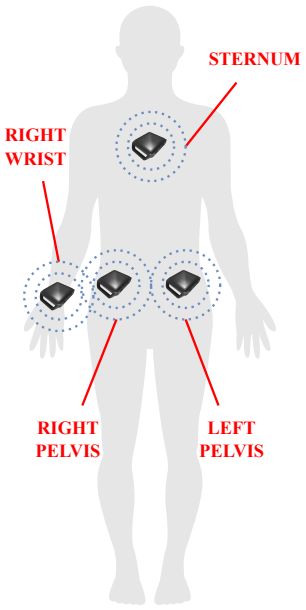

Fig. 1.15 The placement chosen for the sensor in the proposed framework: two IMUs are located on the two sides of the human pelvis to monitor motor actions driving the lower limbs (e.g., walking, sit-to-stand, lying-down); one sensor on the sternum serves to register the trunk contribution to accomplishing sit-to-stand and lying-down activities; the sensor on the right wrist (i.e., the wrist of the dominant arm) aims at acquiring the possible use of hands during lying-down, as well as the arm swing while walking.

The experimental data are collected with the Motion Studio system by APDM (APDM Inc, Portland, OR, USA, https://apdm.com (accessed on 15 January 2024). The system (see Figure 1.16) consists of the following three main components:

- a set of wireless body-worn IMUs, called OpalTM sensors, measuring 43.7 $\times$ 39.7 $\times$ 13.7 mm (LxWxH), each with a docking station;
- an Access Point for wireless data transmission and synchronization of the independent sensors;
- the Motion Studio software to manage the acquisitions of the recorded data.

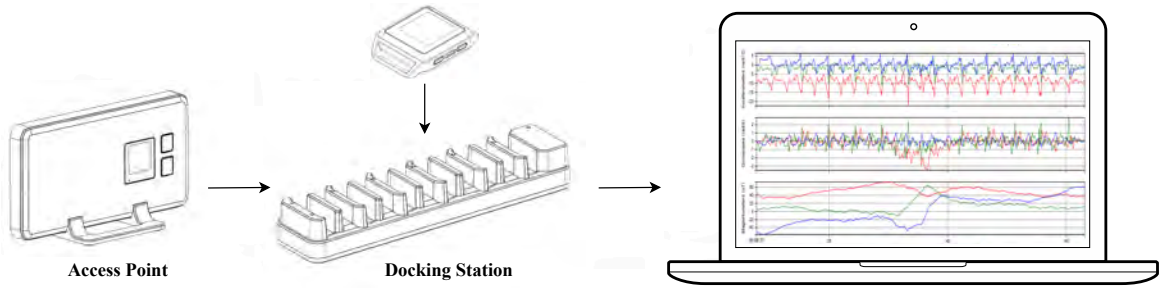

Fig. 1.16 Motion Studio system with IMU sensors, Access Point, Docking Station, and PC.

Each Opal sensor is wireless connected by Bluetooth communication protocol to a remote PC, and includes a 3-axis 14-bit accelerometer to measure linear acceleration, a 3-axis 16-bit gyroscope to record angular velocity, and a 3-axis 16-bit magnetometer for magnetic field intensity [149].

The Motion Studio software was used to record data in real time with a sampling rate of 128 Hz. Each recording session returns signals from the accelerometer, gyroscope, and magnetometer, whose combination has already proven to outperform a subset of IMU components in related works about HAR [150].

Experimental Protocol The experimental sessions are performed in the MARLab—Movement Analysis and Robotic Lab—of the IRCCS Maugeri in Bari (Italy). The protocol took approximately 40 minutes to be completed by each subject. A twofold experimental protocol ix proposed in order to entail the separate execution of ADLs for training and seamless ADLs for testing the proposed model. As a result, two datasets have been acquired to accomplish CHAR with the DL-based classifier.

One dataset, which is used for training the model, used 10 subjects (four males and six females) who performed each activity multiple times and separately, i.e., each subject repeated the three previously defined tasks one by one and repeated each of them 10 times. This dataset contains a total of 300 acquisitions, each corresponding to a specific activity. The experimental protocol for the training dataset has included three tasks (see Figure 1.17a) that are aimed at acquiring data related to the chosen ADLs. These motor actions have been conducted as follows.

- *Walking+Turning task*: the subject stands quietly for 30 seconds, walks for 7 m, turns 180 degrees counterclockwise around a pin, and walks back to the start point. In the end, the subject has to stand quietly for 5 s [149].

- *Sit-to-Stand task*: the subject sits on a chair with their heels at a reasonable distance for a comfortable execution of the task and keeps this position for 5 s. Next, the subject rises from the chair to reach a standing position, which they keep for another 5 s.

- *Lying-down task*: the subject keeps standing with heels at a reasonable distance from the bed for a comfortable execution of the task and keeps this pose for 5 s. After that, the subject lies down such that he/she feels comfortable, and keeps this lying position for 5 s.

A reasonable waiting time was allowed between two subsequent repetitions of each activity to prevent the subject's fatigue, which can alter the results [151, 152].

On the other hand, the other dataset, which is employed for testing the model used eight subjects (four males) who executed the above-mentioned activities continuously in a specific order, i.e., each subject performed tasks with no interruption in a predefined circuitry resembling a daily life scenario. Therefore, the experimental protocol for the test dataset is made up of the same ADLs as those of the training dataset, but such motor actions have been conducted in order to follow a predefined circuit (see Figure 1.17b): each participant starts from a sitting position and stands quite for 5 s; next, he/she gets up from the sitting position, walks for 7 m, turns clockwise 180 degrees, and then walks back for 7 m to reach the couch; after that, he/she turns in the preferred direction, lies down and keeps lying for about 5 s. After completing one execution of the circuit, subjects were instructed to wait a fair amount of time before the next repetition to prevent fatigue [151, 152]. Each recording of the test dataset is repeated five times per subject, for a total of 40 acquisitions.

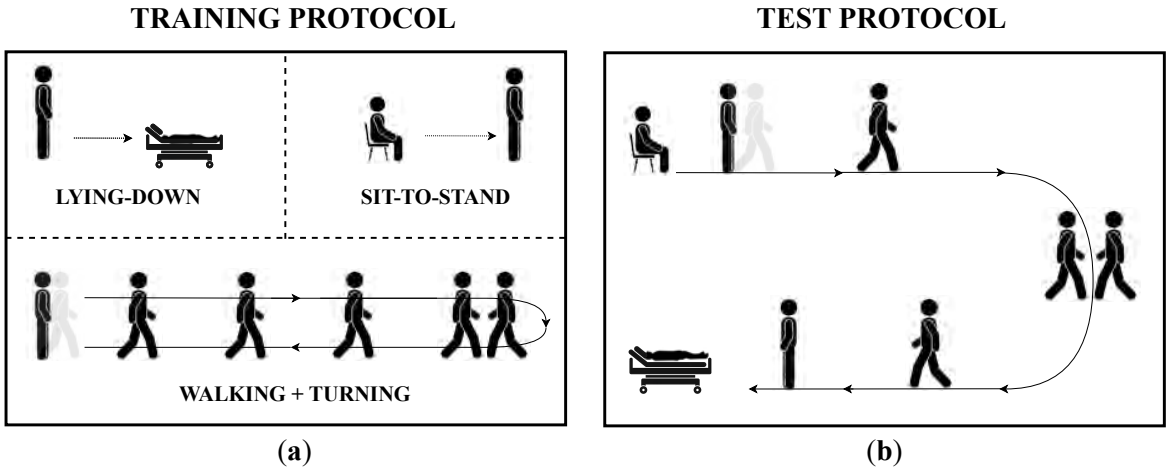

Fig. 1.17 The two experimental protocols encompassed in the study with the aim of continuous HAR: (**a**) the protocol for acquiring the training dataset encompasses an interrupted execution of motor tasks, which are Lying-down, Sit-to-stand, and Walking+Turning; (**b**) the protocol for collecting the test dataset requires subject to perform the same tasks without interruptions on a predefined path.

1.3.2.2 Classification Pipeline

This Subsubsection elucidates the CHAR-addressing pipeline, which includes a preprocessing stage (Paragraph 1.3.2.2), the details about the architecture and the training of the custom CNN classifying ADLs (Paragraph 1.3.2.2). Furthermore, the strategy for achieving the final prediction of activities is described in Paragraph 1.3.2.2, whereas the metrics used to evaluate the classification performance for all sensor combinations are reported in Paragraph 1.3.2.2 and compared in Paragraph 1.3.2.2.

Preprocessing The physical variable measured by the IMUs (see Paragraph 1.3.2.1) makes the values of one IMU component stay within a different range with respect to the values of the other components. This may result in extreme differences among input data and can worsen the capability of recognizing ADLs, as it is more complex to detect patterns in the data [153]. Therefore, a normalization operation is needed to achieve a uniform representation of the data. More specifically, the data of each IMU component have been normalized to lie in the range $[-1,1]$, as conducted in other related works about CHAR [27].

Signals coming from the IMUs used in a HAR workflow may comprise data that are not related to the motor tasks of interest, especially when some static periods (e.g., keeping a standing/standing/lying position) or transitions between two ADLs (e.g., stand-to-walk and walk-to-stand) are included in the dataset. Therefore, a data segmentation phase is needed to

identify the time frames in which data streams might contain relevant information about the target ADLs. Indeed, data were manually segmented by means of a signal inspection both for training and test datasets. These segments are then associated with a label representing the ground truth for the recorded activity for the sake of a supervised learning strategy [11].

A windowing procedure is applied both for training and test datasets to obtain an even higher amount of data to feed the proposed CHAR model. The window width must be informative enough to capture the performed activity [120]; nonetheless, an excessively wide window must be avoided to prevent a high computational cost and a classification delay that is not apt for the specific application [143]. As a consequence, it has been decided to adopt a step size of 128 samples, corresponding to 1 s, and an overlap of 64 samples, corresponding to 0.5 s. Such windows may be part of a longer window for which to classify ADLs [154].

The duration of one activity execution may change depending on the subject's characteristics, considering that an individual with motor disorders needs more time than a healthy one to accomplish the same task [155–157]; this results in a different number of windows that could not cover the entire length of the signal, thus causing a loss of information for the network. Therefore, IMU data are resampled such that the new signal length is an integer multiple of the window width to ensure that the windowing procedure keeps the whole signal.

Several factors can influence inertial data recorded for a CHAR experiment, thus making the ones related to a continuous protocol—i.e., related to a seamless execution of human activities—differ from those of a discontinuous protocol, i.e., related to a separate execution of ADLs. For instance, the structural characteristics of the environment may lead to rearranging the starting point of one motor action in order to keep the continuous nature of the protocol. As an instance, the starting point may swap with the ending point, thus changing the motion direction of the path related to the continuous protocol with respect to that of the discontinuous protocol, i.e., the subject turns counterclockwise in the former, but clockwise in the latter one. This gap in the operation condition is reflected in some components of the inertial signals from which the DL-based model learns patterns, thus potentially worsening the performance of the activity recognition [11].

Hence, for each subject of the training dataset, signals have been treated with a conventional data augmentation technique by flipping to reproduce the operational condition of the test dataset and improve the classifier robustness [158]. More specifically, Figure 1.18 visually reports the normalized magnetometer signal of the IMU sensor located at the left hip during the execution of sit-to-stand and turning tasks related to the test dataset (i.e., continuous execution), and to the training dataset (i.e., separated execution) before and after data augmentation. The operational discrepancy leads the magnetometer signal to be flipped

along the x-axis and z-axis for the turning action and along the x-axis and y-axis for the sit-to-stand task. Hence, such components of the training dataset have been flipped to make the magnetometer components of the training dataset resemble those of the test dataset.

On the other hand, the operational discrepancy is not reflected in accelerometer and gyroscope signals because, differently from the magnetometer data, linear acceleration, and angular velocity do not change according to the subject's position with respect to the position of the magnetic north. Hence, such components of the IMU sensors are not affected by the change in motion direction and they have not been flipped.

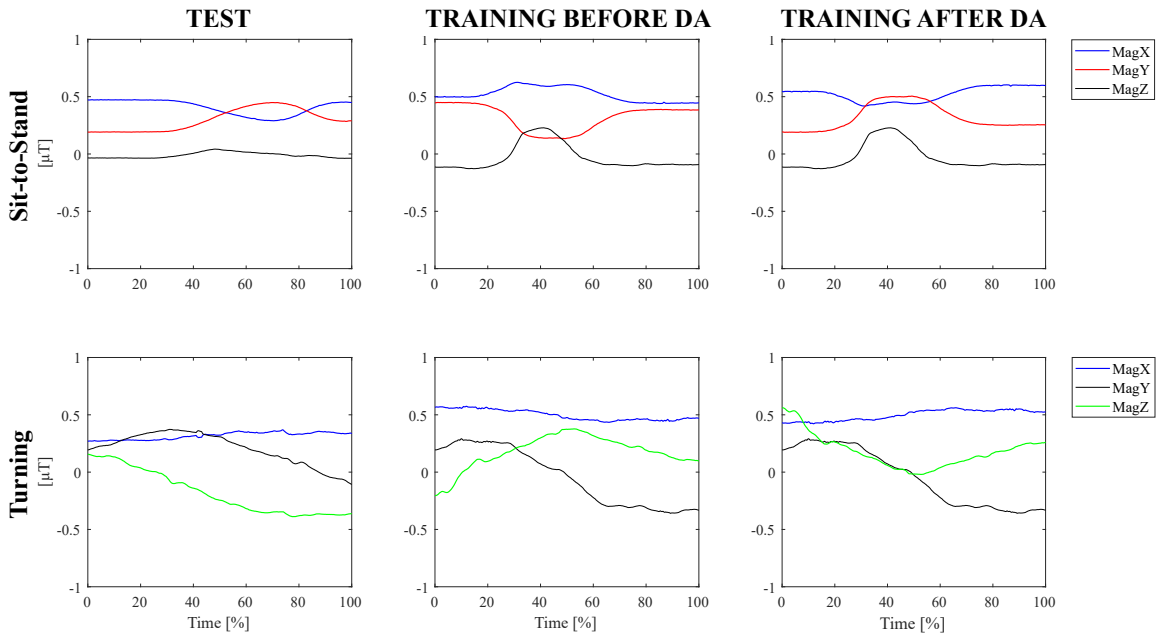

Fig. 1.18 Data augmentation technique to cope with operational differences.

In addition, the time needed to perform ADLs can be different for intrinsic characteristics of the task included in the protocol, since motor actions such as walking for seven meters last far more than standing from a chair. This difference in activity duration results in a different number of samples (i.e., windows) that feed the classifier; consequently, the dataset of IMU signals would be unbalanced towards the majority class (i.e., the motor action with the highest number of windows), thus leading to reduced classification performance [11]. Therefore, another conventional data augmentation technique for time series data is applied to compensate for the imbalance [158]. In particular, the signals of the minority classes (e.g., sit-to-stand, turning, lying-down) are scaled by a factor that can be either amplified or attenuated so as to simulate slight magnitude differences among the repetitions made by one

subject [4]. The number of trials of the above-mentioned activities has been increased, thus enlarging the volume of the collected data.

Sensor configuration, which is given by the number and placement of the IMUs adopted in the setup, can have a significant impact on the performance of the HAR system [139, 146, 153, 159]. Therefore, it might be useful to evaluate the different combinations of the sensors from which the inertial data feeding the model come. More specifically, this work is focused on those combinations involving two and three sensors, as well as all the four IMUs explained in Paragraph 1.3.2.1.

In light of this, each window of the pre-processed dataset is an array of size $W_l \times N_c$, where W_l is the window width and N_c is the number of sensor channels, which differs according to the combination of sensors to be evaluated: it is six for any sensor pair, nine for any sensor triple, and twelve for the combination with four sensors.

Custom Convolutional Neural Network In this work, a one-dimensional CNN for classifying ADLs has been employed, since they were successfully applied in related works about HAR [111, 125, 126, 130, 143, 146] and CHAR [30]. Specifically, the chosen architecture (see Figure 1.19) employs three distinct parallel branches to process signals from the accelerometer, gyroscope, and magnetometer simultaneously. This structure automatically extracts features from signals that have different physical meanings, thus allowing it to leverage all the data recorded by each sensor at the same time.

The input layer is fed by a multidimensional array whose shape is (N_w, W_l, N_c), where N_w is the number of windows in the input dataset, which may change across subjects and trials, W_l is the window length, which is fixed, and N_c is the number of sensor channels, which differs according to the combination of sensors to be evaluated (e.g., it is six for any sensor pair, nine for any sensor triple, and twelve for the combination with four sensors).

A grid-search method is employed to optimize the architectural characteristic of the 1D-CNN, i.e., determine the number of convolutional and dense layers, as well as the number of neurons that maximize validation accuracy [112, 138]. Therefore, each branch consists of two 1D convolutional layers using 128 filters and kernels of size 5 for the first and 3 for the second one, and one max-pooling layer. Next, two 1D convolutional layers use 64 filters and kernels of size 5 and 3, respectively, followed by a max-pooling layer. Then, a flattened layer reshapes data into a linear vector. All convolution layers are characterized by a *ReLu* nonlinear activation functions. Subsequently, all three branch outputs are concatenated in one linear vector, thus gathering the smaller previous outputs. This composite feature vector is then fed through two fully connected layers, each with 128 neurons, for learning

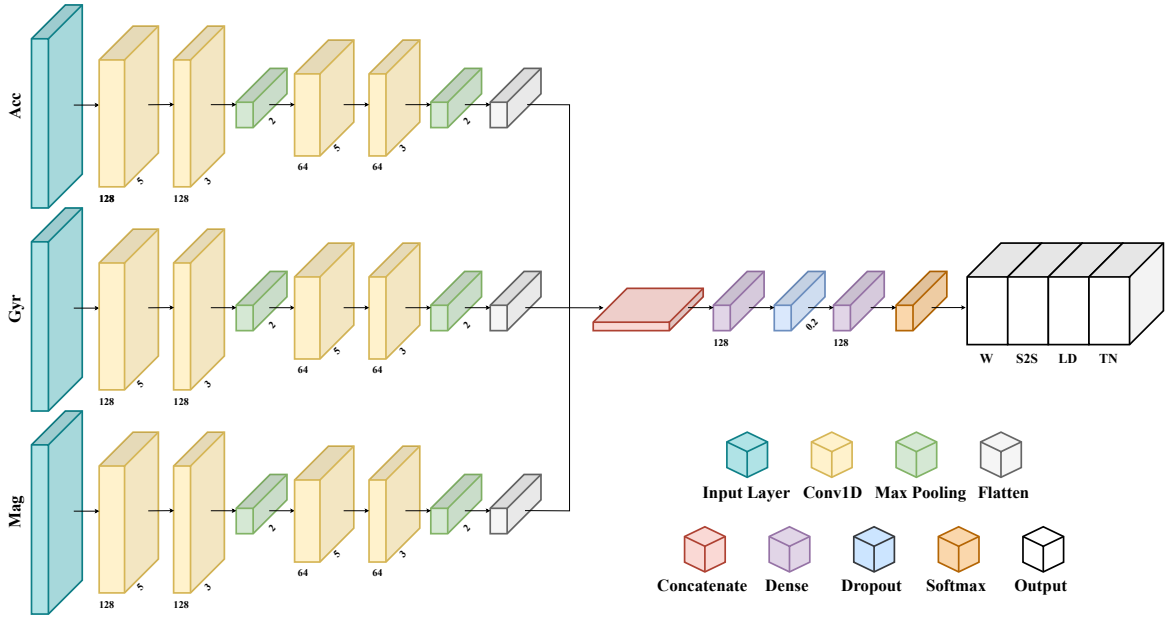

Fig. 1.19 The custom multi-branch CNN addressing CHAR.

more abstract representations of the data. The first one is followed by a dropout layer that switches off 20% of the neurons to prevent overfitting. Finally, an output layer with a softmax activation function is included to classify tasks into one of the four defined classes. This layer is responsible for the final prediction of activity labels, based on the representations learned from the input data.

The same heuristic on validation accuracy is used to select the model hyper-parameters, such as the optimizer, the learning rate, the batch size, and the number of epochs. The best performance is obtained by using a number of epochs of 200, a batch size of 64, and the Adam optimizer with a learning rate of 0.001. An early stop criterion monitoring the loss value on the validation set during the training is exploited; however, criteria accounting for other metrics (e.g., validation recall) can be used. Consequently, the value of the patience is set to 10 to stop the learning process prematurely if the value increases for 10 consecutive iterations on the validation batches.

For each combination of sensors, the dataset of the separate execution of ADLs was split into ten stratified folds, 75% of which is assigned for training and the remaining 25% for validation. Afterward, a 10-fold-cross-validation methodology is employed to ensure a fair and unbiased evaluation of the model [147]. All investigations in this study are conducted on the Google Colab-Pro framework to train the model on a Tesla T4. Tensorflow, Sklearn, Pandas, and Numpy libraries have been exploited for training and inferencing the CHAR-targeting architecture.

Classification Strategy Human activities are usually classified by applying a sliding-window technique on the input data, meaning that the prediction is given for each of the windows in which the signal is divided [120]. However, signal duration within a trial can differ across subjects, because people with motor impairment may need a higher amount of time to accomplish the task [155–157]. In light of this, monitoring ADLs for pathological individuals could admit a slightly slower classification by means of wider windows to enhance the accuracy of the final prediction of the performed motor action.

Hence, for each activity, it has been decided to propose a classification strategy that entails the combination of predictions coming from *sub-windows* of a single trial to achieve the model prediction related to a *grouped window* that lasts as in the trial [154]. Ultimately, the classification of the *grouped window* is given by the average of the predictions made on the *sub-windows*.

Performance Metrics The efficacy of the CHAR-oriented framework has been evaluated by means of two metrics. On the one hand, classification performance is measured through accuracy, since the input dataset has been rebalanced by means of data augmentation. The formula of this performance index is given below:

$$\text{ACC} = \frac{TP+TN}{TP+TN+FP+FN} \tag{1.1}$$

In such equations, TP, TN, FP, and FN represent true positives, true negatives, false positives, and false negatives, respectively.

On the other hand, the feasibility of the framework in a real-time clinical application is investigated by computing inference time [30]. For each ADL, this metric is calculated both for the *sub-windows* and *grouped windows* of each trial as follows:

- *sub-windows* inference time is the time that is necessary for returning the prediction from a single sub-window;
- *grouped-window* inference time is the time needed for returning the prediction from the single trial of the activity.

Hence, this metric is mathematically defined as follows:

$$\text{IT [s]} = t_{end} - t_{start} \tag{1.2}$$

In such equations t_{start} is when the inference procedure is started by giving the data in input, whilst t_{end} is when the inference process differs depending on the window type. More specifically, given a single trial of each ADL, t_{end} may be:

- the time in which the model returns a classification label for a single *sub-window*, in the case of *sub-windows* inference time;
- the time in which the model gives the classification output as the average prediction across *sub-windows* in the case of *grouped-window* inference time.

The proposed metrics are computed for each test fold to obtain a confidence interval distribution for each index [147].

Comparisons and Statistics Sensor placement can be impactful on the model performance of a workflow for recognizing human activities [139, 146, 153, 159]. Hence, the model has been tested on all the combinations entailing at least two of them, which are detailed in the following.

1. Combinations with two sensors:
   - *Right Pelvis* + *Left Pelvis* (RP+LP);
   - *Left Pelvis* + *Sternum* (LP+S);
   - *Right Wrist* + *Left Pelvis* (RW+LP);
   - *Right Pelvis* + *Sternum* (RP+S);
   - *Right Wrist* + *Right Pelvis* (RW+RP);
   - *Right Wrist* + *Sternum* (RW+S);
2. Combinations with three sensors:
   - *Right Pelvis* + *Left Pelvis* + *Sternum* (RP+LP+S);
   - *Right Wrist* + *Right Pelvis* + *Left Pelvis* (RW+RP+LP);
   - *Right Wrist* + *Left Pelvis* + *Sternum* (RW+LP+S);
   - *Right Wrist* + *Right Pelvis* + *Sternum* (RW+RP+S);
3. Combination with all the four sensors:
   - *Right Wrist* + *Right Pelvis* + *Left Pelvis* + *Sternum* (RW+RP+LP+S).

Such combinations have been statistically compared with the non-parametric Friedman's test since the hypothesis of a Gaussian distribution is excluded due to the limited number of tests. Besides, a pairwise post-hoc test with Bonferroni's correction was performed with a significance level set to $p < 0.05$. These analyses were conducted using MATLAB 2022b.

1.3.3 Results

This subsection presents the results of the continuous human activity recognition performed with the proposed DL-based framework: the outcomes of the efficacy of the classification strategy are reported in Subsubsection 1.3.3.1, whereas the results concerning the investigation of the optimal sensor configuration are described in Section 1.3.3.2.

1.3.3.1 Differences between Window Types

The classification performance of the CNN-based framework addressing CHAR has been evaluated in each fold for all combinations of sensors. Hence, many distributions have been obtained for the two window types described in Paragraph 1.3.2.2, i.e., sub-windows of a single repetition of the ADL and *grouped window* lasting the repetition itself, and for all metrics mentioned in Paragraph 1.3.2.2, which are accuracy and inference time.

Since two classification strategies have been applied, i.e., without and with averaging, the distributions of accuracy and inference time have been compared to investigate the impact of the averaging technique on both these metrics.

Table 1.1 contains the average accuracy of the CHAR-oriented model computed on ten-fold testing sets for each combination of sensors before and after averaging predictions.

Table 1.1 Average accuracy [%] on ten-fold testing sets for each combination of sensors with the two window types (e.g., *sub-windows* and grouped windows). The corresponding p-values are specified with a significance level set to $p < 0.05$ as well.

Combination	**Test Accuracy [%]**		***p* Value**
	Sub-Windows	**Grouped Window**	
RP+LP	75.42	88.75	**0.0001**
LP+S	65.94	81.44	**0.0001**
RW+LP	79.59	95.00	**0.0001**
RP+S	78.01	83.31	**0.0298**
RW+RP	79.64	82.31	0.1569
RW+S	77.74	89.88	**0.0001**
RP+LP+S	74.90	86.12	**0.0018**
RW+RP+LP	83.83	96.69	**0.0001**
RW+LP+S	80.33	95.75	**0.0001**
RW+RP+S	79.16	81.38	0.4212
RW+RP+LP+S	84.88	96.06	**0.0001**

The accuracy of the DL-based classification has been significantly boosted for almost all combinations of sensors passing from sub-windows to a grouped window, with an increment of about 15% for RW+LP and RW+LP+S with $p < 0.001$; however, the model tested with data related to RW+RP+LP outperforms the outcome corresponding to any other combination for both window types, since the classifier accuracy has significantly raised to 96.69% with $p < 0.001$.

Moreover, the average and standard deviation of inference time for 10 testing sets of each combination of sensors for each window type are reported in Table 1.2.

Table 1.2 Average and standard deviation inference time in seconds needed for the inference related to ten-fold testing sets of each window type with the two window types (e.g., sub-windows and grouped window). The corresponding p Values are specified with significance level set to $p < 0.05$ as well.

Combination	**Inference Time [s]**		***p* Value**
	Sub-Windows	**Grouped Window**	
RP+LP	0.21 ± 0.04	0.25 ± 0.07	0.1901
LP+S	0.22 ± 0.02	0.22 ± 0.02	0.3565
RW+LP	0.22 ± 0.02	0.24 ± 0.03	0.1820
RP+S	0.23 ± 0.01	0.25 ± 0.03	0.0684
RW+RP	0.23 ± 0.07	0.25 ± 0.03	0.4002
RW+S	0.23 ± 0.03	0.26 ± 0.07	0.1660
RP+LP+S	0.23 ± 0.03	0.25 ± 0.03	0.1678
RW+RP+LP	0.24 ± 0.07	0.26 ± 0.02	0.4601
RW+LP+S	0.24 ± 0.03	0.28 ± 0.07	0.1206
RW+RP+S	0.26 ± 0.05	0.29 ± 0.08	0.2706
RW+RP+LP+S	0.30 ± 0.09	0.33 ± 0.10	0.3803

The proposed 1D-CNN needs almost 300 milliseconds on average with a low standard deviation to recognize one activity performed with no interruption with the other ones. Furthermore, the average inference time has incremented, but not significantly ($p > 0.05$), for all combinations of sensors. Notwithstanding, such time stays in the order of magnitude of a few milliseconds.

1.3.3.2 Differences in Accuracy Among Sensor Combinations

Statistically significant differences were revealed for each performance index when comparing sensor combinations. The outcomes of the proposed metric for evaluating the efficacy of the proposed framework to address CHAR are pictorially depicted in the boxplot reported in Figure 1.20.

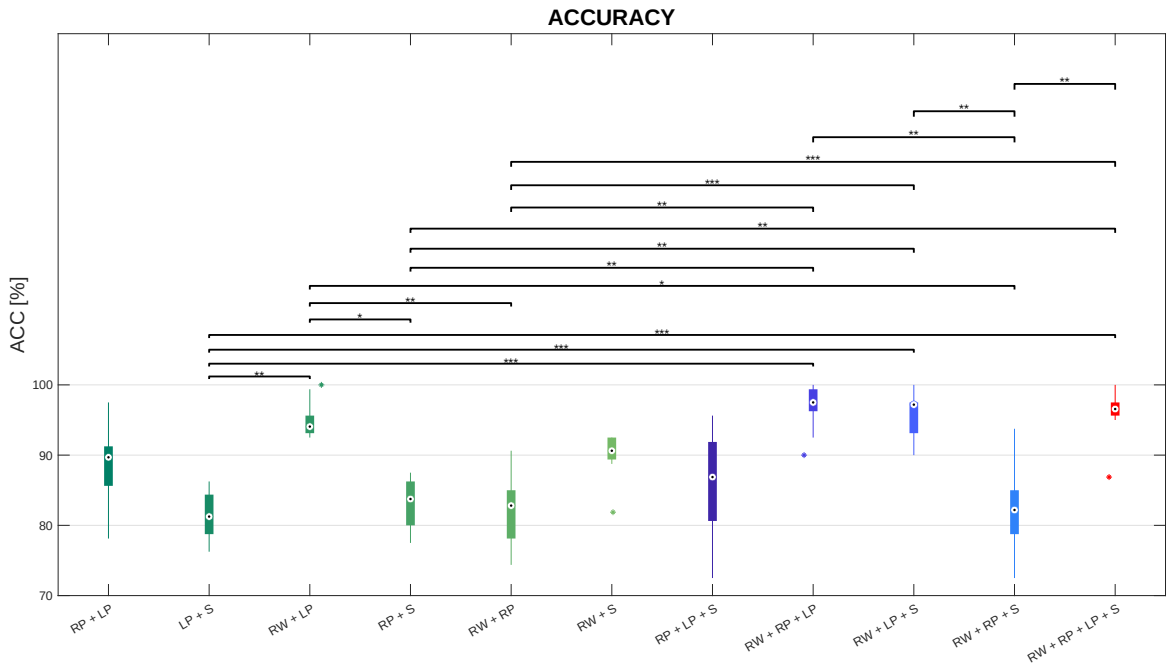

Fig. 1.20 Boxplots of accuracy distributions on the test set for each sensor combination, with *, **, and *** representing statistically significant comparisons with $p < 0.05$, $p < 0.01$, and $p < 0.001$, respectively.

Friedman's test revealed that ACC significantly differs among sensor combinations, with $p < 0.01$.

Regarding the comparisons among sensor configurations with two sensors, according to post-hoc tests, the ACC in the RW+LP combination is significantly greater than the ACC in both LP+S ($p < 0.01$) and RP+S combinations with $p < 0.05$, as well as than the ACC in RW+RP combination with $p < 0.01$. Instead, no statistically significant differences were found in the values of ACC between the RW+LP combinations and any other combination with two sensors. However, the RW+LP combination was revealed to be the best configuration with two IMUs placed at the *Right Wrist* (RW) and the *Left Pelvis* (LP). Similarly, slightly worse performance can be observed for the RP+LP and the RW+S combinations.

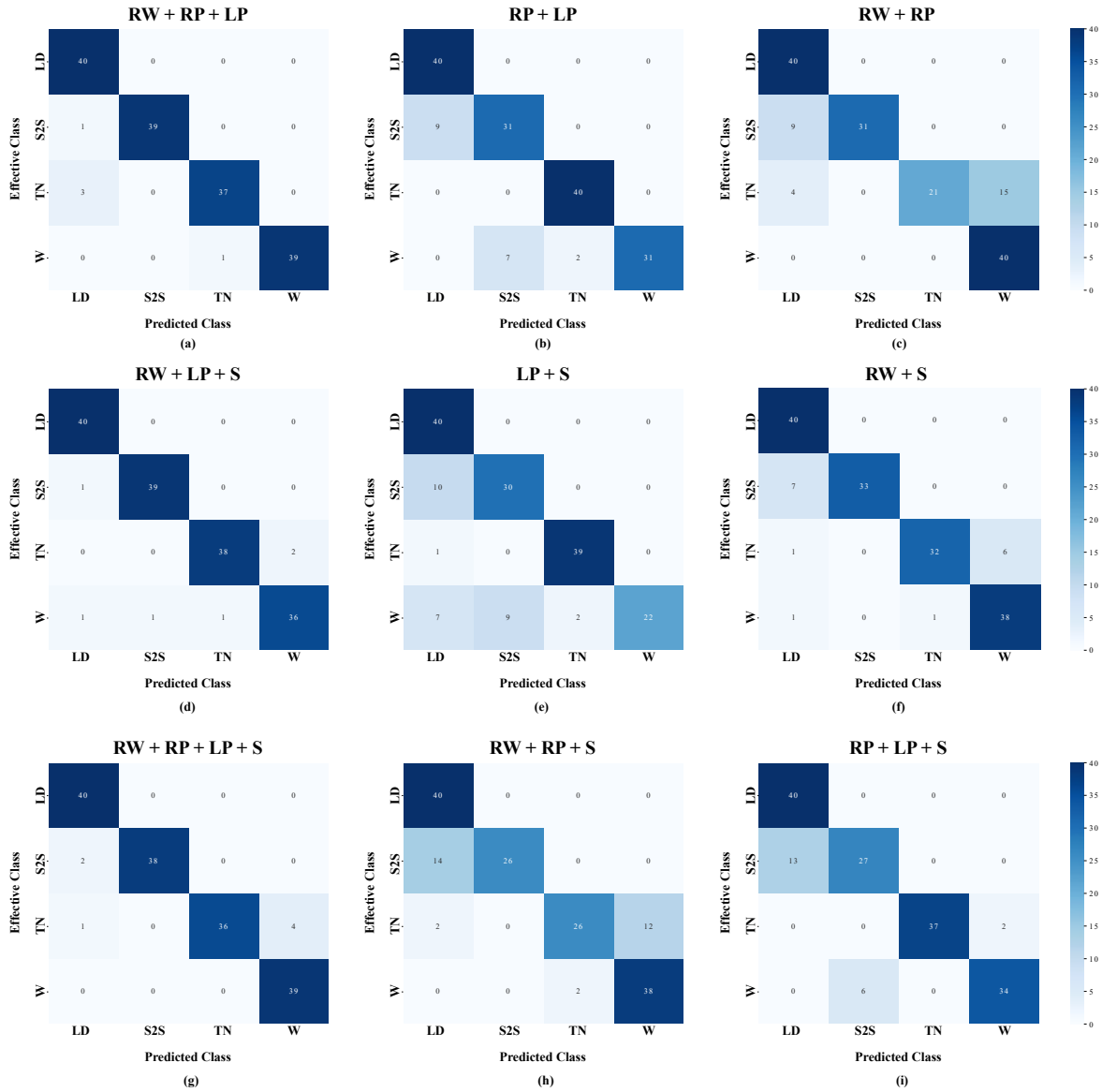

Fig. 1.21 Confusion matrices of the proposed model for continuous human activity recognition for three sensor configurations: (**a**) RW+LP+S means that inertial sensors are placed at the right wrist, the left pelvis, and the sternum; (**b**) LP+S means that inertial sensors are placed at the left pelvis and the sternum; (**c**) RW+S means that inertial sensors are placed at the right wrist and the sternum; (**d**) RW+RP+LP means that inertial sensors are placed at the right wrist, and the right and left pelvises; (**e**) RP+LP means that inertial sensors are placed at the right pelvis and left pelvis; (**f**) RW+RP means that inertial sensors are placed at the right wrist and the right pelvis; (**g**) RW+RP+LP+S means that inertial sensors are placed at the right wrist, the right and left pelvises, and the sternum; (**h**) RW+RP+S means that inertial sensors are placed at the right wrist, the right pelvis, and the sternum; (**i**) RP+LP+S means that inertial sensors are placed at the right and left pelvises and the sternum. The activities to be recognized are Lying-down (LD), Sit-to-stand (S2S), Turning (TN), and Walking (W).

Concerning the comparisons between each configuration with two sensors and each one with three sensors, posthoc tests showed that ACC in the RP+LP+S combination revealed no statistically significant difference with any sensor pair On the other hand, ACC in the RW+RP+LP combination is significantly higher than ACC in the LP+S combination with $p < 0.001$, as well as ACC in RP+S and RW+RP combinations with $p < 0.01$. Secondly, ACC in the RW+LP+S proved to be better than ACC in both RP+S with $p < 0.01$, as well as higher than ACC in LP+S and RW+RP with $p < 0.001$. Besides, ACC in the RW+RP+S combination significantly lessens ACC in the RW+LP combination with $p < 0.05$, but no other significant differences were found with any other sensor pair.

As for the comparisons among sensor triples, posthoc tests revealed that ACC in the RW+RP+S combination is the lowest one among sensor triples. More in detail, it significantly lessens ACC in the RW+RP+LP and RW+LP+S combinations with $p < 0.01$; ACC in the RW+RP+S combination is also slightly worse, though not significantly, than ACC in the RP+LP+S triple.

Considering the comparisons between the sensor quadruple and any sensor triple, according to the post-hoc test, the ACC median in the RW+RP+LP+S combination is almost comparable with ACC in the RW+RP+LP and RW+LP+S triples; on the other side, ACC in the sensor quadruple is higher than the one in RP+LP+S, though with no statistically differences; in addition, the RW+RP+LP+S combination outperforms the RW+RP+S one in terms of accuracy with $p < 0.01$.

Besides, this sensor quadruple is better than both LP+S and RP+S combinations with $p < 0.001$ and $p < 0.01$, respectively, as well as RW+RP with $p < 0.001$. The ACC median in the RW+RP+LP+S combination is even higher, but not significantly, than the one in any other sensor pair.

The outcomes depicted in the boxplots can be further investigated by means of the confusion matrices of the ten-fold testing sets. More in detail, the confusion matrices of the predicted activities against ground truth using RW+LP+S, LP+S, RW+S, RW+RP+LP, RP+LP, RW+RP, RW+RP+LP+S, RW+RP+S, and RP+LP+S combinations are shown in Figure 1.21.

Regarding the confusion matrix related to the LP+S combination, a misclassification can be observed between sit-to-stand (S2S) and lying-down (LD): besides, walking (W) is confused with both turning (TN) and S2S. Similarly, the confusion matrix related to the RW+S configuration shows that S2S is still confused with LD, and W is misclassified with TN in an even worse way. On the contrary, The confusion matrix related to the RW+LP+S combination decreases such misclassifications and improves the overall accuracy.

The confusion matrix related to the RP+LP combination reveals a misclassification between S2S and LD, as well as walking W is confused with either turning TN or S2S. Similarly, the confusion matrix related to the RW+RP combination shows that this configuration leads to confusing S2S with LD, as well as worsening the misclassification between W and TN. On the other side, The confusion matrix related to the RW+RP+LP triple reduces the number of false positives and false negatives, thus leading to enhanced overall accuracy.

As for the confusion matrix of the RW+RP+S triple, S2S is confused with LD, whilst TN is misclassified with W; furthermore, the confusion matrix of the RP+LP+S combination reveals a comparable misclassification between S2S and LD, whereas W is slightly confused only with S2S. Instead, according to the confusion matrix related to the RW+RP+LP+S configuration, a decrease in false positives and negatives is produced when using all sensors, thus ensuring a better performance in terms of accuracy.

1.3.3.3 Differences in Inference Time Among Sensor Combinations

This Subsection presents the results in terms of inference time compared among sensor combinations. Such comparisons are pictorially depicted in the boxplots reported in Figure 1.22.

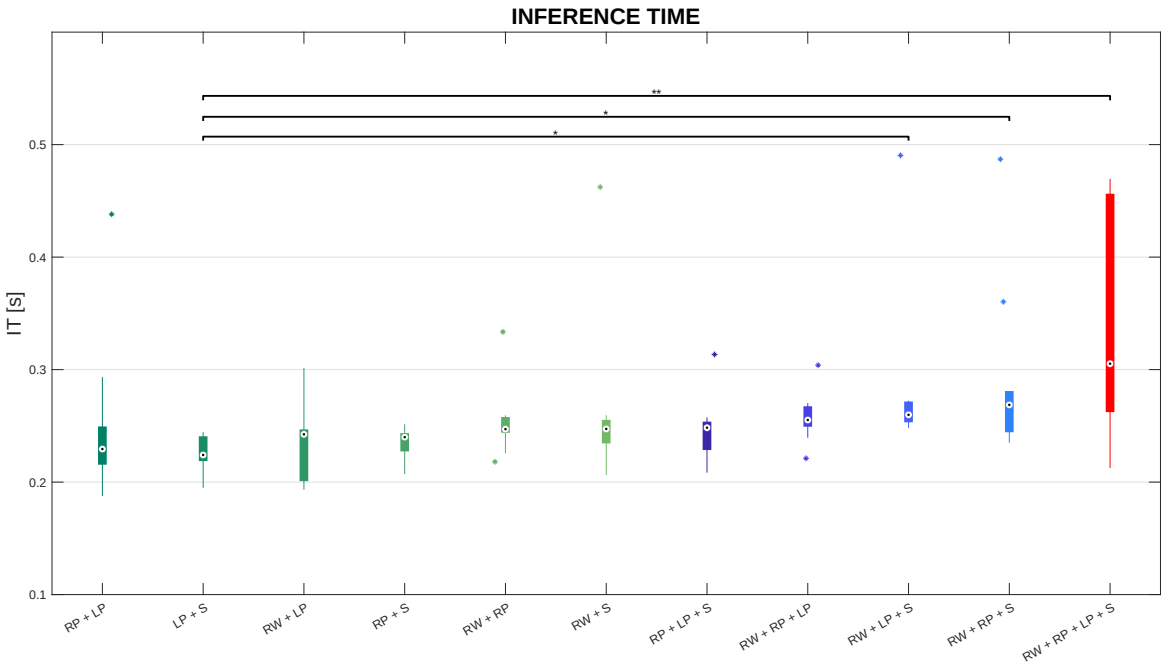

Fig. 1.22 Boxplots of inference time distributions on the test set for each sensor combination, with * and ** representing statistically significant comparisons with $p < 0.05$ and $p < 0.01$, respectively.

Friedman's test leads to statistically significant differences in IT among sensor combinations. Besides, post-hoc tests revealed that IT in the RP+S combination is significantly lower than IT in both RW+LP+S and RW+RP+S triples with $p < 0.05$, as well as inferior than IT in the RW+RP+LP+S configuration with $p < 0.01$. Inference time stays below 300 ms in almost all sensor combinations, except for IT in the RW+RP+LP+S combination whose distribution reached the highest values (almost 450 ms), but less than 1 s.

1.3.4 Discussion

This work presents a DL-based framework that is aimed to perform continuous human activity recognition (CHAR), i.e., the classification of activities of daily living (ADLs) with a custom convolutional neural network (CNN) that is fed by data acquired by means of inertial measurement units (IMUs) located at four body parts, which are the left pelvis (LP), right pelvis (RP), sternum (S), and right wrist (RW). The experimental protocol requires the subject to perform four ADLs, which are *Walking* (W), *Turning* (T) while walking, *Sit-to-stand* (S2S) and *Lying-down* (LD) on a surface, in two ways: On the one hand, ADLs are executed separately (i.e., every subject performs multiple repetitions of one of the motor actions before passing to the each of the other ADLs) to collect data for training the model; on the other side, the execution of motor tasks lies within a circuit (i.e., ADLs are performed uninterruptedly) to record signals for testing the workflow. Moreover, the CHAR is addressed first by employing a sliding-window procedure on the pre-processed IMU signals to predict the ADL in each of these *sub-windows*, and then by combining these outcomes to obtain the final prediction related to a wider window, i.e., *grouped window*. This classification strategy has already been proposed in one related work, but it was not tested on a dataset of human activities performed in a continuous way [154]. Two metrics are exploited to quantitatively evaluate the performance of the proposed framework: accuracy (ACC) serves to assess the capability of the model to perform CHAR, whereas inference time (IT) is aimed at ascertaining its feasibility in a real-time monitoring scenario. As described in Paragraph 1.3.2.2, all possible combinations of sensors made up of at least two IMUs were considered in order to determine the optimal sensor configuration, i.e., the number and location and sensors leading to a good compromise between classification accuracy and inference time.

The quantitative outcome related to metrics and comparisons are reported in detail in the previous subsections. Such results show that the classification strategy effectively increased accuracy for all combinations; remarkably, the exploitation of IMUs both at the right wrist and the two pelvises (e.g., RW+RP+LP combination) led to the highest boost in accuracy. This

proves the efficacy of the proposed averaging strategy in enabling more accurate predictions of continuously performed human actions. Furthermore, even though employing *grouped windows* delayed the final prediction of the model targeting CHAR, the time needed to recognize one activity performed in a seamless way stayed beneath 500 milliseconds for all combinations. Hence, inference time on a single data sample is coherent with a real-time scenario of health monitoring impaired subjects, whose execution of ADLs lasts more than 2 s [155–157]. In light of this, one may infer that the exploitation of *grouped windows* effectively increases the classification performance without excessively enlarging inference time for all combinations, especially the RW+RP+LP combination that is revealed to be the optimal sensor configuration as a good trade-off between accuracy and computational cost; indeed, albeit the average time needed to inference on the test dataset becomes slightly higher, such increment is not significant and the average accuracy of the model using all sensors gains from 83.83% to 96.69% after combining predictions of sub-windows.

When comparing sensor combinations (see Subsubsections 1.3.3.2 and 1.3.3.3), it emerged that configuration with two sensors located at the right wrist and the left pelvis, i.e., RW+LP is the best among sensor pairs, arguably because it integrates information regarding the motion of both upper and lower limbs, respectively. On the contrary, placing IMUs either at the left pelvis and the sternum (LP+S) or at the two sides of the pelvis (RP+LP) slightly decreases classification performance. This results in misclassification between S2S and LD (Figure 1.21), which may be due to the absence of information about the movement of the right wrist that is recruited to support the lying-down action. Indeed, integrating wrist-related information into either LP+S or RP+LP combinations (i.e., RW+LP+S and RW+RP+LP, respectively) can reduce misclassifications and ensure a more accurate CHAR-targeting framework.

On the other hand, pairing the sensor at the right pelvis with the one at the right wrist (i.e., RW+RP combination) may lead the model to fail in recognizing turning, which is confused with walking, and sit-to-stand, which is misclassified as lying-down; the sensor configuration with IMUs at the two sides of human pelvises reduces misclassifications between TN and W, keeping them between S2S and LD. On the contrary, feeding the model with data coming from both pelvises and the right wrist (i.e., RW+RP+LP triple) enhances accuracy.

Such outcomes can be explained with the following motivation: the sensor at the left pelvis captures relevant information about the turning action, whereas the one at the right wrist is crucial in recognizing the lying-down motor pattern. Hence, either using this sensor pair (i.e., RW+LP) or integrating it with one (i.e., RW+RP+LP) or more sensors (i.e., RW+RP+LP+S) allows for classifying continuously executed ADLs with a satisfying

accuracy (close to 100%); however, the RW+RP+LP triple is the optimal configuration of sensors in the proposed workflow for CHAR, since it does not lead to an excessive increase in the inference time with respect to using two sensors.

1.3.5 Conclusions

This work presents a framework based on Deep Learning (DL) for classifying activities of daily living (ADLs) that are executed uninterruptedly by means of data coming from inertial sensors placed at different parts of the human body. Comparison of the computed metrics for different sensor configurations proved the efficacy of the proposed workflow in accurately recognizing motor actions with temporal performance that are acceptable in a real-time clinical scenario. Most notably, the outcomes indicate that the integration of sensors located at the right wrist and the two pelvises offered a good compromise between accuracy and computational cost.

The main limitation of the study is related to the size of the experimental sample. This could be addressed either by recruiting new subjects with different characteristics or by exploiting DL-based data augmentation algorithms, such as generative adversarial networks [160]. Besides, the investigation may be pushed forward by implementing explainable artificial intelligence methods (e.g., attention mechanism) to improve interpretability [4, 161–164].

In addition, the dataset of activities to be recognized can be enlarged so as to include other clinically relevant transitional motor actions (e.g., stand-to-walk, stand-to-sit, walk-to-sit, or lying-to-sit). In so doing the proposed framework could be even addressed for evaluations of either motor or cognitive impact, such as motion intent recognition [165–167]. Furthermore, acquiring inertial signals during stair ambulation would offer the possibility to investigate another motor pattern in which some patients would exhibit an abnormal execution of the task due to the fear of falling [118].

1.4 A Deep Learning-based framework oriented to pathological gait recognition with inertial sensors

Abnormal locomotor patterns may occur in case of either motor damages or neurological conditions, thus potentially jeopardizing the individual's safety. Pathological gait recognition (PGR) is a research field aimed to discriminate among different walking patterns. A PGR-oriented system may benefit from the simulation of gait disorders by healthy subjects, since

the acquisition of actual pathological gaits would require either a higher experimental time or a larger sample size.

This section presents a workflow based on convolutional neural networks to recognize normal and pathological locomotor behaviors by means of inertial data related to nineteen healthy subjects.

The remainder of this section is as follows. At first, Subsection 1.4.1 describes the scientific literature regarding pathological gait recognition. Secondly, materials (i.e., the system and protocol for data collection) and methods (i.e., preprocessing operations, CNN-based architectures, and statistical analysis) are discussed in Subsection 1.4.2. Then, the results are shown and discussed in Subsection 1.4.3. Ultimately, Subsection 1.4.4 draws conclusions about the conducted study and suggests ideas for future works.

1.4.1 Related Works

Human locomotion is a symmetric motor action [168] that requires the involvement of the central and peripheral nervous systems actuating mechanisms to control limb movements, posture, and muscle tone. When this neuromotor process is compromised by either the physiological decline due to aging or such pathological conditions as Parkinson's disease (PD), abnormal walking patterns may be exhibited [31]. Therefore, monitoring locomotor behaviors is needed to evaluate whether and how the individuals' motor state deviates from a healthy gait [10], and such difference may be an indicator of gait disorders [169, 170].

In the context of healthcare, the employment of systems for monitoring and recognizing gait allows to record the motor execution, identify a possible gait disorder, and provide feedback for the patients' assistance [32, 171–174]. In light of this, walking pattern recognition has even the potential to support clinicians for both rehabilitative and remote-monitoring purposes [175] aiming at the treatment of neuromotor pathologies, such as PD [176–180], cerebellar ataxia [181], stroke [182, 183], and cerebral palsy patients [184].

Gait recognition (GR) is a human activity recognition problem that is directed to differentiate locomotion from other motor actions [10], whilst pathological gait recognition (PGR) may be regarded as a subfield of GR that is used to discriminate motor patterns between healthy and pathological in case of binary classification [169] or among different gait disorders [31, 33, 171, 175, 185–187]. Though a binary classification is easier to accomplish due to the high deviation of pathological motor patterns with respect to normal gait [177, 179, 182], a PGR including different gait disorders allows to discriminate even similar walking patterns [170], such as those of foot drop and hemiplegia.

The recognition of pathological gaits needs a high amount of data related to patients to be accurate, which implies to make the experimental subjects execute multiple repetitions of several motor actions [10, 168]. However, this may be a high-demanding motor task in the case of actually impaired subjects due to their condition; for this reason, such individuals could perform the target motor pattern only a limited number of times or with longer breaks [173]. As a consequence, a dataset imbalance between healthy and pathological individuals would arise, thus introducing a bias in the classification; since this worsens the performance of automatic recognition, a higher amount of patients is needed to be involved [188]. Moreover, the specific disease severity influences the number of recruitable patients, which could be seriously restricted in case of non-autonomous locomotion, and a constant supervision of clinicians is still required for the patients' safety. Hence, the simulation of abnormal walking patterns by healthy individuals may provide a benefit to the performance of a PGR framework, considering their possibility to perform different trials of various walking actions. In so doing, the efficacy of a classification pipeline can be evaluated prior to any investigations on actual pathological individuals [31]; this is similar to the concept of cross-subject domain adaptation [189], meaning that the model is pre-trained on abnormal walking patterns simulated by healthy controls before being finally tested on actual pathological data. Besides, the PGR system could then carry out an early detection of abnormal walking patterns [170, 190].

A pathological motor pattern may be replicated in different ways, such as fixing lower limb joints [169] or making the subject wear a shoe unilaterally [172]; however, such methodology could result in the individual's discomfort during the execution, thus potentially leading to involuntary compensations that alter the simulation, and would require a complex setup to mimic various gait disorders. Therefore, experimental protocols addressing PGR are typically based on the simulation of such impaired motor behaviors without any physical constraint on the lower limbs [31, 32, 185].

Walking patterns for PGR can be recorded by means of such fixed sensors as optical motion capture systems [171], which provide experimenters with high-fidelity data on movement patterns during the gait cycle [191]. Among these devices, RGBD cameras have obtained comparable performance with respect to Vicon systems [171], which have a limited application due to their expensiveness [169]. RGBD cameras recognized activities of daily living (ADLs) with performance that are similar or even higher to inertial wearable devices [192]. However, these devices are influenced by illumination and occlusions and are characterized by a limited coverage area [193]; in addition, their need for an extensive preprocessing to prepare data for the actual classification pipeline [171] could be in contrast with real-time requirements of remote-monitoring applications [10]. Hence, such wearable

sensors as inertial measurement units (IMUs) could be preferred for their portability, which allows for their usage in both outdoor and indoor environments [10, 175].

Subsequently, motor behaviors can be recognized by Machine Learning (ML) models, which were trained on data related to either actual pathological individuals or locomotor disorders simulated by healthy subjects. For instance, Dolatabadi et al. [188] fed such ML models as a k-nearest neighbor (kNN) with the data coming from Kinect sensors to automatically discriminate walking patterns of healthy subjects and individuals affected by either stroke or acquired brain injury. Ghobadi [32] trained a support vector machine (SVM) with IMU data to recognize a simulated foot drop behavior.

Notwithstanding, these pipelines needed a complex and time-demanding feature engineering stage prior to the actual classification [10, 172]. On the other hand, Deep Learning (DL) architectures, such as convolutional neural networks (CNNs) [171, 173, 194], can be trained directly on raw data, thus avoiding manual feature extraction [10, 185]. For instance, Oh et al. [173] exploited a 1D-CNN to recognize the activities of daily living performed by hemiparetic stroke patients and healthy controls, who wore IMUs on the wrist, forearm, upper arm, trunk, and ankle. However, such ADLs did not entail locomotor patterns, since they were conceived for investigating the asymmetry of upper limb motions of stroke individuals.

1.4.2 Materials and Methods

The proposed framework for pathological gait recognition is reported in Figure 1.23. Herein, inertial data are first collected from five sensors placed on the human body during the execution of walking patterns, and then used to feed each of three different DL-based classifiers, which differ in terms of architecture.

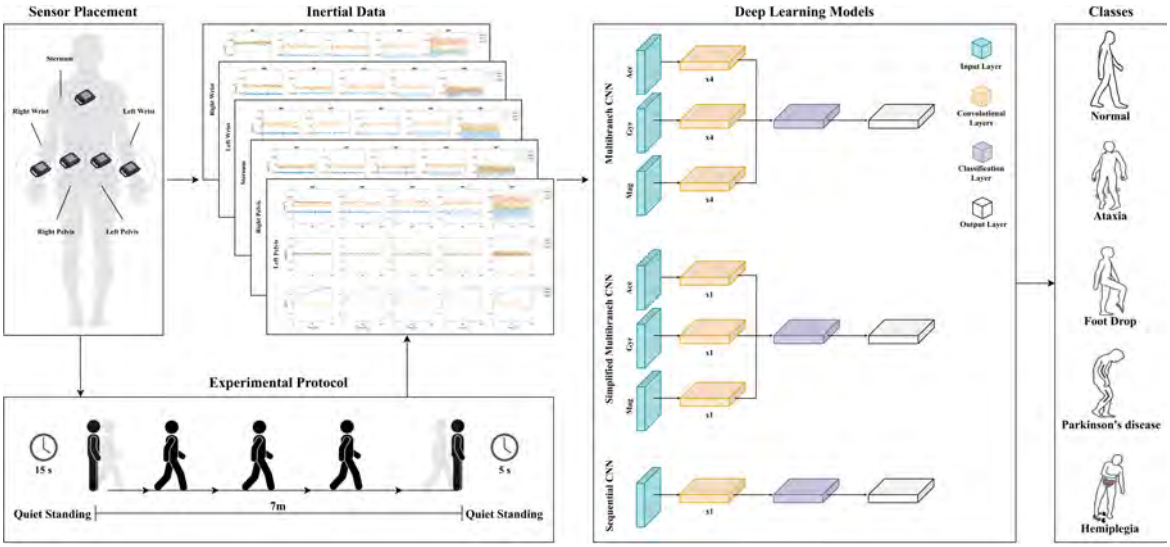

Fig. 1.23 The presented framework is based on the acquisition of inertial data by means of five IMU sensors, whose components are given as input to each of three DL-based models, which return the label associated with the walking pattern.

1.4.2.1 Data Collection

This sububsection reports the individuals recruited in the experiments, the walking behaviors to be simulated, the IMU sensors used to acquire kinematic data, and the experimental protocol to be followed.

Participants Nineteen healthy subjects are recruited among the physiatrists and physiotherapists of IRCCS Maugeri (Bari, Italy) to guarantee a plausible simulation of pathological gaits. A proper balancing among males and females has been guaranteed (i.e., 9 males and 10 females) to prevent the model from being biased by sex [194]. These participants have no motor or cognitive disorders, and differ in age (37.6 ± 13.0 years old), weight (72.9 ± 12.7 kg), height (170.7 ± 6.8 cm), and anthropometric characteristics for the sake of a higher data heterogeneity. Prior to the beginning of the experimental session, participants have been informed about the execution of the motor tasks.

Walking actions The activities to be performed have been chosen among the motor disorders that had been treated the most in the IRCCS Maugeri in Bari, Italy. In light of this, in addition to normal walking, four pathological gaits have been considered and they are ataxic, equine (foot drop), hemiplegic, and parkinsonian gaits [195]. The description of these walking patterns is provided in the following.

- *Normal gait* mainly requires alternating flexion-extension movements of the lower limb joints (i.e., hip, knee, and ankle), possibly supported by arm swinging to increase balance.

- *Hemiplegic gait* is the result of a poor control of the flexor muscles during the swing phase, as well as the spasticity of the extensor muscles involved in the extension of the paretic leg [31]. The knee does not flex normally during swinging, thus causing the leg circumduction [191]. On the paretic side, the hemiplegic patient is prone to raise the shoulder and to keep the arm close to the trunk, flexed, adducted, and with the wrist internally rotated.

- *Equine gait* (foot drop) can be induced by abnormal activity of the plantar muscles in the swing phase, thus resulting in the weakness in foot dorsiflexion and an abnormal ankle position for which knee flexion or hyperextension during the stance phase of locomotion are used as compensation [196].

- *Ataxic-cerebellar gait* is characterized by a wide base of support and a low cadence of steps that leads to an impaired balance and generates instability [31].

- *Parkinsonian gait* determines the presence of bradykinesia (delayed movement) with short and slow steps, as well as issues in detaching the forefoot [31, 197]. The Parkinsonian patient has even a forward flexed trunk because of muscle rigidity in this body part and tremor in the hands [4, 194].

IMU sensors Wearable IMU sensors (OPAL^{TM}, Portland, OR, USA) have been utilized to acquire data from each subject. These devices are automatically calibrated by the Motion Studio system by APDM and are worn by means of such elastic bands as Velcro straps to avoid direct contact with the skin and consequent motion artifacts due to friction. Five sensors have been selected (see Figure 1.23) and worn by each participant on both sides of the human pelvis (RP and LP), on the right and left wrists (RW and LW), and on the sternum (S). This distributed placement has been preferred with respect to the tendency by many PGR studies to promote the subject's comfort in daily life by exploiting the potentiality of e-textiles [198]: more specifically, the sensor on the sternum can be embedded into a smart T-shirt, those on the wrists can be part of on a smart bracelet, and those at the pelvises might be inserted in a smart belt. In addition, placing sensors on different body parts is useful to detect a wider myriad of motor actions that involve the upper and lower limbs, whether separately or simultaneously [10, 199].

The sensor configuration is almost the same as in a previous work about human activity recognition [10], with the only difference of an additional IMU on the left wrist. Furthermore, this placement enables the detection of pathological behaviors: in fact, the IMUs on the pelvises may carry the lower-limb movements compensating for either hemiplegia or foot drop; on the other hand, the sensor on the sternum allows for detecting Parkinsonian trunk flexion; sensors on the wrists are essential to record the presence/absence of arm movements corresponding to the dominant and/or pathological side (hemiplegia), or the presence of Parkinson tremor. This sensor placement can capture the characteristics of a normal gait too, as already mentioned in a previous work [10].

The experimental data are recorded with a sampling rate of 128 Hz from a 3-axis 14-bit accelerometer to measure linear acceleration, a 3-axis 16-bit gyroscope to acquire angular velocity, and a 3-axis 16-bit magnetometer for magnetic field intensity [200].

Experimental Protocol The protocol took place at the Laboratory of Movement Analysis of IRCCS Maugeri in Bari, Italy; it encompasses the execution of multiple repetitions of both normal locomotion and the simulation of pathological gaits, meaning that each subject is asked to perform four repetitions for each task. The mimicking quality is qualitatively ensured by a prior familiarization stage, whose duration was not excessively high since physiatrists and physiotherapists executed the tasks. Besides, the verisimilitude is further allowed by an expert in the realm of neurorehabilitation, who gave instructions in a video that is taken as a further reference together with the Standford Medicine guidelines [201]. A total of 28 repetitions have been recorded for each subject, since hemiplegic and equine gaits have been mimicked at each side of the human body to increase the model generalizability in recognizing the pathology. In fact, in these cases the asymmetry of motor patterns can be relevant not only for activity classification, but also for an effective rehabilitation [173].

Each repetition begins with a standing phase of 15 s, proceeds with an overground walking on a linear traced path of 7 m, and ends with another standing stage of 5 s, as shown in Figure 1.23. Note that this path has been followed in different directions for the sake of a higher data variability. Each subject is told to wait a reasonable time between contiguous repetitions [10]. In view of this, the protocol required a total of almost 45 min for each individual.

1.4.2.2 Classification Pipeline

The pipeline for classifying walking patterns is made up of two parts, which are a preliminary set of preprocessing operations and the implementation of different models for PGR.

Preprocessing Data from the inertial sensors are initially acquired for each subject and repetition as a matrix of size $N_s \times (5 \cdot 9)$, where N_s is the number of samples in a single repetition, 5 is the total number of IMU sensors, and 9 is the total number of IMU components (3 for the accelerometer, 3 for the gyroscope, and 3 for the magnetometer). Afterwards, they have been processed first with a segmentation by visual inspection to exclude both the static period (initial and final standing phases) and the transitional movements (stand-to-walk, walking, and walk-to-stand), isolating the walking patterns of interest.

Accelerometer, gyroscope, and magnetometer values have been then normalized for each walking pattern in the range $[-1,1]$ to obtain a uniform representation of the data [10]. Subsequently, a windowing procedure has been applied to enlarge the dataset dimensionality by dividing the signal into windows of 128 samples (1 s) with 50% overlap (0.5 s); this window width is chosen so as to capture enough motor patterns without excessively increasing the computational cost [202].

IMU data have been resampled both to achieve a uniform sample size and to exploit the whole informative content of the signal [10]. Additionally, different combinations of sensors have been examined to verify the influence of sensor configurations on the classification performance [10].

Classification models In this work, the pipeline for classifying normal and abnormal walking patterns includes three DL-based models:

1. mCNN-1D: a multi-branch one-dimensional convolutional neural network that was already exploited for continuous HAR in a previous work [10];
2. smCNN-1D: a simplified multi-branch one-dimensional convolutional neural network;
3. sCNN-1D: a sequential one-dimensional convolutional neural network.

CNN-based architectures have been chosen in view of their successful application in related works about PGR [33, 186, 187], together with their efficacy in HAR [10, 203].

The mCNN-1D model (Figure 1.24a) is characterized by the same architecture and hyper parameters as the one used in the previous work [10], with the only difference that the early-stop criterion herein monitors the recall on the validation set to avoid overfitting.

The smCNN-1D model (Figure 1.24b) differs from mCNN-1D model from the architectural point of view, since it adopts only one 1D convolutional layer, which uses 128 filters with a kernel size of 5, and one fully connected layer with 128 neurons; moreover, the hyper parameters are the same, except for the batch size that is 256.

The sCNN-1D architecture (Figure 1.24c) is inspired by that of the smCNN-1D model. Since it is a sequential CNN, it is not made up of parallel branches, but only of a unique set of layers. Therefore, input data are not split into the different IMU channels (i.e., accelerometer, gyroscope, and magnetometer); on the other hand, such IMU components can be given as input to the model either combined or separately.

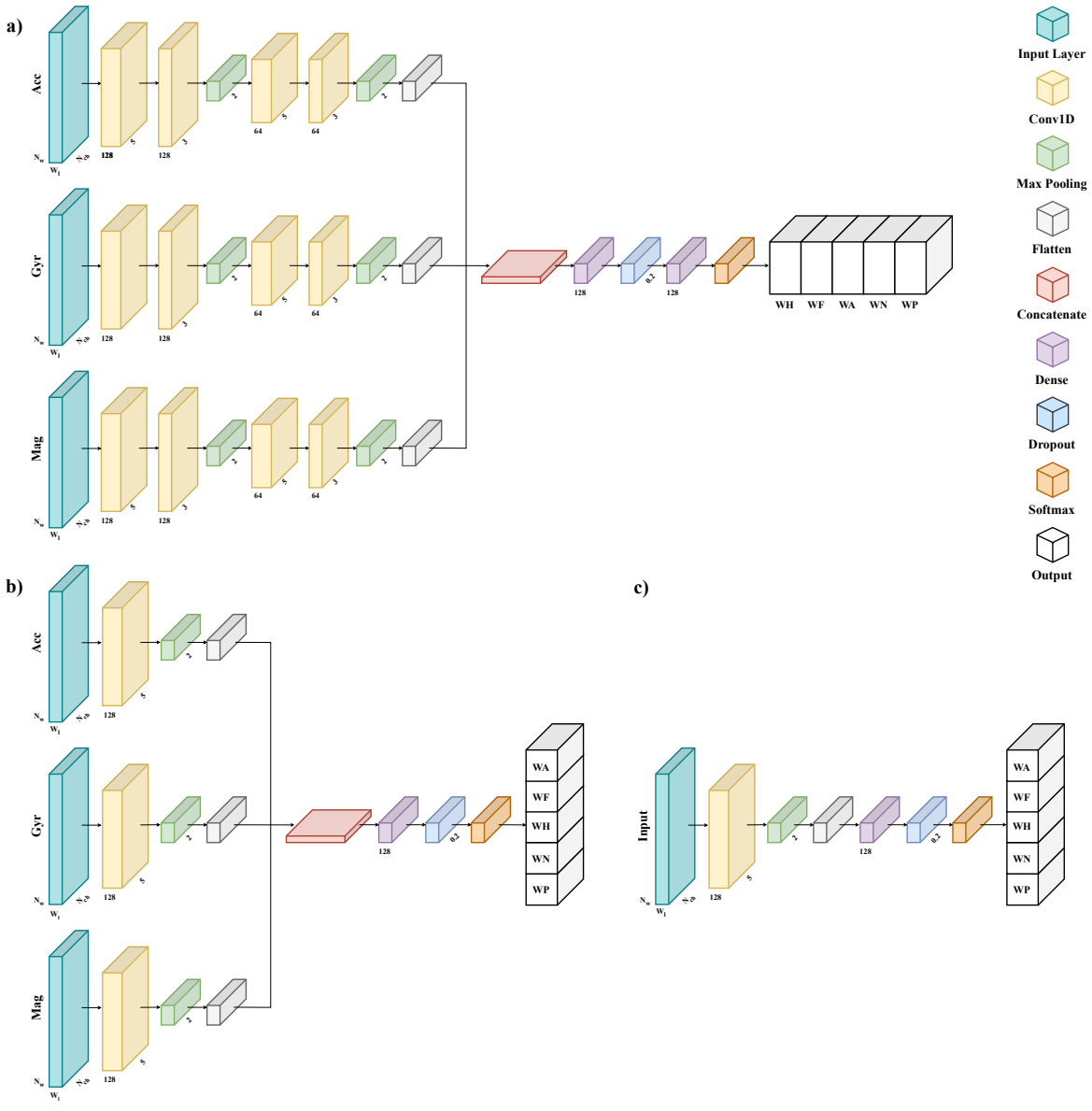

Fig. 1.24 The classification models addressing PGR: a) a multi-branch one-dimensional convolutional neural network; b) a simplified multi-branch one-dimensional convolutional neural network; c) a sequential one-dimensional convolutional neural network. Note that N_w is the number of windows in the input dataset, which differs with both subjects and trials; W_l is the window length, which is fixed; and N_{ch} is the number of sensor channels.

For all architectures, to aggregate the data from multiple sensors into one single input, the input layer is fed by a multidimensional array whose shape is (N_w, W_l, N_{ch}), where: N_w is the number of windows in the input dataset, which may change across subjects and trials; W_l is the window length, which is fixed; and N_{ch} is the number of sensor channels, which is equal to the quantity $N_c \cdot N_s$, given N_s the number of sensors in the combination to be evaluated and N_c the number of IMU components to be examined. Note that N_c can be one for the sCNN-1D when only a single IMU component is used as input to the model, otherwise it is three.

The classification has been designed to recognize five walking patterns, since both hemiplegic and equine walks have not been distinguished based on the affected side.

The data splitting method is the same across all models: the dataset is randomly split across subjects [204, 205] such that the data of the 60% of them (11 subjects) are assigned to the training set, the data of the 20% of them (4 different subjects) to the validation set, and the data of the 20% (further different 4 subjects) to the testing set. This splitting strategy has already been employed in other studies that are oriented to fall detection [206] and human activity recognition [207], as well as conceived for diagnostic purposes in either the medical field [208, 209] or the energetic context [210]. To ensure a fair and unbiased evaluation of each model, the above-mentioned partition is applied ten times the dataset is split ten times, each of which different subjects are randomly extracted to constitute the three sets [10, 211].

All investigations of the models have been conducted on the Google Colab-Pro framework such that each model is trained on a Tesla T4. All the architectures have been trained and inferences by means of Tensorflow, Sklearn, Pandas, and Numpy libraries.

1.4.2.3 Metrics and Statistics

Different metrics have been used to evaluate the model performance for each sensor combination reported in Figure 1.25. At first, the test dataset has been evaluated in terms of accuracy and recall, whose formulas are reported as follows.

$$\text{Accuracy} = \frac{TP+TN}{TP+TN+FP+FN} \tag{1.3}$$

$$\text{Recall} = \frac{TP}{TP+FN} \tag{1.4}$$

where TP, TN, FP, and FN represent true positives, true negatives, false positives, and false negatives, respectively.

On the other hand, the feasibility of the framework in real-time clinical application has been investigated by computing the inference time, which is the instant when the data is given as input to the model the one in which the result classification label is obtained [212].

The normality distribution of these indexes has been checked by means of Shapiro-Wilk test with a significance level of $p = 0.05$. Consequently, for pair-wise comparisons, their values have been statistically compared through a non-parametric Wilcoxon signed-rank test for non-normally distributed sets and with a paired t-test ($p < 0.05$) for normally distributed ones.

These analyses have been conducted using Matlab 2022b platform.

1 sensor	2 sensors	3 sensors	4 sensors	5 sensors
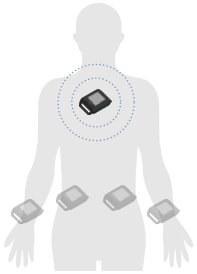	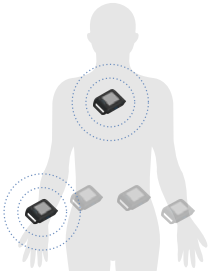	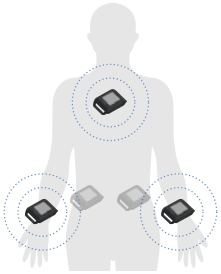	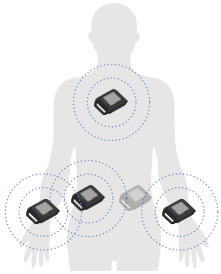	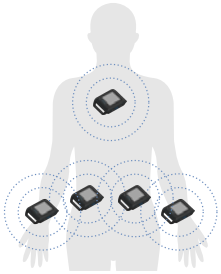
S LP RP LW RW	S + LP S + RP S + LW S + RW LP + RP LP + LW LP + RW RP + LW RP + RW LW + RW	S + LP + RP S + LP + LW S + LP + RW S + RP + LW S + RP + RW S + LW + RW LP + RP + LW LP + RP + RW LP + LW + RW RP + LW + RW	S + LP + RP + LW S + LP + RP + RW S + LP + LW + RW S + RP + LW + RW LP + RP + LW + RW	S + LP + RP + LW + RW

Fig. 1.25 Sensor combinations grouped by the number of sensors, which can be placed at the sternum (S), the left pelvis (LP), the right pelvis (RP), the left wrist (LW), or the right wrist (RW).

1.4.3 Results and Discussion

This work presents a framework based on deep learning aiming at performing pathological gait recognition (PGR) - i.e., recognizing healthy and simulated pathological gaits. For this purpose, various architectures based on convolutional neural networks (CNNs) have been implemented, and they are a multi-branch one-dimensional CNN (mCNN-1D), a simplified multi-branch one-dimensional CNN (smCNN-1D), and a sequential one-dimensional CNN (sCNN-1D). Such models have been trained and tested with the data coming from inertial measurement units (IMUs) placed at five body parts, which are the left pelvis (LP), the right pelvis (RP), the left wrist (LW), the right wrist (RW), and the sternum (S). The experimental

protocol followed by the subjects entails both the execution of normal gait (WN) and the simulation of four abnormal walking patterns, which are hemiplegic (WH), equine (WF), ataxic (WA), and Parkinsonian (WP) gaits. Three indexes have been employed to evaluate the performance of the proposed workflow: accuracy and recall are aimed to ascertain the capability to perform PGR, whilst inference time serves to assess its feasibility in a real-time clinical scenario. Note that the classification speed is needed to ensure a prompt assistance to any patients; for instance, when they are assisted by a robotic device, the supporting torque provided by the controller should be properly tailored to their disorder [213–219], which is the one recognized by the classifier. Furthermore, since the self-detection of gait patterns may be difficult, a real-time classification allows for correcting abnormal behaviors [197] or adapting to the patient's improvements [199] that would occur during a rehabilitation program. The model is tested for different sensor combinations to establish the optimal configuration in light of the given metrics.

The radar plots reported in Figure 1.26 compares the results of the mCNN-1D and smCNN-1D architectures, each of which is fed with all the three components of the IMU sensors (accelerometer, gyroscope, and magnetometer).

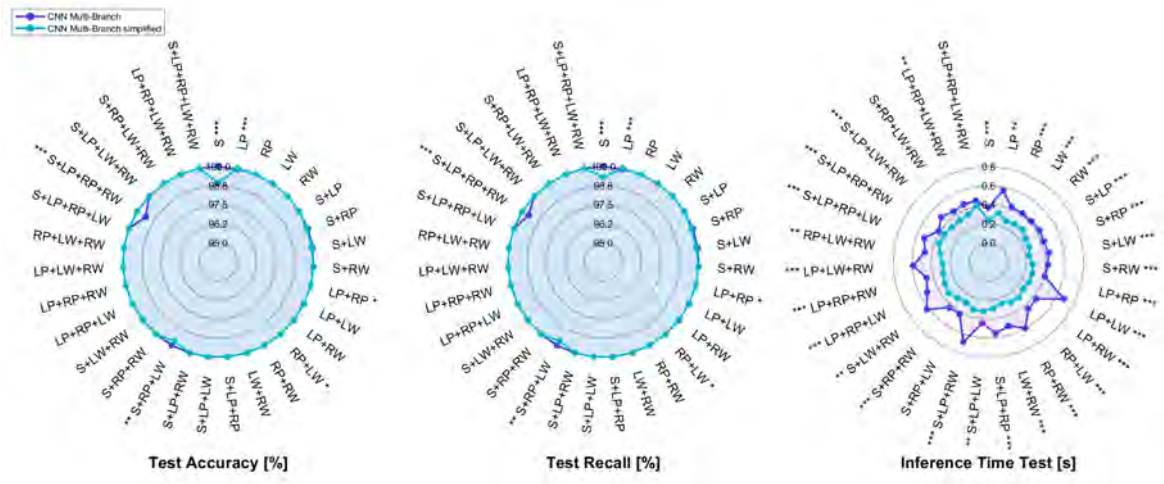

Fig. 1.26 Radar plot comparing metrics computed on the test set for the multi-branch CNN and its simplified version, with ** and *** representing statistically significant comparisons with $p < 0.01$ and $p < 0.001$, respectively.

The median of accuracy and recall for the two models is 100% in almost all sensor configurations, despite the dataset imbalance. This could be due to the fact that applying segmentation before normalization allows for excluding all the possible motion artifacts that would worsen the classification performance. However, as for the mCNN-1D model, such satisfying results in terms of accuracy are not accompanied by an equally acceptable

inference time, since its value approaches 600 $\pm$ 100 ms for some combinations, which can be excessive for a real-time application, since it is close to the 30% of the execution time of overground walking by impaired subjects [220].

Consequently, the model architecture has been simplified, thus reaching with the smCNN-1D model a test inference time that is significantly lower than the one of the mCNN-1D model in almost all combinations; besides, the maximum time decreases from approximately 700 ms to about 400 ms for the LP+LW and S+LP+RW sensor pairs. This computational time is even lower than 300 ms for some combinations with either a single IMU or sensor pairs for the simplified multi-branch CNN.

In light of this, the simplified architecture has been adopted for the sequential CNN (Figure 1.24c) as well. The performance achieved with the smCNN-1D and sCNN-1D models, whose input data are the three channels of the IMU sensors, are pictorially depicted in Figure 1.27.

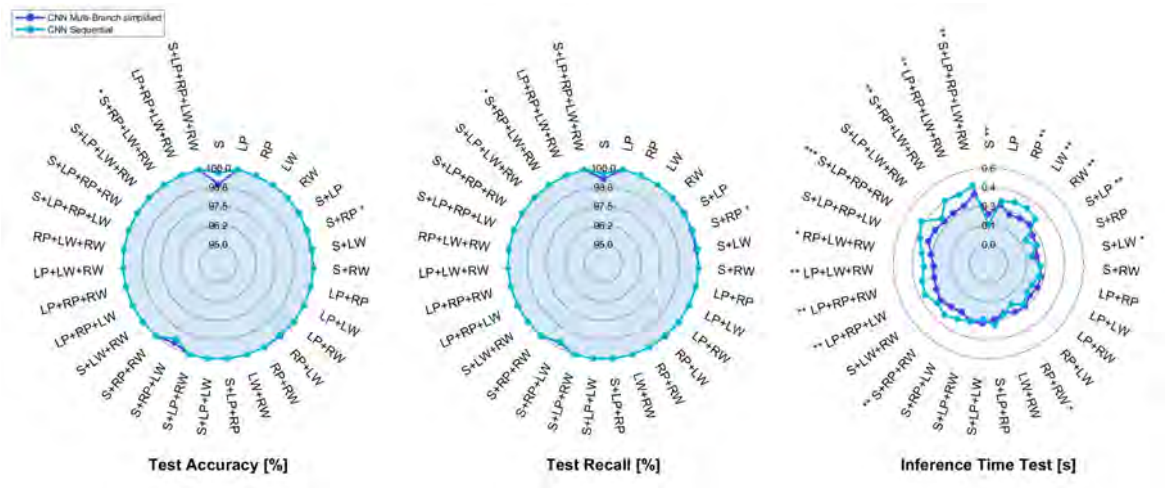

Fig. 1.27 Radar plot comparing metrics computed on the test set for the simplified multi-branch and the sequential CNNs, with *, **, and *** representing statistically significant comparisons with $p < 0.01$, $p < 0.05$, and $p < 0.001$, respectively.

To parity of accuracy and recall, the inference time does not seem to improve when passing from the smCNN-1D to the sCNN-1D model, except for the sensor on the sternum, in which case the test inference time is about 100 ms. This is presumably due to the use of unnecessary input data; therefore, the sCNN-1D model has been tested for all sensor combinations by separately giving as input each IMU component to the model, with the aim of evaluating which channel (i.e., accelerometer, gyroscope, and magnetometer) leads to the best model performance. The consequent results in terms of accuracy, recall, and inference time are pictorially shown with the radar plots reported in Figure 1.28.

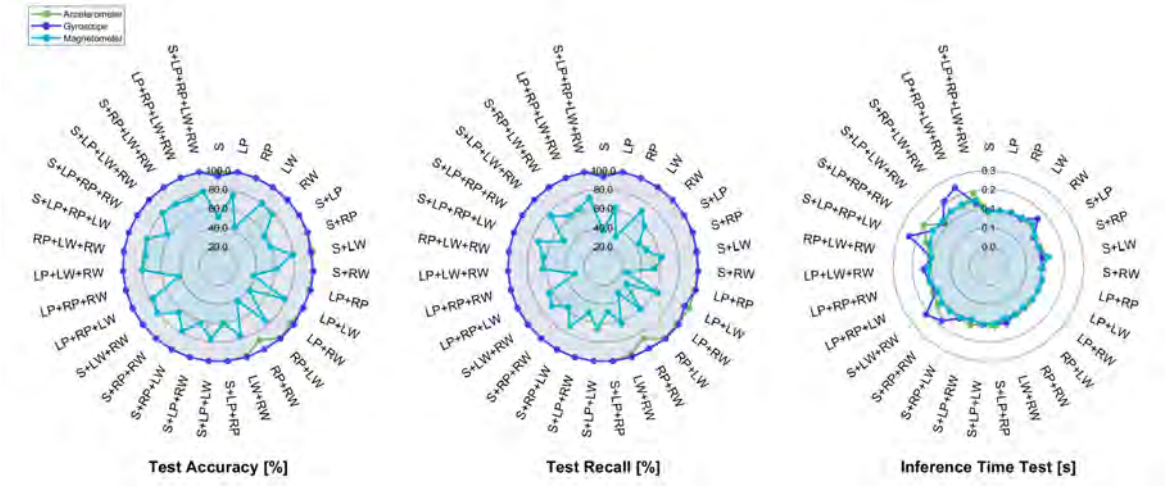

Fig. 1.28 Radar plot of the accuracy, recall, and inference time computed on the test set by feeding the sequential CNN with each IMU component separately.

The outcomes show better performance in both accuracy and recall for the accelerometer and gyroscope, whereas the outcome worsens when passing the magnetometer entry as input to the model, since the recall is about 80% only in three combinations (i.e., S+LW+RW, S+LP+LW+RW, S+RP+LW+RW). Moreover, the lowest values of accuracy are achieved for the combinations with one sensor placed at either the sternum or the right pelvis; instead, the accuracy for the LW+RW pair is higher than the one related to the LP+RP pair. Hence, it can be argued that the information carried by the magnetometer placed on the wrist raises the performance with respect to the magnetometers of the IMU located at the sternum and pelvis, which are not equally discriminative. In fact, the motor behavior of human wrists is different for each type of walking action: it is stationary on the affected side in the hemiplegic close to the sternum, it follows hand tremor in the Parkinsonian gait and arm sway in normal walking.

The outcome of the above-mentioned model in terms of inference time lies in the range $[100, 200]$ ms for almost all the three components, except for some combinations in which it slightly exceeds 200 ms in the case of the accelerometer and gyroscope. This outcome is more compliant to real-time requirements, since it at most equals the 10% of the execution time of a pathological walking [220]. Therefore, the sequential CNN model using either the accelerometer or the gyroscope seems to provide the best compromise among all the above-mentioned metrics.

Figure 1.29 and Table 1.3 report the average accuracy in distinguishing normal and simulated pathological gaits to compare the proposed framework with similar studies in the literature: all walking patterns have been classified with an average accuracy of 100%, thus outperforming related works.

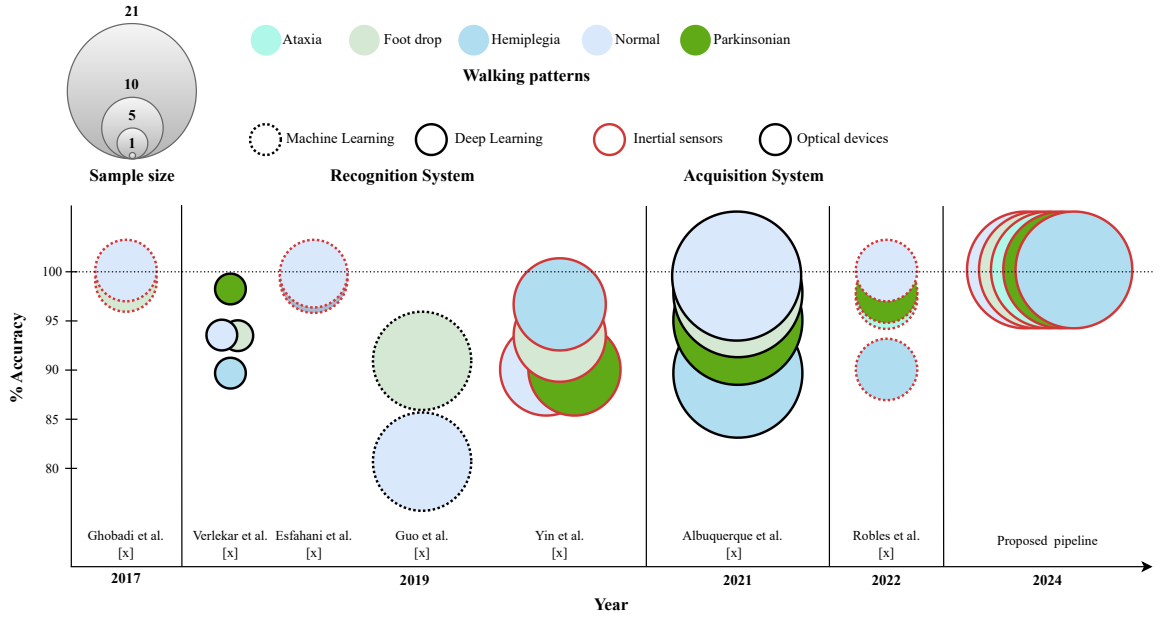

Fig. 1.29 Related works simulating abnormal walking patterns.

Table 1.3 Relevant features from related works, reported for comparisons among workflows.

	Ghobadi et al. [32]	**Verlekar et al.** [186]	**Eshefani et al.** [175]	**Guo et al.** [171]	**Yin et al.** [33]	**Albuquerque et al.** [187]	**Robles et al.** [31]	**Proposed framework**
Subjects	10	5	11	16	15	21	10	19
Input Data	IMU signals	Data from images	Data from smart textiles	Data from images	IMU signals	Data from images	Data from accelerometer	IMU signals
Classifier type	ML	DL	ML	ML DL	DL	DL	ML	DL
Classifier	SVM	CNN	kNN, LDA, SVM, ANN	SVM BiLSTM	ANN, LSTM, CNN	CNN	ANN	CNN
Normal	99.6%	94.0%	99.6%	81.24%	89.0%	99.0%	99.8%	100%
Hemiplegia	ND	87%	99.4%	ND	91.3%	89.0%	90.3%	100%
Ataxia	ND	ND	ND	ND	ND	ND	97.0%	100%
Foot drop	98.7%	94.0%	ND	92.9%	ND	97.0%	ND	100%
Parkinsonian	ND	98.0%	ND	ND	78.6%	95.0%	98.1%	100%

For instance, Robles et al. [31] utilized Artificial Neural Networks (ANNs) to classify simulated gait disorders (those of Parkinsonian, ataxic, and hemiplegic subjects) by analyzing accelerations of the center of mass of ten healthy subjects. An average accuracy of 99.8%, 90.3%, 97.3%, and 98.1% was obtained for the classification of normal, hemiplegic, ataxic, and Parkinsonian gaits, respectively. Ghobadi et al. [32] discriminated normal gait from

abnormal foot drop (FD) patterns, which were mimicked by ten healthy subjects, with an average accuracy of 99.6% and 98.7% (respectively) by training a SVM with Mahalanobis distance-based features extracted from the IMU signals of the subject's right leg. Esfahani et al. [175] employed various ML-based algorithms (e.g., ANNs, SVM, and kNN), which were fed with the data of eleven healthy subjects coming from a smart textile system, thus being able to differentiate between normal and hemiplegic gaits with an average accuracy of 99.6% and 99.4%, respectively.

However, such studies performed the actual classification after a time-consuming feature engineering procedure. On the other hand, other related works relied upon DL architectures to automatically extract features instead of handcrafting them [11]. For example, Guo et al. [171] exploited not only SVM, but also Bidirectional Long-Short Term Memory (BiLSTM) networks to classify normal and mimicked foot-drop walking patterns based on the images acquired with a single RGB-D camera; in so doing, averages accuracies of 81.24% and 92.9% were respectively achieved for the normal and the pathological gaits, which were simulated by sixteen healthy subjects. Albuquerque et al. [187] recruited twenty-one healthy subjects and developed a remote pathological gait classification system for discriminating normal, hemiplegic, foot-drop, and Parkinsonian gaits, thus achieving average accuracies of 99%, 89%, 97%, and 95%, respectively. The performance of these two works are almost comparable with the presented study except for the recognition of one class (i.e., normal and hemiplegic gait, respectively) which is mainly confused with similar walking patterns that are not entailed the focus of this work though. Verlekar et al. [186] trained CNN-based models with gait energy images, which were determined from a dataset of five healthy subjects; in so doing, it was possible to distinguish normal from hemiplegic, foot-drop, and Parkinsonian gait sequences with an average accuracy of 94%, 87%, 94%, and 98%, respectively.

Moreover, these latter studies addressed PGR with data coming from optical trackers, which may be limited in real-world scenarios. Only one work has been found to employ IMU data to recognize simulated pathological gaits by means of DL architectures. Yin et al. [33] utilized two accelerometers mounted on the lower limbs to classify normal and simulated pathological gaits through both ML (i.e., ANN) and DL models (LSTM and CNN); in so doing, normal, hemiplegic, and Parkinsonian motor patterns were discriminated with average accuracies of 89%, 91.3%, and 78.6%, respectively. Despite the promising performance, they are yet lessened by the proposed workflow, arguably due to the order of preprocessing operations (i.e., normalizing signals before segmenting) that may introduce motion artifacts worsening classification performance; in addition, that investigation was conducted on a

lower sample size (i.e., number of participants) with the same sensor type (i.e., inertial measurement units) and did not consider the same walking patterns as in this work.

1.4.4 Conclusions

This work presents a Deep Learning-based framework aimed at the classification of normal and abnormal walking patterns by means of multiple convolutional neural networks, which are fed with the data coming from inertial sensors worn at different locations of the human body.

Given the promising performance of the exploited models in terms of accuracy and inference time, the proposed workflow is claimed to be effective in discriminating motor patterns. The instructions of an expert clinician for a realistic gait disorder simulation contributed to the quality of classification results. However, the framework has been tested only on data related to locomotor actions, both normal and abnormal, performed by healthy subjects, since this work has been conceived as a feasibility study before the application on actual pathological gaits. Therefore, the proposed workflow should be evaluated by exploiting data coming from people actually affected by gait disorders to test its usefulness in a clinical scenario. In so doing, even the severity rating of such neuromotor disorders as Parkinson's disease [176–180] and ataxia [181] can be explored. Furthermore, since the motor actions have been performed by people with advanced clinical knowledge, a successive experimental campaign could include subjects with no expertise in gait disorders for the sake of an even higher data variability [221].

Secondly, only five walking patterns have been considered, since the samples of the hemiplegic and equine gaits have not been distinguished according to the emulated affected side; hence, a 7-class classification may be pursued to investigate whether the framework effectively performs PGR even in case of unilateral gait disorders, which may be useful for the corresponding rehabilitation [173].

The type of abnormal walking patterns considered in this work, though being in line with most of related works, is restricted to evident motor behaviors. Therefore, for the sake of an even higher usefulness in a clinical scenario, such less obvious motor patterns as walking tremor [222] should be considered in the future. Another example is given by the Parkinsonian tremor, which could be further addressed in view of its previous successful simulation by healthy subjects with slight amplitude differences with respect to actual pathological subjects [223]. This may be done by conceiving some indexes to measure the deviation of an

individual's gait pattern from the range typical of a healthy subject, thus tracking the patients' rehabilitative progress and the effectiveness of therapies [12, 191, 194, 224].

Future research could also aim to develop an integrated explainable framework that combines the strengths of attention mechanisms [4, 204, 225] and Layer-wise Relevance Propagation [226]. These methods helps in understanding which parts of the input data (i.e., IMU component) contribute the most to the model predictions.

With this in mind, the proposed gait recognition system can be enhanced to pursue its seamless integration into either the clinical realm or a home application [199]. This may be achieved by embedding the inertial sensors within e-textiles to increase the subject's comfort either in a rehabilitative path or in a remote-monitoring application.

Chapter 2

Applications for occupational purposes

2.1 Introduction

High productivity requirements demanded by industrial and manufacturing scenarios force human operators to daily perform repetitive and exhausting actions with awkward body postures exposing them to injuries. This process, if excessively prolonged over time, may lead to medical conditions known as work-related musculoskeletal disorders (WMSDs). WMSDs are the first cause of occupational diseases in industrialized countries: they account for 15% of total healthcare costs in the EU-28, affecting 60% workers and concurring in billions of dollars of lost production for the industry sector [227]. Since WMSDs mostly concern neck, shoulders, and back [228], the demand for direct upper body assistance in the workplace has been increasing in the past years.

A major asset for the prevention of WMSDs in such complex environments is occupational exoskeletons (OEs) designed for upper limbs. By means of actuation systems, these exoskeletons are able to provide torque to the user's arms, thus sustaining the upper limbs and relieving the local musculature during arm elevation and weight lifting movements [229]. Industrial and logistic companies have increasingly shown interest in deploying OEs inside the workplace [230], with long-term expectations of reducing the occurrence of WMSDs and hence improving the related productivity of the human workforce by decreasing absence rate [231]. Moreover, the use of OEs has been demonstrated to reduce the required energy expenditure for completing a series of tasks, concurring in an overall redistribution of the latter among a reduced number of workers and thus resulting in a general decrease in costs [232].

Subjective evaluations derived from questionnaires are widely employed within the validation of OEs as a measure of the perceived exertion [233–236]; however, even such

self-ratings can be biased by the user's psychology, which may be influenced by the personal experience with robotic interfaces on its part [237]. Therefore, new methods of human performance evaluation should be integrated into the conventional ones in order to achieve unbiased instruments.

2.1.1 Objective and Research Question

Innovative interfaces integrating OEs have allowed for the design of objective evaluations for industrial purposes [218, 233–235].

Despite the advances of these systems, some research questions still remain to be addressed.

A gap regards the validation of active OEs by means of realistic static and dynamic tasks [238]. In the same context, the impact of a robotic interface on muscle connectivity has not been clarified yet [239].

Based on the prior discussion concerning opportunities and difficulties of interfaces for motor assessment, the main objective of the research conducted for this thesis has regarded the conceptualization, development, and implementation of frameworks to advance the state-of-the-art in this field. The workflows have been developed with the aim of pursuing their feasibility and usability in industrial scenarios.

The applications considered mainly belong to the realm of robot-aided power augmentation. Tasks under consideration concerned performance evaluation. Data under consideration were collected in laboratory.

2.1.2 Contribution

In the aforementioned scenario, the main purpose of this thesis is to develop new frameworks based on exoskeletons to quantify motor performance [238, 239].

In the context of active occupational exoskeletons, the majority of portable upper-limb exoskeletons for workers has found to undergo an in-lab assessment that is mainly based on static tasks either over the head [234, 240, 241] or under the head [242]. There are some minor exceptions featuring the dynamic lifting [243, 244] and carrying of loads of various weights [245, 246]; nonetheless, passive devices are mostly employed in these cases. Therefore, the work presented in Section 2.2 filled a research gap regarding both the design of active OEs to support humans in lifting weights and their in-lab assessment through static and dynamic tasks resembling daily activities in an industrial scenario [238]. Moreover, most of works employ traditional electromyographic metrics to validate OEs, whereas there exist

almost no previous works analyzing functional connectivity between muscles to investigate the impact of robotic devices for supporting the execution of human motor tasks. For instance, Cancrini et al. exploited a planar robot for challenging motor control of healthy subjects during several sessions of upper-limb training [247]. The same team studied the differences between healthy and stroke subjects in the execution of reaching tasks [248]. Nevertheless, both studies limited the analysis to the extraction of muscle synergies rather than determining the inter-muscular coordination. All the remaining related works employing muscle networks have not included robotic devices. Hence, the work presented in Section 2.3 contributes to the state-of-art by means of a muscle network analysis of healthy subjects during the execution of isometric tasks with and without an occupational exoskeleton. This has been revealed to be the first study investigating the influence of an upper-limb exoskeleton on human motion features by means of muscle network [239].

Ultimately, the technical contributions can be summarized as follows: an occupational exoskeleton has been validated by means of metrics derived from both conventional EMG measures and intermuscular couplings based on network theory.

2.1.3 Chapter Outline

This chapter is organized into the following sections. This chapter introduces the objective and the technical contribution of of the occupational-oriented applications of this thesis.

Sections 2.2 and 2.3 contain the related works and the contributions in terms of validation of occupational exoskeletons conceived for supporting humans in static and dynamic tasks.

2.2 Flexos: a Bilateral, Active and Portable Shoulder Exoskeleton Reduces Muscular Effort in Real World Weight Lifting Task

Work-related musculoskeletal disorders affect a high percentage of operators performing repeated weight lifting and moving in industrial scenarios. Since upper limb muscles are affected in the process, upper body assistance is increasingly needed to prevent WMDs and their consequent cost to the health system. Occupational exoskeletons (OEs) can be employed in industries with the final aim of decreasing energy expenditure and reducing WMD occurrence.

This section presents Flexos, a portable bilateral shoulder exoskeleton designed to assist logistic and industrial operators in performing weight-lifting tasks to prevent the insurgence of WMDs. The device has been designed to be worn as a backpack and with ergonomic-shaped 3D-printed interfaces to maximize the wearer's comfort. It provides only one series elastic actuated joint for each shoulder for both compensating the arms' weight - together with additional lifted weight - and taking into account the user's intentions. An in-lab assessment, designed to be close to real-life workplace use cases, was conducted on nine healthy right-handed subjects to evaluate Flexos capability in assisting the user during the execution of isometric, dynamic, and carrying-load tasks. Different metrics were extracted from time-series signals to assess the effort related to five targeted muscles surrounding the shoulder complex.

The outline of this section is organized as follows: Subsection 2.2.1 contains the state-of-art of occupational exoskeletons assisting humans in industrial-like motor tasks; Subsection 2.2.2 describes the mechanical design and the control system of the proposed device; Subsection 2.2.3 explains the experiments conducted for evaluating Flexos assistive efficacy; the outcomes of the data analysis carried out for this latter validation are provided in Subsection 2.2.4 and discussed in Subsection 2.2.5, wherein liimtations and future works are explored in Subsubsections 2.2.5.3 and 2.2.5.4 as well.

2.2.1 Related Works

Depending on their design, OEs for the upper body parts can be rigid [249] or soft [250, 251]. A rigid device is characterized by the presence of a kinematic chain made of rigid links and linear/rotary joints, which act in parallel to the human upper limbs. These devices often struggle with joint misalignments, arising at the interfaces between human and robotic joints. These issues become challenging particularly when dealing with the shoulder complex, consisting of a total of 5 Degrees Of Freedom (DOF). On the opposite side, a soft exoskeleton only consists of wearable garments equipped with soft actuation systems, such as cable tendons or pneumatic muscles. These devices tend to be lightweight and capable of preventing discomforts caused by joint misalignments since they do not feature a kinematic chain [252]. However, employing soft garments, which are characterized by specific structural performances, prevents these devices from providing more than a limited amount of torque [253]. So far, this issue has strongly limited the use of soft exoskeletons in industrial scenarios [254].

Fig. 2.1 The proposed Flexos exoskeleton for the shoulder.

Another crucial factor involves the exoskeleton actuation system, where predominant solutions to date mainly rely on passive energy storage systems, such as springs [255–258]. Despite being extremely light and simple, these devices do not provide real-time adjustable torque, as their estimates only depend on the arm elevation angle and fixed design parameters, such as the selected spring stiffness. On the contrary, active solutions can provide any desired amount of torque at any time, since they are usually based on electric motors whose limitations are only related to their structural configuration and absorbed power [233]. A great design candidate for active systems is Series Elastic Actuators (SEAs), which offer an estimation of the interaction torque by measuring the angular displacement of the series elastic joint. This facilitates the retrieving of feedback torque data, enabling real-time closed-loop torque control and thereby ensuring safety in physical Human-Robot Interaction (pHRI) [259].

Additionally, active systems facilitate the integration of assistance strategies driven by intelligent algorithms that draw insights from data of various types, such as signals related to

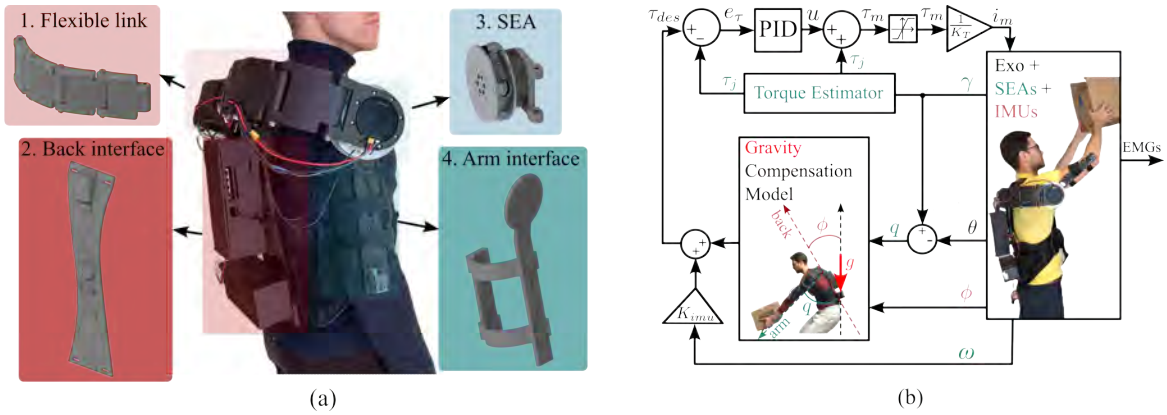

(a) (b)

Fig. 2.2 (a) Flexos design overview. (b) Schematic diagram of the implemented torque controller.

inertial measurement units (IMUs) or muscular activities measured with electromyography (EMG) sensors [260, 261]. However, these systems are frequently more complex and bulkier if compared to their passive counterparts [262]. For this reason, minimizing the number of active joints could provide a good compromise between the higher controllability of active exoskeletons and the device's ergonomics.

2.2.2 System Description

2.2.2.1 Mechanical design

Flexos main subsystems are shown in Fig. 2.2 (a). The device is mainly made up of rigid custom parts, most of which are produced using 3D printing technology, with additional soft interfaces that are hand-sewn to the rigid surfaces, thus the whole system is still considered a prototype.

The device interfaces with the human body through both a primary rigid part located at the back - Fig. 2.2 (a), 2 - and one arm interface - Fig. 2.2 (a), 4 - for each side. These arm interfaces can be secured around the upper limbs using two Velcro strap bands. Flexos also utilizes a kinematic chain - Fig. 2.2 (a), 1 - that operates in parallel to each human arm, linking the two primary human-robot interfaces (back and arm) together. This flexible link [263] enables the user to maneuver the arm around the internal/external rotation axis and shift the shoulder center of rotation around the acromioclavicular joint. It has one extremity fixed to the back interface, whilst the other one is connected to the SEA - Fig. 2.2 (a), 3 -. Each SEA features an actuator in series with an elastic joint: the actuator is comprised of a brushless DC motor, specifically the T-Motor AK80-9, capable of delivering a rated

torque of up to 9 Nm and featuring an integrated driver circuit that enables operations via the controller area network (CAN) protocol; the series elastic joint axis is perpendicular to all of the flexible link's joints axis because it lies on a horizontal plane while being incident to the shoulder center of rotation. The SEA internal rotation is mapped to the user's arm rotation over the sagittal plane (i.e. the arm elevation plane). Moreover, the SEA output is rigidly linked to the arm interface, thus it transmits the applied torque to the human arm aiding the user in executing elevation motions. This emphasizes the critical structural role of the flexible link: being mounted on the SEA input, the flexible link is capable of withstanding the torque exerted by the SEA and safely redistributing it to the back interface. This specific design offers two key benefits: first, the SEA consistently assists arm elevation; secondly, the underactuated kinematic chain can structurally transmit the assistance torque from the SEA to the back at any point within the exoskeleton workspace. However, the kinematic chain of the exoskeleton is not compatible with the typical abduction/adduction motion performed with the arms positioned alongside the body. Nevertheless, the user is allowed to reach a comparable posture by combining the other compatible movements of flexion/extension and internal/external rotation.

2.2.2.2 Control & Communication Systems

All essential components for control and communication are housed inside a box that is embedded in Flexos backpack, making the device completely portable. These include the power storage system - a 24 V, 10 Ah LiFePO4 battery weighing 1 kg - the control unit, and the wireless communication system. The system is capable of continuous operation for at least 6 hours without the need for battery recharge.

The main control unit of the system is represented by a Teensy 4.1 board, which is integrated into a printed circuit board (PCB) that hosts all the connectors for power, sensors, and actuators. The control logic is written in C++ code, compiled, and deployed to the Teensy. The microcontroller operates at a rate of 1 KHz and manages bidirectional CAN communication with both actuators, configuring the desired current value and retrieving measurements of the angle, the speed, and the current of the motors. Furthermore, it handles the Synchronous Serial Interface (SSI) communication protocol through which the encoders embedded in the SEA transmit their measured angular displacements, thus allowing the computation of the corresponding joint torque values. Additionally, the microcontroller manages I2C communication with the IMUs. There are three BNO055 IMU boards mounted on Flexos: the first one is placed on the back interface and serves as the main reference

Table 2.1 Control parameters

Parameter	Value
Joint stiffness k_j	72.4 Nm/rad
Motor torque constant K_T	0.75 Nm/A
Max. system output torque τ_{max}	9 Nm rated, 18 Nm max
Proportional gain K_p	1.5
Derivative gain K_v	0.015 s
Integral gain K_i	0.50 s^{-1}
Velocity contribution gain K_{imu}	0.01 Nm $*$ s/rad

for the other two IMUs that are located on each arm interface and measure the arms' Euler angles and angular velocities.

The control unit facilitates data exchange with an external device using the UDP network protocol through the Teensy Ethernet interface. This interface is linked to a multi-port router switch with four Ethernet ports and a wireless LAN interface, enabling WiFi communication between the control unit and an external PC. The external PC, which operates at a 500 Hz, can dynamically adjust control parameters (e.g., maximum desired torque, control gains, and operating mode), while also retrieving all the relevant data gathered by the Teensy board.

2.2.2.3 Torque controller

Flexos is torque-controlled to ensure safe pHRI. The SEA has an encoder sensor embedded in the series elastic joint measuring the joint's elastic displacement, which has been already characterized and mapped to the correspondent joint torque value in a previous work [264]. These values are subsequently used to implement a precise closed-loop torque controller, whose scheme is described in Fig. 2.2 (b). The primary goal of this controller is to partially compensate for the gravity torque that arises from the arm weight - either alone or eventually with a lifted object - during the elevation motion. However, the system output torque is saturated by the control to 5 Nm, since previous experimental evaluations revealed that higher torque values could lead to localized deformations in the 3D-printed parts the current Flexos version uses. Such deformations could compromise the structural integrity of the device and, consequently, its performance in assisting the user.

Key control parameters concerning the torque controller are detailed in Tab. 2.1.

The SEA provides an estimate of the joint torque based on Eqn. 2.1:

$$\tau_j = k_j \sin\left(\frac{\gamma}{2}\right) \tag{2.1}$$

where the estimated joint torque τ_j is computed in relation to the angular displacement γ, and the first-order joint stiffness k_j was experimentally evaluated in [264] and is reported in Tab. 2.1. This estimate results is a feedforward component that is combined together with the feedback control law u. The latter is based on a PID controller, whose gains are tuned with the Ziegler-Nichols method and reported in Tab. 2.1. The resulting motor torque command τ_m is converted into a current value and sent to the motors.

The desired torque reference τ_{des} for the closed-loop controller is obtained by the Gravity Compensation Model plus an additional velocity contribution as shown in Eqn. 2.2:

$$\tau_{des} = \tau_{max} \sin(q - \phi) + K_{imu}\omega \tag{2.2}$$

where τ_{max} represents the maximum system output torque. As shown in Fig. 2.2 (b), the arm elevation angle q is obtained by subtracting the series elastic joint angular displacement γ by the motor angular position θ, both measured by their respective encoders. The IMU located on the back interface measures the misalignment between its vertical axis - parallel to the user's back plane and thus to the longitudinal axis - and Earth's gravity vector. The resulting angle ϕ is subtracted to q and the obtained assistance becomes proportional to the difference between the two antagonist angles. Additionally, the desired torque reference τ_{des} is proportional to the shoulder flexion speed ω, which is measured by the IMUs located on each arm interface and then scaled by a constant value K_{imu}. By taking into account the flexion/extensions angular speed, an additional contribution is aimed to be provided to the controller reference generation that takes into account the user's intentions.

2.2.3 Experiments

2.2.3.1 Participants

A series of in-lab experiments were performed on nine healthy subjects (27.64 $\pm$ 2.46 years old, all males), with only one left-handed - with neither previous history of neuromotor disorders nor a former familiarity with occupational exoskeletons. The experimental protocol conformed to the ethical standards laid down in the 1964 Declaration of Helsinki. Ethical approval for the study was granted by the Scuola Superiore Sant'Anna Review Board, ID 152021, and before commencing the experiments, written informed consent was obtained from each participant.

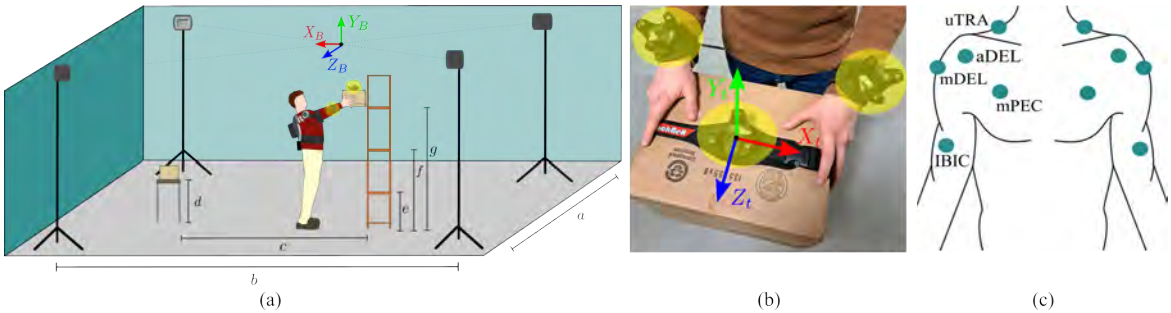

(a) (b) (c)

Fig. 2.3 Experimental setup. The room for the experiments is shown in (a): the subject's motion path includes a starting platform where the package is lifted from and a final shelving unit where the package is shelved. Three different shelf heights, which are labeled as e, f, and g, are encompassed in this experiment. The base stations are located at the four corners of the room such that there is no occlusion among them and each marker is always tracked by at least two base stations. The base stations generate an absolute coordinates system $(XYZ)_B$ that serves as a reference for the individual coordinates system $(XYZ)_t$ of the three used trackers (b). One tracker is positioned at the top-center of the box, whereas the other two trackers are located at the user's wrists. (c) EMG Trigno sensor positioning. Each sensor is located along the longitudinal midline of each targeted muscle, thus the sensor midline is parallel to the muscle fiber direction.

2.2.3.2 Experimental Setup

The in-lab assessment of Flexos aims to evaluate how effective the exoskeleton is in supporting the user during repeated activities requiring upper limb elevation. This efficacy is tested by focusing on two main aspects: on the one hand, the achievable ROM is measured and the movements of the upper limbs are tracked inside the workspace; on the other hand, both the perceived exertion and the muscular effort that is required to perform each task are evaluated to assess whether the exoskeleton manages to reduce them.

ROM is computed through the IMUs located on each arm interface, which are also used for motion tracking together with a virtual reality tracking system [265]. This latter consists of four HTC SteamVR Base Station 2.0, located at the four corners of the experiments room (Fig. 2.3 a), and three VIVE Tracker 3.0, two of which are positioned on each subject's wrist and the third of which is located on the target box (Fig. 2.3 b). Trackers and base stations are managed by SteamVR which acquires linear and angular positions and speeds at 250 Hz.

Muscular effort evaluation involves measuring the electromyography (EMG) activity of five specific muscles - biceps brachii (lBIC), anterior deltoid (aDEL), medial deltoid (mDEL), pectoralis major (mPEC), and upper trapezius (uTRA) - during the experiments tasks, each of which will be repeated in two different conditions: with (w. Exo) and without (w.o. Exo) the exoskeleton worn and powered on. EMG signals have been recorded using a Trigno

Table 2.2 Experiments - room dimensions and distances

Parameter		Value [m]
Distance between base stations $\perp$ path	a	5.70
Distance between base stations // path	b	8.60
Path length	c	3.20
Starting table height	d	0.82
Shelving unit, *lower* shelf height	e	0.69
Shelving unit, *middle* shelf height	f	1.20
Shelving unit, *top* shelf height	g	1.59

Wireless Biofeedback System (Delsys, Natick Massachusetts, USA), which comprises a main base station and two types of wireless EMG sensors - Trigno Avanti and Trigno Quattro EMG Sensors - as shown in Fig. 2.3 (c). Each targeted muscle is monitored with one EMG sensor unit carefully placed by following the SENIAM recommendations [266]. A Delsys Trigger Module is used for synchronizing the EMG data with the trackers and exoskeletons data, acquired by the main control unit. The recorded data are then exported and processed using MATLAB. The raw EMG data undergoes band-pass filtering (35-450 Hz), full-wave rectification, and a low-pass filtering (6 Hz) via a zero-phase second-order Butterworth filter. The EMG activity is then normalized using the maximum voluntary contraction (MVC) value of each different subject. Furthermore, EMG signals have been segmented by taking the linear position of the object as a visual reference.

2.2.3.3 Experimental Protocol

Flexos experimental protocol is based on four main tasks, structured as follows:

- **Range of Motion (ROM) task**: the participant is instructed to perform free movements with both upper limbs, with the purpose of reaching the limits of the shoulders' range of motion.
- **Isometric task**: the participant is asked to hold a box with both hands while keeping both arms elevated - horizontal, at 90 $^\circ$ elevation on the sagittal plane - until either voluntary exhaustion [267] or for a maximum of 2 minutes.
- **Dynamic task**: the participant is asked to stay in front of a shelving unit that is made up of three shelves in total. Note that the shelf, whose characteristics are depicted in Fig. 2.3 (a) and numerically reported in Table 2.2, is the same for all subjects. Such characteristics should have been tailored to the subject's anthropometric characteristics

(height, arm length) for the sake of a fair comparison. However, it has not been modified since the inter-subject variability in terms of height is low (183.4 ± 3.1). Each participant is then asked to stay at a reference distance of 70 cm from the shelf unit before starting to perform the dynamic task. The task is divided into two main motor actions, that combined together form a whole trial.

1. *Upwards motion*: The participant is instructed to grab with both hands a box located at the *middle* shelf and shelve it onto the *top* shelf; then, he brings both arms back in the resting position - parallel to the trunk.
2. *Downwards motion*: The participant grabs with both hands the box, now located at the *top* shelf, and he shelves it back onto the *middle* shelf. After that, he brings both arms to the resting position.

Each transition - up, down, rest - is performed between two consecutive beats of a metronome set at 20 bpm. The task is performed for a maximum of 2 minutes.

- **Carrying-Load task**: This task is inspired by the experiments of Theurel et al. [245] and it is divided into three main motor actions as shown in Fig. 2.4.

  1. *Pickup*: The participant is asked to stand in front of the table where the box is located, then grab the box with both hands and lift it performing a flexion movement until the arm elevation on the sagittal plane reaches $90\,^{\circ}$.
  2. *Carrying*: The participant turns around and walks towards the shelving unit in front of him. While walking, he keeps carrying the box with arms at $90\,^{\circ}$ elevation on the sagittal plane. The participant is asked to synchronize each step with the beat coming from a metronome set at 80 bpm.
  3. *Release*: The participant reaches the shelving unit and leaves the box on one of the three shelves.

  The three actions are then repeated in the opposite direction, meaning that the subject lifts the box from the shelving unit and carries it towards the table where he will leave it, thus completing a whole cycle, namely trial. At each subsequent cycle, the subject is asked to shelve the box in a different layer of the shelving unit (in order, *middle*, *top*, *middle*, *lower*). The metronome also supports an additional paced action: each phase is preceded by a brief pause where the subject is requested to stand still while holding the box for three consecutive beats. This will help identify motor actions while inspecting

(a) (b) (c) (d)

Fig. 2.4 The three phases of the Carrying-Load Task. (a)-(b) *Pickup*, (c) *Carrying*, (d) *Release*.

signals in post-processing. The whole task is executed until voluntary exhaustion or for a maximum of 10 minutes.

Isometric and dynamic tasks are performed twice, each time with a box of different masses - 3 kg and 5 kg -. The masses order is pseudo-randomized each time. The carrying load task is only performed with the 3 kg box, in order to prevent the subject from excessive fatigue since this task is the longest one. Every task has been repeated both with Exo (w. Exo) - torque controller powered on - and without (w.o. Exo). The task order has been randomized to be different for each participant. Only the ROM task is not randomized and always executed before all the others since it is only performed w. Exo but with torque controller powered off. The participant is required to rest for a minimum of ten minutes between two subsequent executions of each task, to allow muscle relaxation before proceeding to the next task, thus preventing fatigue from altering the results [268]. Note that the maximum duration of dynamic and carrying-load tasks was chosen to both optimize the global experimental time and attempt to acquire a sufficient amount of data to assess the influence of the exoskeleton [269]. After each task, to collect a qualitative assessment of the task load, the participants filled the 20-point scale NASA Task Load Index (NASA-TLX) questionnaire made up of 6 items, mental demand (MD), physical demand (PD), temporal demand (TD), performance (P), effort (E), and frustration (F) [270]. In addition, the Borg CR-10 [271] questionnaire has been included to qualitatively evaluate the rate of perceived exertion (RPE) as well.

2.2.3.4 Metrics and statistical analysis

Different metrics have been extracted from the processed data in both w. and w.o. Exo conditions to quantitatively verify the efficacy of Flexos in supporting the subject. More

in detail, the execution time has been evaluated only for the isometric time, whereas two EMG-based indexes have been considered for all the tasks. The endurance time (ET), which is the duration of the isometric task, is computed as the time elapsed from the first to the last instant in which the subject kept the shoulder flexed of 90 °. The muscular effort (ME) has been defined as the root mean squared (RMS) of each processed EMG signal and its computation varies with each task. In fact, the ME values may be biased from a delay of the fatigue onset, since subjects could reach fatigue at different times with and without support. Hence, for the sake of a fair comparison, the minimum time between the w.o. Exo and w. Exo conditions have been considered for each task. Afterward, the RMS is computed on the length of the whole signal for the isometric task, whereas it is calculated within all the phases or subphases of the dynamic and carrying-load tasks, respectively.

The normality distribution of these metrics is checked by means of a Shapiro-Wilk test with a significance level of $\alpha = 0.05$. Consequently, the value of these metrics in the w. Exo condition is statistically compared with the one in the w.o. Exo condition through a non-parametric Wilcoxon signed-rank test for non-normally distributed sets and with a paired t-test ($\alpha = 0.05$) for normally distributed ones.

2.2.4 Results

2.2.4.1 Tasks overview

The outcome of the ROM task is determined by the Euler angles measured with the IMUs located on each arm interface. The kinematic model for ROM measurements is compliant with the Thorax coordinate system recommended by the International Society of Biomechanics (ISB) [272]. Table 2.3 presents the results for shoulder flexion/extension and internal/external rotation. To ensure consistency with the literature, these results are compared with the normal values of forward flexion, backward extension, and inward/outward rotation stated by Boone et al. (1979) [273]. The results show how Flexos facilitates extensive coverage of human ROM, achieving an average of 89.2% for flexion/extension motion and 88.4% for internal/external rotation.

Considering a representative subject of the collected dataset, Figure 2.5 (a) shows the temporal evolution of the vertical position of the object that is moved upwards (i.e., from the middle to the upper shelf) and downwards (i.e., from the upper to the middle shelf) in the dynamic task, using the reference system that is shown in Fig. 2.3 (a). Moreover, the processed EMG signal of the right aDEL is shown, reflecting the corresponding muscular activation. For both signals, the inter-trials mean has been included and the time axis has

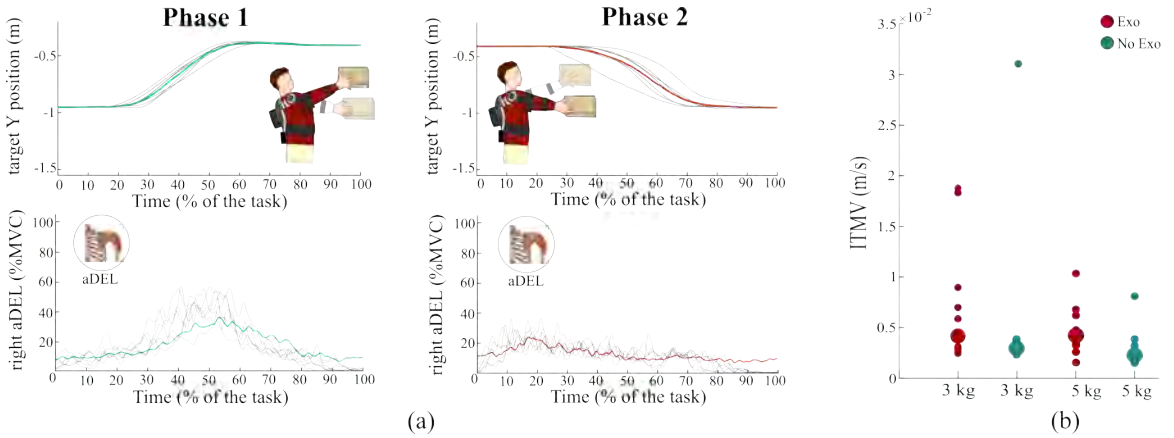

Fig. 2.5 (a) Position of the target box and muscular activation of the right anterior deltoid during the dynamic task. The gray lines are related to single trials, while the colored lines represent the inter-trial mean among corresponding signals. (b) Inter-trials mean velocity during the dynamic task.

been normalized. Both phases (upwards and downwards motions) can be divided into three subphases, which are: a) a reaching subphase that lasts 25% of the whole time cycle on average, b) a moving phase that lasts from the 25% to the 70% of the whole time cycle on average, and c) a release phase that lasts for the remaining 30% of the time cycle on average.

Furthermore, as additional information concerning the outcome of the task, the distribution of the inter-trials mean velocity (ITMV) was computed to demonstrate how each group of tasks was executed as much as possible at the same speed to exclude the effect of movement speed on the effort evaluation. The statistical test revealed that the ITMV during the dynamic task, Figure 2.5 (b), shows no substantial difference between the w. Exo and w.o. Exo conditions, highlighting how the velocity has not noticeably changed during the dynamic task.

Considering a representative subject of the collected dataset, Figure 2.6 (a) shows the temporal evolution of the vertical position of the lifted object during the release and pickup

Table 2.3 Shoulder ROM. Ground truth data for healthy subjects are taken from [273] and compared to the ROM covered with Flexos. Values are reported in mean ± standard deviation.

	w.o. Exo [273]	w. Exo
Flexion	$166.7^\circ \pm 4.7^\circ$	$149.2^\circ \pm 9.24^\circ$
Extension	$62.3^\circ \pm 9.5^\circ$	$55.1^\circ \pm 9.0^\circ$
Internal Rot.	$68.8^\circ \pm 4.6^\circ$	$66.7^\circ \pm 4.9^\circ$
External Rot.	$103.7^\circ \pm 8.5^\circ$	$85.7^\circ \pm 3.4^\circ$

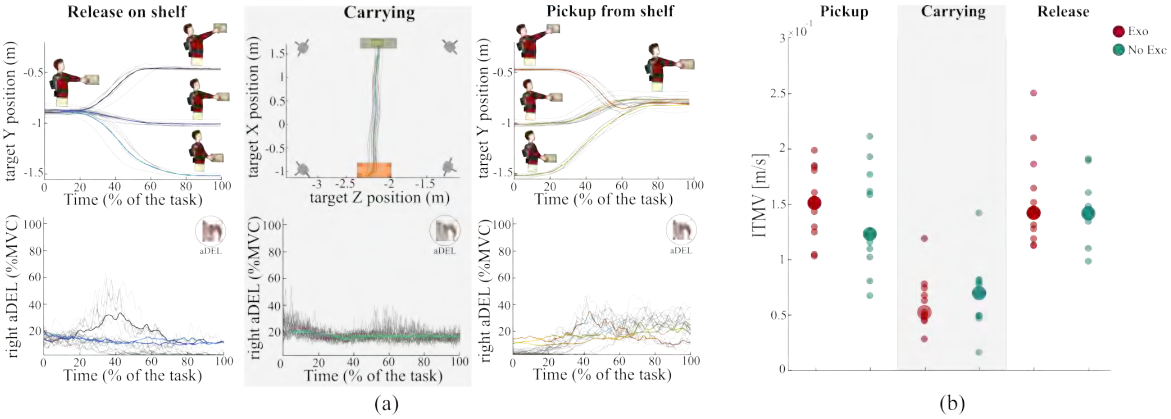

Fig. 2.6 (a) Position of the target box and muscular activation of the right anterior deltoid during the carrying-load task. The gray lines are related to single trials, while the colored lines represent the inter-trial mean among corresponding signals. (b) Inter-trials mean velocity during the carrying-load task.

subphases of the carrying-load task for each shelf height, as well as the trajectory of the object (i.e., position on the z-x plane) moved from the platform to the shelving during the carrying subphase of the same task. These signals trajectories are expressed in the reference system that is shown in Fig. 2.3 (a). The EMG signal of the right aDEL, reflecting the muscular activation of the corresponding targeted muscle, is depicted as well. For both signals, the inter-subject mean has been included and the time axis has been normalized. The release subphase may be further divided into a reaching stage lasting the first 20% of the whole time cycle on average, a releasing stage lasting from the 20% to the 60% of the whole time cycle on average, and a resting stage for the remaining 40% of the time cycle on average. Similarly, the pickup subphase can be divided into a reaching stage lasting the first 25% of the whole time cycle on average, a picking stage lasting from the 25% to the 70% of the whole time cycle on average, and a holding stage for the remaining 30% of the time cycle on average. Moreover, muscular activation increases on average as the height of the shelf on/from which to release/pick the object is greater. On the other hand, during the carrying subphase, the EMG signals oscillate around a mean value as the subjects move the object from the platform to the shelving while walking.

Moreover, the distribution of the ITMV during the carrying-load task is again computed as for the dynamic task and reported in Figure 2.6 (b). The statistical test revealed that the ITMV during the carrying-load task does not significantly differ between the w. Exo and w.o. Exo conditions and, since the difference between the two conditions is small, the velocity has arguably no notable changes during the execution of the carrying-load task.

2.2.4.2 Outcomes

Several indexes have been extracted from the processed EMG signals to evaluate whether Flexos effectively supported the subject in weight-lifting tasks.

Endurance time The endurance time has been quantified for the isometric task, thus finding that ET differs in each condition and for each mass. As shown in Fig. 2.7 (b), ET in the Exo condition is higher than in the w.o. Exo condition for both masses. Therefore, the exoskeleton effectively increased the subject's endurance during the isometric task.

Muscular effort The distributions of the ME during the isometric task for all subjects is reported in Fig. 2.7 (a). The median of ME during the isometric task in the w. Exo condition is lower than the one in the w.o. Exo condition in almost all cases, though without statistical significance Nonetheless, no muscle was penalized by the introduction of Flexos; hence, from a general point of view, the ME values underline the benefits of employing an occupational exoskeleton for isometric tasks.

The distributions of ME during the dynamic task for all subjects are reported in Fig. 2.8. The median of ME during the dynamic task in the w. Exo condition is higher than in the w.o. Exo condition only in one case - left lBIC when moving a 5 kg mass, that is a muscle not directly supported by the exoskeleton -. However, compared to the corresponding one in the w.o. Exo condition, the reductions are slightly lower than in the previous case (i.e. isometric task), particularly for the mDEL and aDEL.

The distributions of ME during the carrying-load task for all subjects, divided by sub-phases (i.e., pickup, carrying, release), is reported in Fig. 2.9. Such outcomes may be

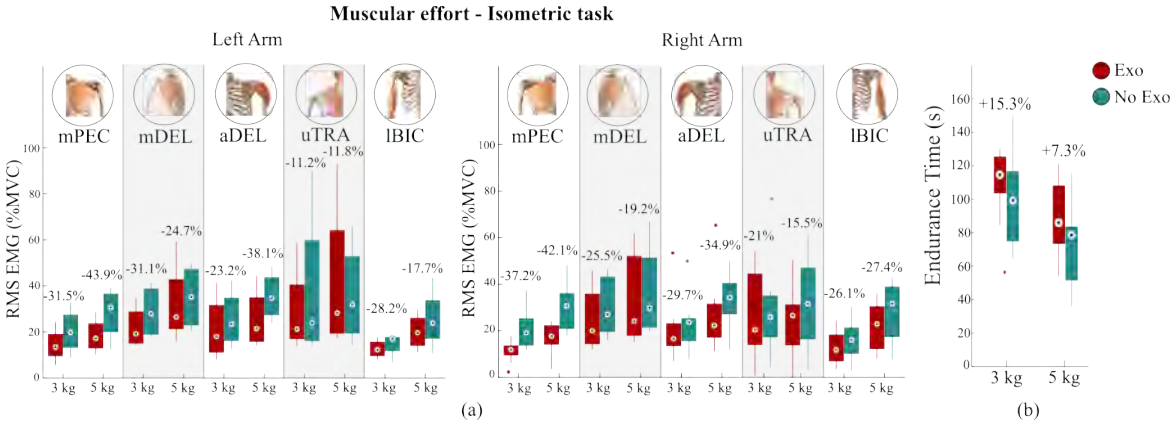

Fig. 2.7 (a) RMS during isometric task. Percentage differences in RMS between w. Exo and w.o. Exo conditions are reported. (b) Endurance time during isometric task.

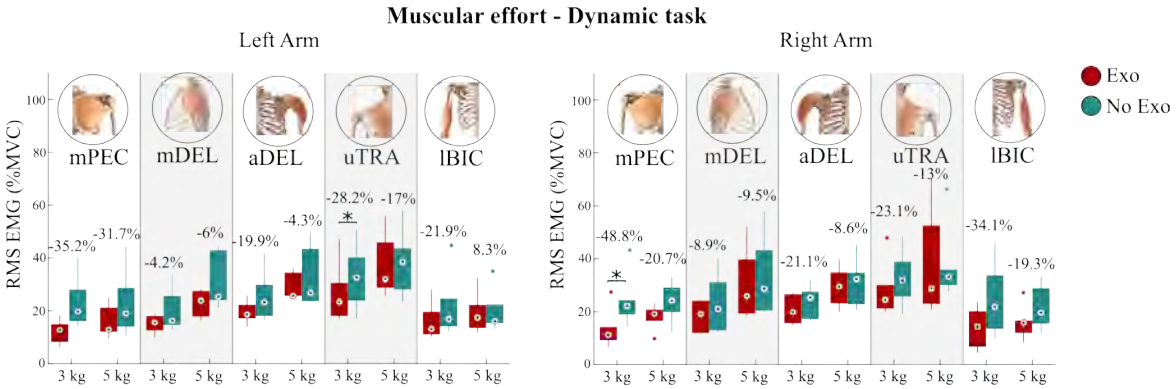

Fig. 2.8 RMS during dynamic task, with * representing statistically significant comparisons with $p < .05$. Percentage differences in RMS between w. Exo and w.o. Exo conditions are reported.

regarded as intermediate between those of the isometric task and those of the dynamic task in terms of the amount of both statistically significant reductions and variation between the w. Exo and w.o. Exo conditions. The most relevant reductions concern the carrying phases, which require to performing isometric contractions for a longer time.

Fig. 2.10 reports the scores of the NASA-TLX and RPE questionnaires related to both w. Exo and w.o. Exo conditions by means of two different polygons. More in detail, the scores related to the w. Exo conditions are lower than the ones of the w.o. Exo condition for all items; notably, this difference is statistically significant for PD with $p < .001$, as well as for E and F with $p < .01$. In addition, the RPE scores related to the w. Exo condition is significantly lower than the ones of the w.o. Exo condition with $p < .01$. These outcomes, although subjective, confirm that the perceived workload is reduced when Flexos support the subject's motor actions.

2.2.5 Discussion

This work presented the design and control of the Flexos, a fully portable and active shoulder exoskeleton for direct assistance in the workplace. The system design and control have been described in detail, leading to an in-lab experimental assessment performed over nine healthy subjects to evaluate Flexos' capabilities in helping the user to perform weight lifting movements and moving objects tasks, as well as shelving operations. The device performance is tested both in terms of ROM evaluation and reduction of the muscular effort required to perform weight lifting, carrying, and shelving tasks.

2.2.5.1 Flexos' design features

The adoption of occupational exoskeletons still presents challenges, notably concerning the comfort and the consequent acceptability of these devices among workers. To address this, the design of ergonomic human-robot interfaces and the achievement of a broader ROM were prioritized. The resulting device was pleasantly received by the participants during the study, as hinted by the generally decreased NASA-TLX scores shown in Fig. 2.10 (a).

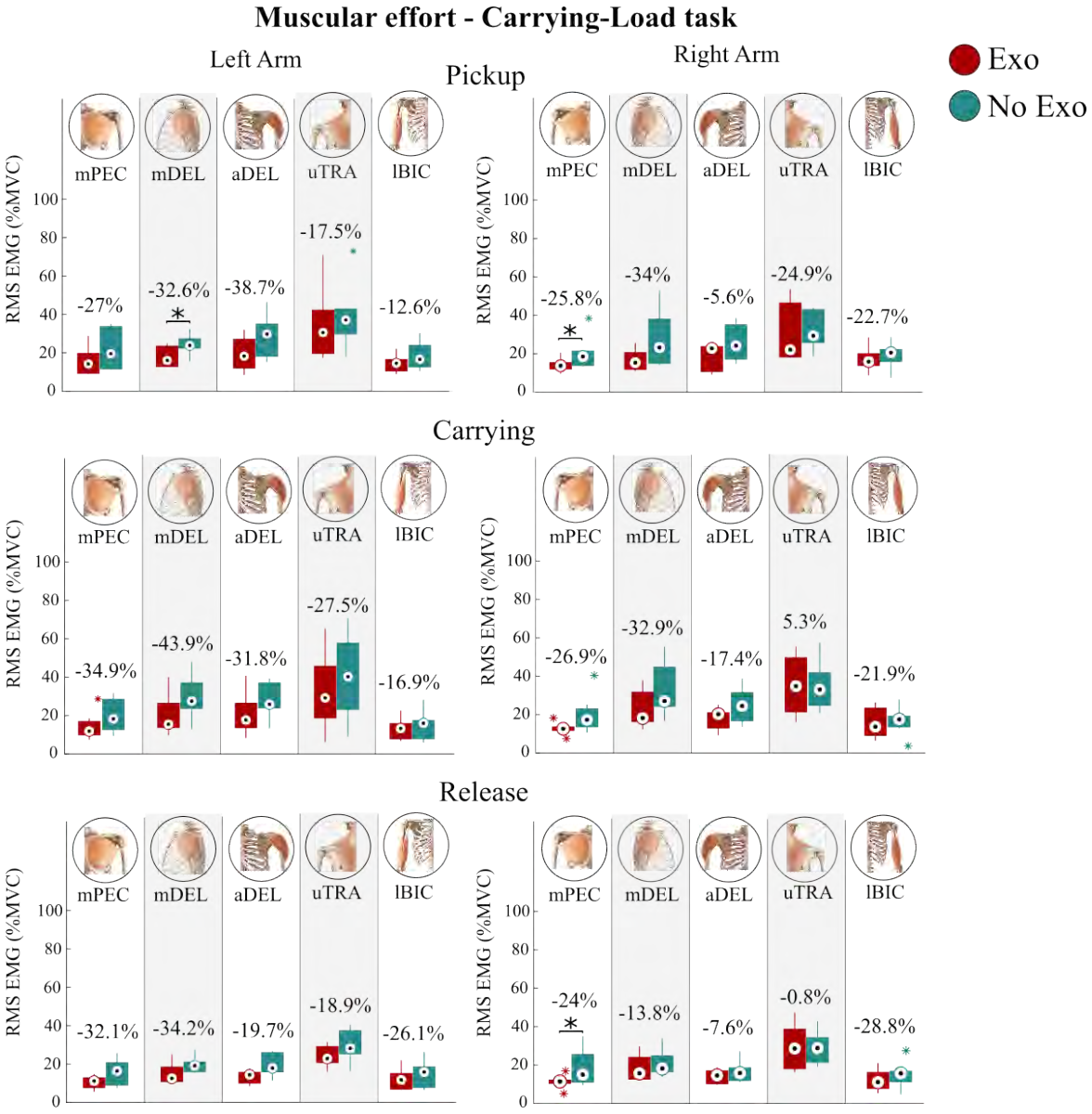

Fig. 2.9 RMS during the three main phases of the carrying-load task, with * representing statistically significant comparisons with $p < .05$. Percentage differences in RMS between w. Exo and w.o. Exo conditions are reported.

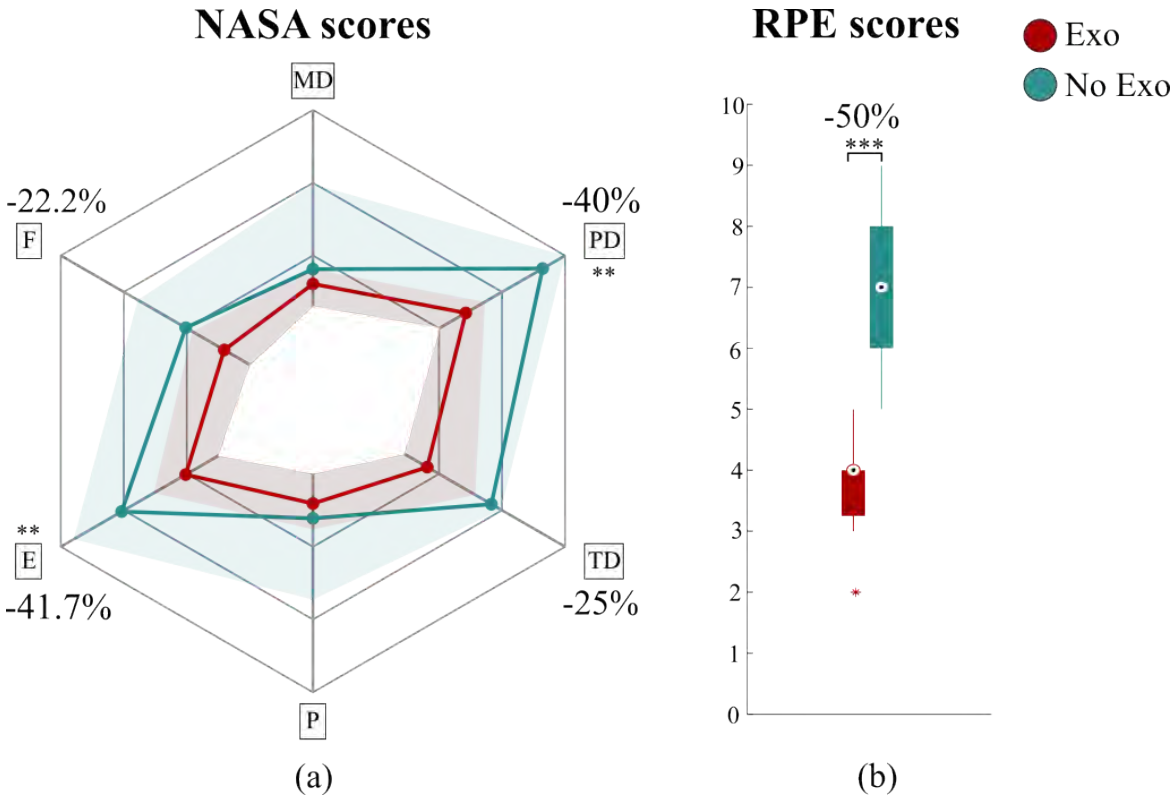

Fig. 2.10 Results of NASA-TLX and RPE questionnaires, with ** and *** representing statistically significant comparisons with $p < .01$ and $p < .001$, respectively. (a) The score distributions are depicted with a different polygon for each condition (i.e., w. Exo and w.o. Exo), as well as with the median highlighted through a thick line. (b) RPE scores. Moreover, the percentage differences in questionnaire scores between w. Exo and w.o. Exo conditions are reported. The darker color refers to w. Exo condition while the lighter color refers to w.o. Exo.

Particularly, the reduced level of Mental Demand (MD) and Frustration (F) is possibly due to multiple factors: the system's lightweight design and its back-drivability, which allows for high mobility even with powered-off torque controller; the employment of soft garments at the human-robot interfaces, facilitating a comfortable load transfer to the human body; the adoption of the new bi-manual configuration, enabling the user to perform more complex tasks with both hands, with no reports of discomfort highlighted during the experiments with respect to a previous work [218] where Flexos was only one-sided.

Moreover, participants did not complain about the impossibility of performing a direct shoulder abduction/adduction motion when the arm is placed along the body, as the other available DOF ensured enough mobility to cover most of the shoulder ROM. Percentages - flexion/extension 89.2%, external/internal rotation 88.4% - show no substantial difference in the shoulder ROM between w. Exo and w.o. Exo conditions. Additionally, this configuration has the possible advantage of being underactuated, with the exoskeleton kinematic chain capable of bearing the actuation torque, contrary to a previous solution [263].

Lastly, participants were positively affected by the modifications in the torque controller, i.e. the additional torque reference signal depending on the arm velocity, as suggested by the decreased score of Physical Demand (PD). Indeed, subjects reported feeling increased assistance when manipulating the target mass in the pick-up/releasing phases, characterized by less effort in upper arm movements.

2.2.5.2 Comparison in muscular activity

The experimental protocol has been designed to reproduce in a laboratory the targeted use of the exoskeleton. The new tasks are more complex and more adherent to real-life workplace activities than in a previous preliminary study [218]. The protocol of the present study is thus characterized by an additional layer of complexity that makes it different from the majority of related works, which are usually centered on a reference trajectory to follow. Nonetheless, the concept and the methodology are promising. Particularly, Fig. 2.11 reports the average muscular activity reductions obtained with the experiments on the current Flexos system: average reductions range from 15% to 39%, from 7% to 34%, and from 14% to 32% for the isometric, dynamic, and carrying-load tasks, respectively. These results are consistent with similar studies in the literature. Theurel *et al.* [245] obtained an average reduction of 54% in the dynamic (lift) task and 40% in the walking task for the anterior deltoid (aDEL) by using a passive exoskeleton with eight subjects for manipulating a target mass whose weight ranged from 5 kg to 15 kg depending on both the task type and the participants' gender. Grazi *et al.* [235] managed to obtain average reductions of 33% (aDEL), 41% (mDEL), and 33% (uTRA)

employing their semi-passive upper-limb exoskeleton H-PULSE during prolonged continuous overhead activities with nine subjects. Pacifico *et al.* [274] performed experiments with the proto-MATE, a passive upper-limb exoskeleton, on fifteen subjects, resulting in average reductions that lie in the range 18% - 35% and 18% - 38% during dynamic (reaching) and isometric tasks, respectively. Pinto *et al.* [275] studied the effects of wearing a passive shoulder exoskeleton for overhead tasks, resulting in an average reduction of 27% (aDEL), 38% (mDEL) and 33% (uTRA). Missiroli *et al.* [268] proposed an OE for upper limbs with a hybrid configuration - the shoulder is passively actuated while the elbow is active - that could reach average reductions of 31% (aDEL), 22% (mDEL) and 33% (lBIC) during shoulder abduction in dynamic (tracking) tasks. De Bock *et al.* [246] assessed the effect of wearing a passive shoulder exoskeleton prototype for overhead tasks, obtaining average reductions of 25% (aDEL), 29% (lBIC) and 20% (mPEC). Lee *et al.* [276] proposed a novel passive shoulder exoskeleton employing magnetic spring joints and they tested the prototype while performing overhead drilling and box-lifting tasks, resulting in average reductions of 34% (aDEL), 25% (mDEL) and 3% (uTRA). It is evident how the majority of exoskeletons with similar assisting purposes - upper-limbs devices for assisting arms flexion/extension - are often passive. On the one hand, these devices manage to obtain relevant reductions in the user's muscular activity; however, due to their passive actuation system, such exoskeletons do not allow for modifying in real-time the delivered torque. In a previous work [263], where an active exoskeleton was designed with bowden cable remote actuation, thus still not portable, the muscular activity decreased by 32% (aDEL), 57% (mDEL) and 45% (lBIC) for the static task and by 25% (aDEL), 50%(mDEL) - with lBIC showing a not significant reduction - for the dynamic task. Finally, the preliminary study conducted with the previous version of Flexos [218] led to reductions rangin from 11% to 42% and from 2% to 37% for the static task holding 2 kg and the dynamic task, respectively. These results differ from the ones obtained with the new experiments, despite being always centered on the Flexos prototype. This can be mainly due to the bilaterality of the current Flexos instead of the unilaterality of the old preliminary study; besides, the previous experiments were characterized both by a lower sample size and thoroughly different (and simpler) tasks.

Other relevant features from related work are reported in Table 2.4 for further comparisons.

2.2.5.3 Limitations

Despite the promising results, this study highlighted some issues, starting from the restricted size of the experimental sample, which could be addressed by recruiting new participants

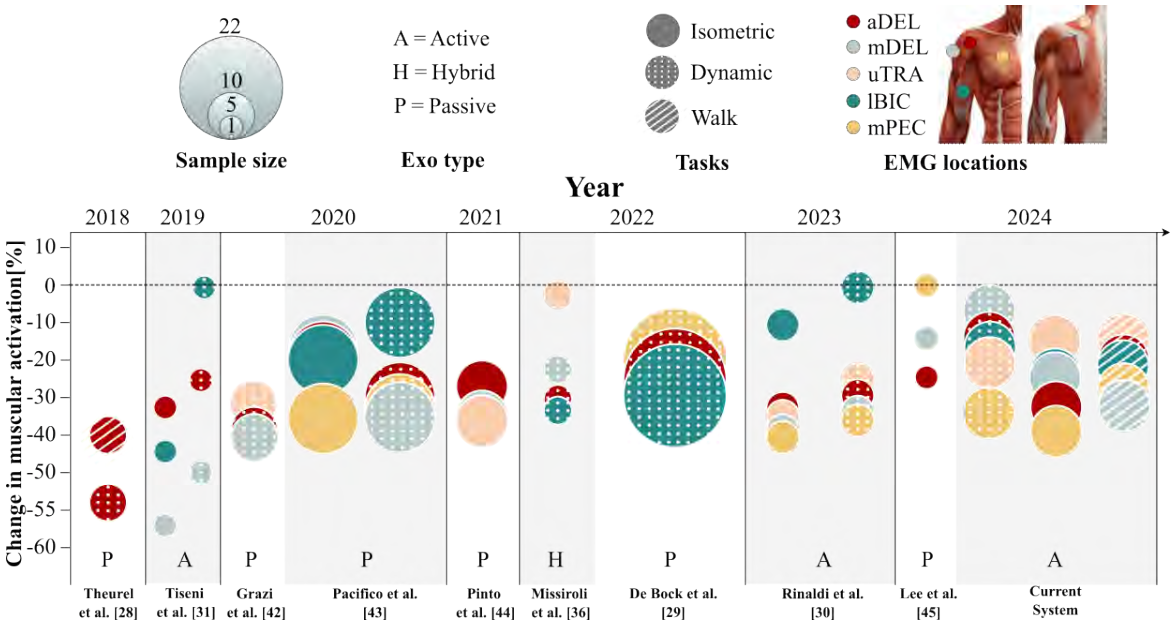

Fig. 2.11 Related works employing similar exoskeletons supporting the shoulder flexion. Changes in muscular effort are reported with circles, whose size and color represent the sample size and the muscle whose activity, respectively. Acronyms: aDEL - anterior deltoid; mDEL - medial deltoid; uTRA - upper trapezius; lBIC: biceps brachii; mPEC: pectoralis major.

Table 2.4 Relevant features from related works, reported for comparisons among prototypes.

	Theurel et al. [245]	**Tiseni et al.** [263]	**Grazi et al.** [235]	**Pacifico et al.** [274]	**Pinto et al.** [275]	**Missiroli et al.** [268]	**De Bock et al.** [246]	**Rinaldi et al.** [218]	**Lee et al.** [276]	**Current System**
Mass (kg)	9	2.45	5	3.5	3	6.4	3.8	4.8	1.9	7.6
Actuation Type	Passive	Active	Passive	Passive	Passive	Hybrid	Passive	Active	Passive	Active
Max Torque *Absolute* (N m)	assistance at EE up to 135° (flex.)	20	6	5.5	ND	ND	3	9	5	9
Max. Torque *Experiments* (N m)	assistance at EE 9 kg (Males) 5 kg (Females) up to 90°	2.5	4.58 (Low) 5.38 (Medium) 5.85 (High)	4	ND	ND	3	5	2.5	5
Target Load Mass (kg)	15 (Males) 8 (Females)	0	0	0	0	1.5	5 (static tasks) 10 (dynamic tasks)	2	1.2 (drilling task) 5 (lifting task)	3, 5 (static task) 3, 5 (dynamic tasks) 3 (carrying-load task)
Body Side	Both	Right	Both	Both	Both	Both	Both	Right	Both	Both

even among females in order to increase inter-subject variability in terms of anthropometric characteristics and muscular tonicity.

Moreover, the choice of the material still put a limitation over Flexos' full assistive potential: all the SEA torque could not be entirely used due to the insufficient stiffness in the flexible link, which resulted in torsional displacement under load. To better suit Flexos' future applications, subsequent iterations of the device will provide composite materials combining plastic and carbon fiber, to fully exploit Flexos' potential assistance.

The control strategy is another component of the proposed system that can be improved by compensating for a two-fold lack. At first, the user could benefit from modulating Flexos assistance for different payloads, which may be done by estimating the target mass that serves as a reference for the torque controller. In addition, a more advanced control strategy could be exploited to allow Flexos to exhibit better performance in dynamic tasks.

2.2.5.4 Future works

Most of the limitations mentioned above could be addressed by further developments of Flexos in the future. As an instance, since one of the main benefits of employing an active device is the possibility of integrating external sensors in the control loop, the torque controller could be enhanced by employing the IMUs to collect kinematics data of the user online, i.e. while wearing Flexos and performing a specific task. This data will be used in the torque controller to adjust the assistance based on the user's posture, thus ensuring a satisfying level of ergonomics to be compliant with the main requirements for a device to be employed in the workplace.

Secondly, the extra assistive contribution of the torque controller needs further investigations to fully take into account the user's intention in future versions of the device.

Furthermore, textile interfaces, which are a set of harnesses worn by the subject instead of rigid robotic devices, may provide an additional benefit for reducing fatigue: for instance, Georgarakis et al. used a textile exosuit to delay the onset of fatigue during isometric contraction of upper limb muscles [250].

Lastly, an in-lab assessment of Flexos is performed as this is the first step towards a possible final goal which is the adoption of this device inside the workplace. The next step will be an in-field assessment where real workers are enrolled to perform tasks in a real industrial scenario.

2.3 Muscle networks analysis on an active occupational shoulder exoskeleton

Muscle networks depict the way in which different muscles, controlled by different neural drives from different areas of the motor cortex, can share the oscillatory input, thus generating connections. It has been hypothesized that these networks can show how the brain can achieve coordinated movements with so many degrees of freedom, through neural coherence. It is worth wondering what happens to these structures when an assistive exoskeleton is employed. This research investigated the answer to this question by analyzing functional muscle networks of healthy subjects during isometric and load-carrying tasks with and without an occupational exoskeleton.

The contribution of this work to the state of the art is the presentation of a full comparative muscle networks analysis of healthy subjects during the execution of a) a pure bilateral isometric task and b) a bilateral load-carrying task, with and without Flexos, which is an occupational upper-limb exoskeleton. This study has been found to be the first one investigating the influence of an upper-limb exoskeleton on human motion features by means of muscle networks. Hence, this work presents:

1. an overview of what muscle networks are and how they have been analyzed and used in literature;

2. a complete description of the methods for computing muscle networks;

3. the comparison of networks and the correspondent features with and without the support of the upper-limb exoskeleton, together with an extensive discussion of what networks' metrics mean in terms of a physiological motion strategy and how the changes in their value could practically mean for healthy subjects.

This entire analysis also includes a discussion on muscle synergies, which are extracted on the same dataset about what useful information can be caught on motor strategies by comparing them with muscle networks.

The hypothesis of this work is that muscle networks can be used to evaluate an exoskeleton from the point of view of retaining physiological motor patterns while using the device. Accordingly, if an assistive device does not alter subjects' physiological movement, muscle network metrics should not be very different when comparing the two conditions with and without the exoskeleton.

This section is structured as follows: Subsection 2.3.1 provides a description of the state-of-art of functional connectivity analysis; Subsection 2.3.2 offers an overview of the robotic device, the experimental setup and protocol followed for acquiring data, and the operations executed to extract muscle networks from raw data; the outcomes of this data analysis are reported in Subsection 2.3.3; ultimately, discussions and conclusions of the conducted study are presented in Subsection 2.3.4.

2.3.1 Related Works

Robotic exoskeletons have increasingly gained popularity in both the scientific and industrial communities for the possibility of supporting humans in performing motor tasks [243, 277]. Based on the context in which they operate, they can be used as rehabilitation devices [278, 279] and power augmentation devices [218, 280]. Power-augmentation is referred to as a way to boost human performance in certain tasks, like carrying or lifting loads, for military or industrial applications. This usually happens thanks to specific design features and control strategies that aim to provide more power after detecting the intention of movements or under specific user commands [230]. Despite the physical relief that these devices can provide, it has been hypothesized that they can alter users' movements leading to non-physiological patterns [281, 282], such as increasing gait variability (e.g., using a lower limb exoskeleton) or altering the activity of non-assisted muscles. The analysis of motor patterns can also involve the extraction of muscle synergies, which are motor primitives that have been hypothesized to be used by the central nervous system for the coordinated activation of different muscles towards the completion of motor tasks [283].

Muscle synergies, hence, would enable for unveiling human motor patterns with a lower number of parameters with respect to the number of all the recruited muscles. This has also a high importance when dealing with brain injury (e.g., hemorrhagic or ischemic stroke events), in which context abnormal motor patterns and compensation strategies can occur and be revealed [284, 285]. A few works explored whether a robot-aided motor task may alter such patterns. Scano et al. investigated the impact of a robotic manipulator on the muscle synergies related to the execution of reaching tasks by both healthy and post-stroke people [286]; both subject categories exhibited on average only an amplitude variation of pattern activations for three execution types (free movements, slow-speed robot, fast-speed robot).

Human muscular coordination can be investigated from a different perspective - i.e., highlighting the neural substrate [287] - by evaluating functional connectivity between muscles. Previous studies investigated the hypothesis that the basis of human cognitive

dynamics and motor coordination lies in the synchronous oscillations of neurons, leading to the communication among neuronal groups [288, 289]. In this context, neuronal coherence is the process during which the rhythmic excitability fluctuations of the activated neurons produce temporal windows in which they accept coherent inputs from other neurons that are activated at the same time [288]. Network theory allows to determine the so-called functional muscle networks, which reflect the mutual synchronization of different muscles [290]. Such networks are typically arranged among three frequency bands, which are the alpha, the beta, and the gamma (or Piper) bands [291].

Functional muscle networks have been widely and increasingly utilized in the scientific literature for plenty of applications. O'Keeffe and colleagues employed this EMG-based method to investigate the difference in inter-muscle connectivity during the execution of vocal [290] and dynamic motor tasks [292]. Functional connectivity analysis was applied also to locomotion tasks performed on a treadmill at different speeds by either walking [293] or running [294]. Kerkman et al. exploited inter-muscular coherence to assess postural control on both healthy adults [287] and children in developmental age [295]. Functional muscle networks were used to explore the mechanism behind fatigue onset as well [296, 297]. Topographical changes of muscle connectivity proved to be even biomarkers of the development of stroke in individuals performing either upper-limb [298, 299] or stabilometric tasks [300], as well as an additional tool to investigate the evolution of human locomotor control [301]. Rehabilitative enhancements of post-stroke individuals were captured through muscle network analysis either without [302] or with the aid of robotic exoskeletons [248].

2.3.2 Materials and Methods

The exoskeleton used in this work is Flexos, the shoulder occupational exoskeleton which has been extensively described in all its components in Subsection 2.2.2. Analogously, the participants and the experimental setup are the same as reported in Subsection 2.2.3, respectively.

2.3.2.1 Experimental Protocol

Participants have been asked to perform the following motor tasks.

1. **Isometric task**: the participant has to hold bilaterally a box with both shoulders flexed of 90 ° until voluntary exhaustion [267] or for at most two minutes.

2. **Load-carrying task**: In this task, which is inspired by Theurel et al. [245], the subject is asked to move the box by walking from the table to one shelving unit while keeping both shoulders flexed of 90 ° on the sagittal plane. The beat coming from a metronome set at 80 bpm has been used to synchronize footsteps. The subject was asked to follow the path in the opposite direction, or rather carry the object from the shelving unit to the table. In so doing, one cycle (i.e., trial) of the load-carrying task is completed. Participants were told to repeat the execution of the load-carrying task for ten minutes consecutively, or to stop the execution earlier if moderate fatigue was perceived.

A mass of 3 kg has been chosen for all the tasks such that the participant is not excessively affected by fatigue. Subjects were asked to perform all the tasks without the exoskeleton (w.o. Exo) and wearing the exoskeleton (w. Exo) with the torque controller powered on. A pseudo-randomized order for experimental conditions has been adopted to minimize bias due to any learning effects. A rest of ten minutes has been established between two subsequent executions of the tasks for allowing muscles to relax and avoiding excessive fatigue accumulation [268]. The maximum duration of the load-carrying task derives from a trade-off between the overall experimental time and the need for a highly enough dataset dimensionality [269].

2.3.2.2 Data processing

EMG data needs a preliminary processing stage to remove any possible sources of noise, which may be related either to human motion or the electrical grid. Such operations slightly change depending on whether muscle synergies or functional muscle networks have to be extracted.

Functional muscle network Therefore, raw EMG signals are processed by means of a band-pass filtering (5-500 Hz) and a full-wave rectification via a Hilbert transform [303]. These operations have been chosen to remove artifacts while keeping and even strengthening the information about the neural oscillatory modulations in the range of interest ($<$100Hz), considering the observed EMG signals coming from non-uniform motor unit action potentials [304, 305]. Afterwards, the values of each subject's maximum voluntary contraction (MVC) are employed to normalize the EMG data. Ultimately, EMG data are segmented according to the object linear position.

In addition, coherence matrices have been computed to evaluate the inter-muscular coherence (IMC), which indicates how muscle activations match each other at each frequency.

These matrices are computed as follows:

$$C_{xy}(f) = \frac{\left|P_{xy}(f)\right|^2}{P_{xx}(f) * P_{yy}(f)} \tag{2.3}$$

where P_{xy} is the cross-spectrum between the two signals x and y, P_{xx} and P_{yy} are the self-spectra of those signals, f is the frequency, and C_{xy} is the coherence between the EMG data. Such matrices are averaged across trials and subjects for the load-carrying tasks, as well as among subjects for the isometric one.

Subsequently, each averaged coherence matrix is decomposed by means of the non-negative matrix factorization (NNMF) [306], thus obtaining a r-ranked matrix IMC_{f*n} according to the following formula:

$$IMC_{f*n} = (W_{f*r} \cdot H_{r*n}) + E_{f*n} \tag{2.4}$$

where n is the number of muscle pairs, r is the number of frequency components (i.e., the rank of the matrix), f is the frequency, H and W contains coherence patterns and edge weights of the muscle networks, respectively; ultimately, E is the residual error matrix of the NNMF. The variance accounted for (VAF) with a threshold of 90% is exploited to minimize the number of patterns explaining the total variance of the IMC. VAF has been calculated considering the Frobenius norms of both the error and coherence matrices.

Afterwards, the muscle edge weight matrices are normalized to attain unit vectors for each frequency component. Such arrays are then converted into adjacency matrices by a threshold-based method according to which only weight values that are equal to at least the 30% of their maximum are included.

Functional muscle networks are visualized as a set of nodes, which are related to the muscles, and edges, whose appearance changes according to the value of a single element in the adjacency matrix: low, medium, and high connection strengths are defined for a range of 0%-33%, 34%-66%, and 67%-100% of the maximum of the adjacency matrix; analogously, the higher the value of a single element in the adjacency matrix, the thicker the line connecting nodes in the graph depicting the network topology, and viceversa. Note that each node is characterized by a degree k, which is the number of links connecting that node with other neighbors in the network.

Muscle synergies As for muscle synergies, raw EMG signals are processed by means of a 50 Hz notch-filter band-pass for power line artifact removal, a band-pass filtering (5-500 Hz)

and a full-wave rectification, a low-pass filtering (8 Hz) for deriving the envelope [307], and a normalization by each subject's MVC. Ultimately, a segmentation is exploited to extract the portions of interest by inspecting the object linear position.

Muscle synergies approach exploits the time-domain of EMG measurements, working on data dimensionality reduction to find principal components (i.e. motor primitives). Hence, the NNMF is employed to decompose processed EMG data into two non-negative matrices corresponding to the synergies and the activation patterns [287], similarly to the formula in Eq. 2.4. The number of synergies is computed by means of the variance-accounted-for (VAF) criterion such that the 90% of the variance [308]. Muscle synergies are reordered by similarity [287].

2.3.2.3 Metrics and statistics

Different metrics have been employed to compare the conditions w. Exo and w.o. Exo with the aim of evaluating the potential influence of the exoskeleton on motor patterns during the task execution. At first, the root mean squared (RMS) is computed for each processed time-series EMG signal as a measure of the muscular effort (ME) applied by the subject. More specifically, to cope with inter-subject variability in terms of the temporal occurrence of the fatigue onset, for each task and subject a single common duration between the conditions has been set considering the minimum time between the w. Exo and w.o. Exo conditions. Subsequently, the RMS is calculated considering the whole signal for both the isometric and the load-carrying task.

Secondly, for each task, the similarity between the corresponding muscle synergies in w.o. Exo and w. Exo conditions are computed by means of the Pearson correlation coefficient [309].

Moreover, the RMS of the activation matrix H - namely IMCfreq - is computed for the three frequency bands of interest, which are the α-band (1Hz-10Hz), the β-band (10Hz-30Hz), and the γ-band (30Hz-60Hz), to quantify the activation intensity in the muscular coherence for each task.

Graph theory can be exploited to derive features describing the network topology instead of local connections between single pairs, thus leading to a higher robustness against noise affecting EMG channel [292]. Hence, two network metrics have been extracted for each adjacency matrix. In the one hand, the betweenness centrality (BC) denotes how one node is central within the network, meaning that the higher the value, the more the importance of the node in the communication with other nodes [310]. On the other side, the clustering coefficient (CC) quantifies how the neighbors of one node are neighbors among themselves as

well [310]. Note that the global measure of betweenness centrality and clustering coefficient is determined by averaging the BC and CC of each node, thus achieving a scalar value for each subject, condition, and frequency component. Network metrics have been computed by recurring to the Brain Connectivity Toolbox [310].

Ultimately, a correlation analysis among these metrics has been performed by means of the Pearson correlation coefficient. More in detail, the variation of each metric between the two conditions is computed as the difference between the value in the w. Exo condition and that of the w.o. Exo condition. Subsequently, the correlation between the values of the IMCfreq index, considered in each frequency band, and the values of each network metric (i.e., BC and CC) is computed for each frequency component and task. In addition, the correlation between the inter-subject mean of the RMS and the inter-subject mean of each network metric is computed for each frequency component and task.

A Shapiro-Wilk test with a significance level of $\alpha = 0.05$ is used to check the normality distribution of these indexes. Therefore, the metric values in the w. Exo and w.o. Exo conditions are statistically compared with a non-parametric Wilcoxon signed-rank test for non-normally distributed sets and by means of a paired t-test ($\alpha = 0.05$) for normally distributed ones. All the data analysis has been conducted using MATLAB 2022b and its toolboxes.

2.3.3 Results

2.3.3.1 Task-specific results

The outcomes of muscle network analysis outcomes of the isometric and load-carrying task are respectively reported in Figures 2.12 and 2.13 for both w.o. Exo and w. Exo conditions and both frequency components (C1 and C2).

Isometric task Looking at Figure 2.12a, when the subject performs the static isometric task, the activation function is quite stable in the first component having a high intensity in the 1-8 Hz band and a very low one in frequencies major than 8 Hz, while exhibiting a more variable distribution in the second component, showing a medium intensity from 8 Hz to around 30 Hz; nonetheless, it assumes the highest values in the α-band (1Hz-10Hz) and decreases as the frequency increases in both cases. Moreover, this pattern is the same in both w.o. Exo and w. Exo conditions. Accordingly, no statistically significant differences can be observed between the two conditions in terms of the IMCfreq (Figure 2.12b), except for the

second component in the α-band (1Hz-10Hz) in which this median of the IMCfreq in the w. Exo condition is significantly higher than the one in the w.o. Exo condition with $p < .05$.

For each component, as represented in Figure 2.12a, the network topology in the w. Exo is nearly unchanged compared to the w.o. Exo condition. More specifically, regarding to the first component, the right mDEL strengthens its connections with almost all the other muscles when the task is executed with the exoskeleton. As for the second component, the right mPEC is connected with all the other ones in the w.o. Exo condition, whereas other connections appear for the right uTRA in the w. Exo condition. It has to be noted that, generally, the first component features direct connections between the right and left sides of the body while the second component highlights indirect connections (the mPECs act as bridges between the two sides of the body).

Regarding to the network metric in Figure 2.12d, the CC in the w.o. Exo condition is significantly higher than the one in the w. Exo condition with $p < .01$ for both the right and left uTRA only in the second component. On the other hand, the BC in the w.o. Exo condition is significantly lower than the one in the w. Exo condition only for the left uTRA in the first component. Unexpectedly, no significant differences are exhibited for any of the deltoids. As for the averaged BC (Figure 2.12c) and CC (Figure 2.12d), no statistically significant differences have been found between the two conditions as well. Unlike the BC and CC for each muscle, for both frequency components, the median of the averaged BC in the w. Exo condition is lower than the one in the w.o. Exo condition, whereas the median of the averaged CC in the w. Exo condition is higher than the one in the w.o. Exo condition.

Load-carrying task The activation function and its related RMS distribution in the load-carrying task exhibit similar patterns as in the static isometric task, given the similarity of these two tasks.

The network structure in the w.o. Exo condition is also globally unvaried with respect to the w. Exo condition for each component, as noticeable in Figures 2.13a and 2.12b In fact, compared to the isometric task, almost the same connections in terms of both number and intensity can be noticed for the first component; however, regarding to the second component, the MN of the load-carrying task is slightly different from the one in the isometric one, since the connections in the w. Exo condition, besides the main ones with the right mPEC, are almost equally distributed between the right uTRA and left aDEL.

The BC in the two conditions (Figure 2.13c) does not significantly differ each other for any muscle, whereas the CC in the w. Exo condition significantly lessens the one in the w. Exo condition with $p < .05$ for the left mPEC only in the first component, as it can be

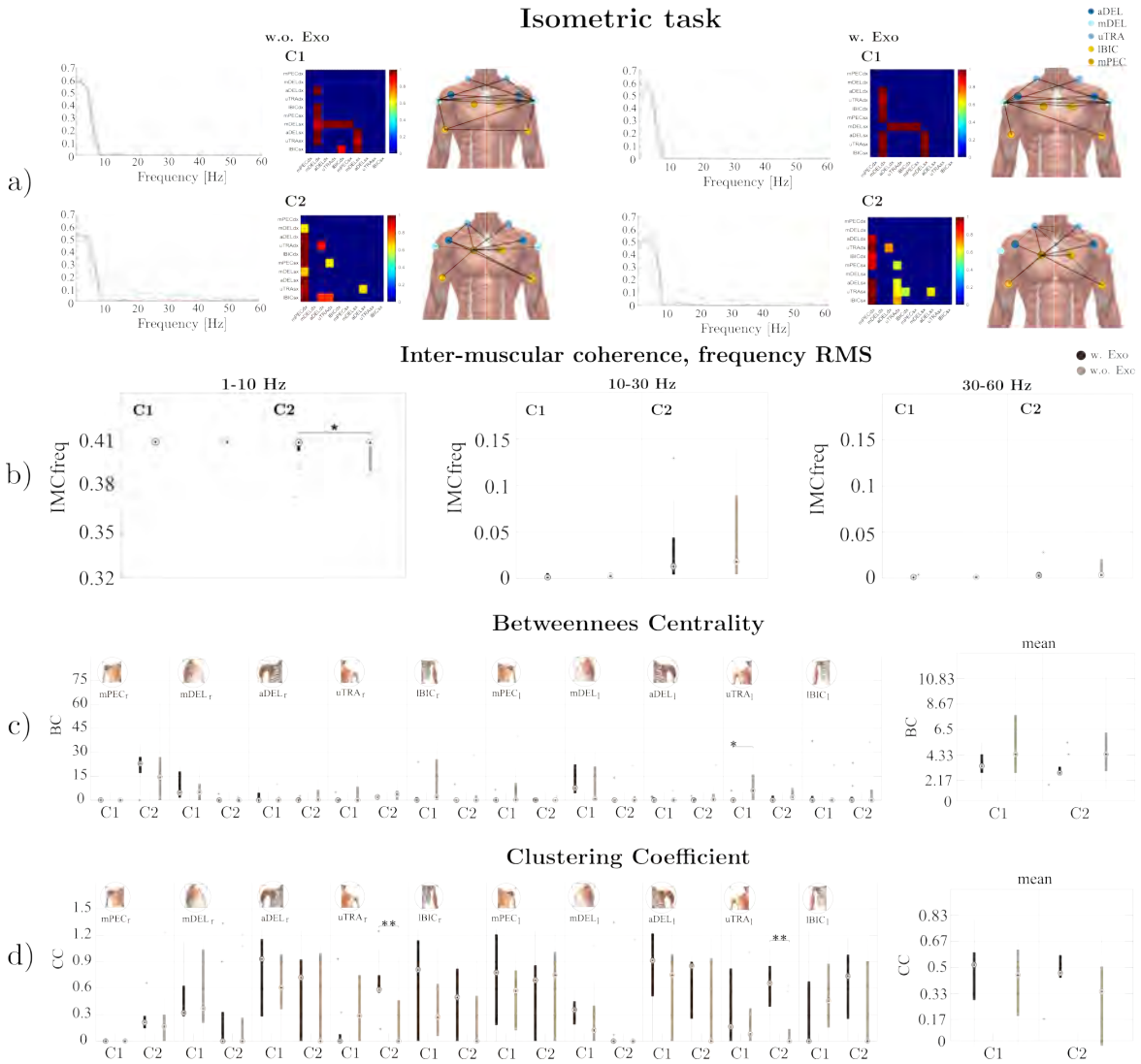

Fig. 2.12 Muscle network analysis outcomes of the isometric task reported for both w.o. Exo and w. Exo conditions and both frequency components (C1 and C2). There can be found: a) the frequency components, the adjacency matrices, and the correspondent muscle networks; b) the RMS of the activation matrix H for the α-band (1Hz-10Hz), the β-band (10Hz-30Hz), and the γ-band (30Hz-60Hz); c) the betweenness centrality (BC) and d) clustering coefficient (CC), which are both computed for each muscle and averaged across muscles.

observed in Figure 2.13d. No statistically significant differences have been found for any deltoids even in this case. The averaged BC (Figure 2.13c) and CC (Figure 2.13d) in the w. Exo condition do not significantly differ from the ones in the w.o. Exo condition. Unlike the BC and CC for each muscle, for both frequency components, the median of the averaged BC in the w. Exo condition lessens the one in the w.o. Exo condition; on the other hand, the

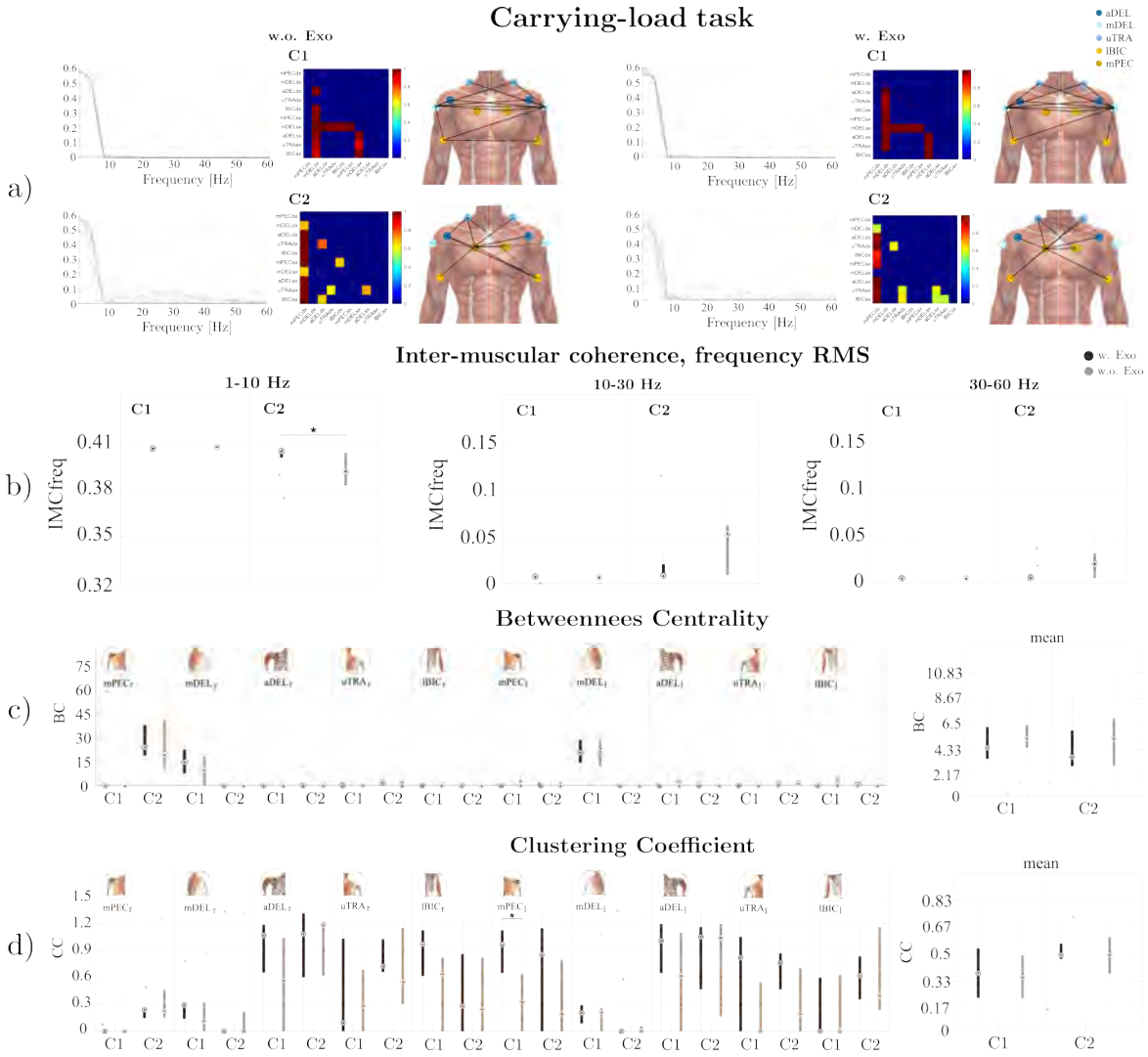

Fig. 2.13 Muscle network analysis outcomes of the load-carrying task reported for both w.o. Exo and w. Exo conditions and both frequency components (C1 and C2). There can be found a) the frequency components, the adjacency matrices, and the correspondent muscle networks; b) the RMS of the activation matrix H for the α-band (1Hz-10Hz), the β-band (10Hz-30Hz), and the γ-band (30Hz-60Hz); c) the betweenness centrality (BC) and d) clustering coefficient (CC), which are both computed for each muscle and averaged across muscles.

median of the averaged CC in the w. Exo condition is either equal or higher than the one in the w.o. Exo condition.

Muscle synergies Muscle synergy analysis is included as a benchmark for the functional connectivity analysis, which is based on muscle networks and proposed as a validation tool for the presented exoskeleton supporting shoulder movements during static and dynamic

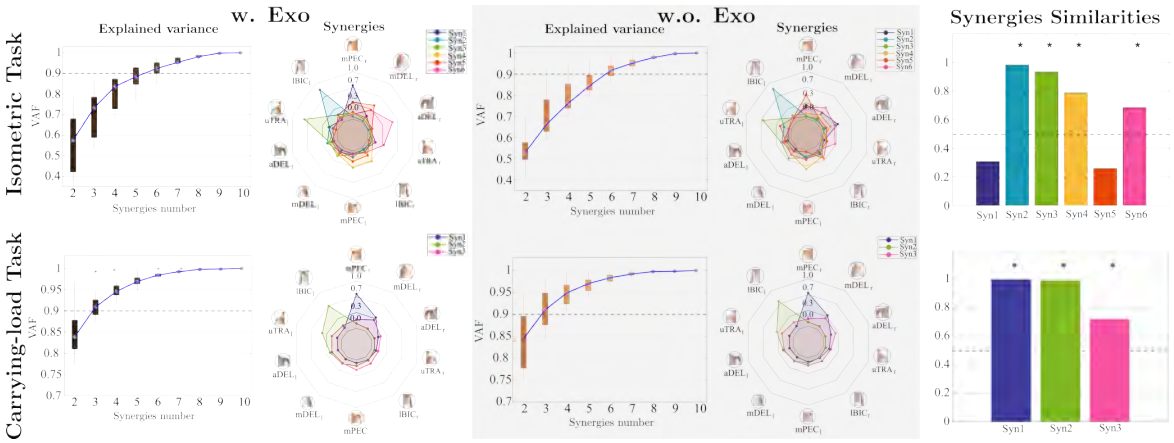

Fig. 2.14 Muscle synergies analysis outcomes of the two motor tasks and for both w.o. Exo and w. Exo conditions. From the left side to the right side of the image there are: the cumulative of the variance explained for each number of synergies; the muscle synergies extracted with the NNMF algorithm; the similarity between the synergies related to the w.o. Exo and w. Exo conditions, where * represents a statistically significant correlation with $p < .05$.

Table 2.5 Mean reduction of the EMG RMS for each muscle.

Task	aDEL	lBIC	mDEL	mPEC	uTRA
Isometric	-29.5	-10.8	-15.3	-27.9	-3.7
Load-carrying	-24.7	-19.1	-31.1	-27.5	-15.8

isometric tasks. Figure 2.14 reports for each task the outcomes of muscle synergy analysis, encompassing the number of synergies computed with the VAF-criterion, the muscle synergies, and their similarity between the corresponding w.o. Exo and w. Exo conditions.

In the isometric task, the minimum number of synergies reconstructing 90% of the signal is 6 in both conditions. Such synergies do not vary noticeably, as proved by the similarity values that are statistically significant for almost all synergies ($p < .05$), except for the first and the fifth synergies. As for the load-carrying task, the minimum number of synergies reconstructing 90% of the signal is 3 in both conditions. All synergies are significantly similar with ($p < .05$).

2.3.3.2 Correlation with muscular activation reductions

Table 2.5 reports the average variation of EMG RMS between the w. Exo and the w.o. Exo conditions for each task. A lower muscular effort has been reached in the former than in the

Table 2.6 Correlation coefficients between the EMG RMS and the network metrics. Statistically significant correlations with $p < .05$ are highlighted in bold.

Network metric	**Isometric task**		**Load-carrying task**	
	First component	Second component	First component	Second component
BC	$R = 0.065$ $p = 0.859$	-0.606 0.063	-0.459 0.182	**0.652** **0.041**
CC	$R = -0.268$ $p = 0.454$	0.434 0.210	0.149 0.682	0.223 0.535

latter condition, as proved by the reductions in muscular activity that range from 15.3% to 29.5% and from 15.8% to 27.5% for the isometric and load-carrying tasks, respectively.

Table 2.6 reports the correlation coefficients between the variation in EMG RMS and the variation in each network metric (i.e., BC and CC) between the w. Exo and the w.o. Exo conditions.

No significant correlation can be observed, except for the difference in EMG RMS and the difference in BC for the second component with $p < .05$ considering the load-carrying task.

Table 2.7 reports the correlation coefficients between the variation in EMG RMS and the variation in the IMCfreq for each frequency band between the w. Exo and the w.o. Exo conditions.

The variation in IMCfreq and the difference in EMG RMS between the w. Exo and w.o. Exo conditions are not significantly correlated with a few exceptions with $p < .05$. With regards to the first component, as for the isometric task, the RMS variation of the right uTRA is positively correlated with the IMCfreq variation in the α-band (1Hz-10Hz), whereas a negative correlation has been found between the RMS variation of the right lBIC and the IMCfreq variation in the β-band (1Hz-10Hz), as well as between the RMS variation of the right mPEC and the IMCfreq variation in the γ-band (30Hz-60Hz). Similarly, as for the load-carrying task, the RMS difference of the right mDEL and the IMCfreq variation in the α-band are negatively correlated; furthermore, the RMS variation of the left mDEL is negatively correlated with the IMCfreq variation in the γ-band. Regarding the second component, only the RMS difference of the left mDEL is negatively correlated with the IMCfreq variation in the α-band.

Table 2.7 Correlation between the EMG RMS and the IMCfreq. Statistically significant correlations with $p < .05$ are highlighted in bold.

Task	**Body side**	**Muscle**	First component			Second component		
			α	β	γ	α	β	γ
Isometric	right	mPEC	$R = -0.438$ $p = 0.238$	0.154 0.693	**−0.714** **0.031**	0.460 0.213	−0.384 0.307	−0.228 0.556
		mDEL	$R = -0.274$ $p = 0.475$	0.057 0.883	−0.228 0.556	−0.212 0.584	0.236 0.541	0.464 0.208
		aDEL	$R = -0.387$ $p = 0.304$	0.239 0.535	−0.073 0.853	−0.060 0.877	0.041 0.917	0.039 0.920
		uTRA	$R = \mathbf{0.716}$ $p = \mathbf{0.030}$	−0.663 0.052	0.242 0.531	0.536 0.136	−0.357 0.345	−0.279 0.467
		lBIC	$R = 0.546$ $p = 0.128$	**−0.681** **0.044**	0.258 0.503	0.192 0.620	0.102 0.794	−0.098 0.802
	left	mPEC	$R = -0.339$ $p = 0.372$	0.218 0.573	−0.568 0.110	0.154 0.693	−0.160 0.682	−0.132 0.735
		mDEL	$R = -0.207$ $p = 0.594$	0.564 0.113	−0.367 0.331	**−0.673** **0.047**	−0.455 0.218	0.657 0.055
		aDEL	$R = 0.041$ $p = 0.916$	0.071 0.857	0.287 0.453	−0.023 0.953	0.018 0.964	0.090 0.817
		uTRA	$R = 0.538$ $p = 0.135$	0.391 0.298	0.377 0.317	0.338 0.374	−0.321 0.399	0.355 0.349
		lBIC	$R = 0.057$ $p = 0.883$	−0.398 0.289	−0.091 0.817	0.171 0.659	0.104 0.791	−0.055 0.888
Load-carrying	right	mPEC	−0.281 0.464	0.469 0.203	−0.257 0.504	−0.599 0.088	−0.030 0.939	0.607 0.083
		mDEL	**−0.670** **0.048**	−0.132 0.735	−0.244 0.526	−0.263 0.493	−0.301 0.432	0.248 0.520
		aDEL	−0.133 0.732	0.140 0.719	−0.220 0.569	0.422 0.258	−0.239 0.535	−0.271 0.481
		uTRA	−0.433 0.244	0.308 0.421	0.395 0.292	−0.505 0.166	0.086 0.826	−0.281 0.464
		lBIC	0.479 0.192	−0.148 0.704	−0.030 0.939	−0.414 0.268	0.404 0.281	0.564 0.114
	left	mPEC	−0.479 0.192	0.098 0.801	−0.031 0.936	−0.391 0.299	0.032 0.935	0.598 0.089
		mDEL	−0.441 0.235	−0.487 0.184	**−0.678** **0.045**	−0.436 0.241	−0.136 0.726	−0.243 0.530
		aDEL	0.011 0.978	−0.158 0.684	−0.382 0.311	−0.101 0.796	0.056 0.886	0.334 0.380
		uTRA	−0.258 0.502	0.460 0.213	0.585 0.098	0.253 0.511	−0.330 0.385	−0.541 0.132
		lBIC	−0.065 0.869	0.109 0.781	0.050 0.898	0.105 0.787	−0.132 0.736	0.129 0.741

2.3.4 Discussions and Conclusions

This work presents the investigation on muscle networks involved during bilateral isometric upper limb tasks with and without an assistive exoskeleton, by means of functional connectivity analysis. For this purpose, functional muscle networks are extracted from the EMG signals of five upper limb muscles (per side) - i.e., biceps brachii (lBIC), anterior deltoid (aDEL), medial deltoid (mDEL), pectoralis major (mPEC), and upper trapezius (uTRA) - to visualize whether and how muscles share the descending neural drives in specific frequencies. Afterwards, a set of metrics is computed to compare the two conditions with (w. Exo) and without the exoskeleton (w.o. Exo). More specifically, the RMS of the processed EMG signal, the RMS of their frequency activations (IMCfreq) in α-, β-, and γ-bands, and the network metrics betweenness centrality (BC) and clustering coefficient (CC) are considered.

In this work, functional muscle network are hypothesized to be a further tool to validate an assistive device, such as a wearable exoskeleton, to evaluate whether physiological motor patterns are retained or varied due to the usage of the device itself. Accordingly, the outcomes reveal that functional connectivity in the w. Exo are mostly unaltered compared to the w.o. Exo condition from many points of view: first, the same number of components has resulted from the NNMF algorithm, and second, the consequent muscle networks reveal consistency between the two conditions in each motor task, having both the network topology and the frequency activations globally the same for each component. An exception to this regards the second component in the α-band, in which case a significant difference between the two conditions has been found for both the isometric and load-carrying tasks; this difference reveals that the frequency RMS when using the exoskeleton is always higher than the one without the exoskeleton, even if the second component differs from the first one mainly in higher frequencies.

Also muscle synergies seem to keep most of their shapes, having 4 similar synergies out of 6 in the isometric task, and 3 similar synergies out of 3 in the load-carrying task. This suggests that the muscle coordination is preserved in terms of the temporal motor pattern. When the box is isometrically held while standing, the biggest differences in synergies have been detected for the right mPEC and aDEL weights; looking at muscle networks, the former is also the muscle with the biggest number of connections, but does not exhibit any differences among conditions. This is in line with muscle effort reductions, which are the highest ones for both mPEC and aDEL (see Table 2.5). Although synergies and networks can give precious insights about muscle coordination strategies, they also show different viewpoints on the same analysis, thus providing complementary information.

This consistency reflects even on the network metric CC, either computed on each muscle or averaged across muscles, given that it does not reveal a statistically significant difference between the w.o. Exo and w. Exo conditions in most of the cases. In the context of muscle networks, the CC of one muscle indicates the extent to which the neighbors of that muscle share the common drive also among themselves [311], thus measuring how one muscle is segregated or aggregated compared to the other ones in the network forming or not a cluster with them, respectively [310]. As a result, the correspondent drives are synchronized such that the neighboring muscles can be recruited to support the aggregated muscle as a compensation measure to accomplish the motor task.

The employment of the exoskeleton has not modified the muscle segregation when an object is isometrically held while either standing or walking. An exception to this global pattern is given by the left pectoral for the first component and the upper trapezii for the second component, in which case the CC in the w. Exo condition is significantly greater than the one in w.o. condition, with $p < .01$. This higher aggregation is in line with the corresponding RMS reduction, which is far lower than that of the anterior deltoid that is targeted by the supporting torque of the exoskeleton. Therefore, this higher aggregation can be arguably explained by the need for synchronizing the other muscles (e.g., left aDEL) to assist the trapezii while statically holding a box.

Conversely, when executing any isometric task with the exoskeleton, both the global values BC and CC in the first component are slightly lower, though not significantly, than the one in the second component. This is in line with other related works, since such global metrics decrease as the frequency increases [287, 293]; nonetheless, such studies did not involve isometric weight-lifting tasks, whence a direct comparison cannot be made.

The difference in BC between the two conditions is positively and significantly correlated with the one in EMG RMS only in the second component for the isometric and load-carrying task, on the trapezius muscles only. From the neural point of view, a central node in one task is the muscle sharing the common drive with other muscles more than the others; since one muscle may belong to the left side and share the drive with muscle on the right side, a high BC makes the former important in the motor coordination in that bilateral task. This means that the more the reduction in muscle effort the more the muscle loses centrality (see Tables 2.7 and 2.5), giving the idea that the coordination pattern slightly changes to accommodate the enter of a "disturb" in the previous physiological pattern. This result is in line with other studies about muscle synergies, whose number and/or patterns tend to change in case of a pathology (e.g., stroke) both with [309] and without an exoskeleton [302]. The reduction of a certain muscle activity may lead to a change of motor strategies, since

that muscle does not join the same previous firing pattern. More investigations are needed to understand whether prolonged utilization of an occupational exoskeleton may lead to a deep re-organization of neural structures, highlighting new possibilities to recover motor capabilities in clinical scenarios, operating on the way in which robots assist human limbs.

In conclusion, functional connectivity analysis has been employed to unveil the impact of an upper-limb exoskeleton on the muscular synchronization during isometric tasks, being together with muscle synergies two faces of the same coin. From the muscle networks point of view, the influence of robotic assistance on muscles seems to reduce their centrality, while muscle synergies reflect this effect on the change of synergies' shape. Hence, despite the limited sample size, investigations based on functional muscle networks are claimed to be a potential additional tool to evaluate the effect of exoskeletons on motor coordination. This overall methodology could help in the future to define new design constraints for assistive devices, thus increasing usability and intuitiveness and, finally, their adoption for the sake of a better quality of life.

Chapter 3

Conclusions

The research works carried out for this thesis were devoted to the conceptualization, development, implementation, and evaluation of innovative interfaces for objective motor assessment in either clinical or industrial fields.

The proposed pipelines have been addressed to different aims, such as the evaluation of visuomotor adaptation, the automatic classification of human motor actions with either a normal or a simulated abnormal execution, and the validation of an occupational exoskeleton supporting human upper-limb joints during static and dynamic lifting tasks.

The studies included in this thesis employed data provided by local institutitions for the sake of the verisimilitude of framework validation.

An in-depth study of the state-of-the-art in the considered domains is presented in Subsections 1.2.1, 1.3.1, 1.4.1, 2.2.1, and 2.3.1, with a focus on visuomotor adaptation, human activty recognition, and occupational exoskeletons.

The proposed system for evaluating visuomotor adaptation is detailed in Section 1.2. Each section describes the state-of-art, materials, methods, and results, after which conclusions are drawn.

The proposed workflows for recognizing human activities of daily living are elucidated in Sections 1.3- 1.4. Each section describes the state-of-art, materials, methods, and results, after which conclusions are drawn. A novel framework for continuous human activity recognition is explained in Section 1.3, whilst Section 1.4 contains a similar workflow addressing the recognition of human locomotor patterns, which are executed either normally or simulating gait disorders. These works validate the proposed systems with data collected on healthy subjects prior to the testing on actual pathological data.

The proposed framework for validating the supportive action of an occupational exoskeleton is detailed in Sections 2.2- 2.3. Each section describes the state-of-art, materials, methods,

and results, after which conclusions are drawn. The traditional validation based on RMS has been compared with other related works in Section 2.2, whereas a novel validation based on functional connectivity analysis is included in Section 2.3.

In conclusion, in this thesis, several technical contributions have been proposed. They include the implementation and preliminary validation on healthy subjects of different innovative interfaces for motor assessment; for this purpose, data were visualized and statistically compared among the different conditions. Most of works oriented to VMA assessment have encompassed upper-limb reaching or drawing tasks and utilized a cursor as visual feedback for the user; instead, a more motivating framework has been implemented with the aid of serious game with the aim of addressing the evaluation of VMA capabilities in children during a locomotion task. This paves the way for the assessment of pathologies determining motor or cognitive impairments, such as the alteration of the sense of agency in children with cerebral palsy.

In the context of human activity recognition, only a few studies employed DL-based workflows that are tested on inertial data coming from a uninterrupted execution of the motor actions and they cannot be easily applied outdoor due to the usage of radar sensors; whereas a novel framework for continuous HAR is proposed by training the DL-based classifier with inertial data correspondent to stand-alone activities before testing it on the signals related to a continuous sequence of the same activities. Furthermore, a new strategy for the recognition of simulated gait disorders is proposed as well, thus adding a contribution to the studies oriented to pathological gait recognition with DL-based models fed by inertial data. Hence, new strategies have been proposed for the DL-based recognition of activities of daily living and simulated gait disorders.

Most studies designing upper-limb exoskeletons for workers have assessed the device in laboratory by means of static tasks, except for a few works entailing dynamic tasks but executed with the support of passive exoskeletons. Moreover, such occupational exoskeletons are typically evaluated with traditional electromyographic measures, whilst almost no previous works have employed inter-muscular functional connectivity as an additional validation tool. On the other hand, an active occupational exoskeleton has been validated with both such conventional metrics and an innovative analysis based on muscle network, thus verifying the influence of a robotic device supporting upper-limb motion during the execution of either isometric or dynamic tasks that resemble an industrial scenario.

In the future, such data-driven approaches for the assessment of either cognitive or motor capabilities are hoped to be increasingly exploited in the clinical practice, as well as for the validation of exoskeleton assisting humans in industrial-like tasks.

My Publications

1. E. Sibilano, **V. Suglia**, A. Brunetti, D. Buongiorno, N. Caporusso, C. Guger, V. Bevilacqua. *Brain-Computer Interfaces*. In: Valeriani, M., de Tommaso, M. (eds) Psychophysiology Methods. Neuromethods, vol 206. Humana, New York, NY.

2. **V. Suglia**, A. Brunetti, G. Pasquini, M. Caputo, T. M. Marvulli, E. Sibilano, S. della Bella, P. Carrozza, C. Beni, D. Naso, V. Monaco, G. Cristella, V. Bevilacqua, D. Buongiorno. *A serious game for the assessment of visuomotor adaptation capabilities during locomotion tasks employing an embodied avatar in virtual reality*. Sensors. 2023; 23(11), 5017.

3. **V. Suglia**, L. Palazzo, V. Bevilacqua, A. Passantino, G. Pagano, G. D'Addio. *A Novel Framework Based on Deep Learning Architecture for Continuous Human Activity Recognition with Inertial Sensors*. Sensors. 2024; 24(7),2199.

4. L. Palazzo, **V. Suglia**, S. Grieco, D. Buongiorno, A. Brunetti, G. Pagano, G. D'Addio, V. Bevilacqua. *A Deep-Learning based framework oriented to pathological gait recognition with inertial sensors*. WIRN 2024, 32nd Italian Workshop on Neural Networks, June 5-7, 2024, Vietri sul Mare, Salerno, Italy, 2024.

5. L. Palazzo, **V. Suglia**, S. Grieco, D. Buongiorno, A. Brunetti, L. Carnimeo, G. Pagano, G. D'Addio, V. Bevilacqua. *A Deep Learning-based framework oriented to pathological gait recognition with inertial sensors*. Sensors 2024; 25(1), 260.

6. F. Berloco, P.M. Marvulli, **V. Suglia**, S. Colucci, G. Pagano, L. Palazzo, M. Aliani, G. Castellana, P. Guido, G. D'Addio, V. Bevilacqua. *Enhancing Survival Analysis Model Selection through XAI(t) in Healthcare*. Applied Sciences. 2024; 14(14),6084.

7. G. Rinaldi, **V. Suglia**, L. Tiseni, C. Camardella, M. Xiloyannis, L. Masia, D. Buongiorno, V Bevilacqua, A. Frisoli, D. Chiaradia. *Towards a healthier workplace: how*

Flexos, an active and bilateral shoulder exoskeleton, provides support in weight-lifting and carrying tasks. *Submitted to* IEEE Transactions on Robotics, 2024.

8. **V. Suglia**, C. Camardella, G. Rinaldi, D. Chiaradia, D. Buongiorno, H. Zhou, A. Frisoli, D. Leonardis, V Bevilacqua. *Muscle networks analysis on an active occupational shoulder exoskeleton*. *Submitted to* IEEE Transactions on Human-Machine Systems, 2024.

9. L. Palazzo, **V. Suglia**, G. Pagano, A. Passantino, G. D'Addio, V. Bevilacqua. *A Deep Learning approach based on a Convolutional Neural Networks architecture towards Abnormal Human Activity Recognition*. XXIV Congresso Nazionale SIAMOC 2024, October 2-5, 2024, Stresa, Italy, 2024.

References

[1] Farshad Falahati, Jonatan Gustavsson, and Grégoria Kalpouzos. Automated segmentation of midbrain nuclei using deep learning and multisequence mri: A longitudinal study on iron accumulation with age. *Imaging Neuroscience*, 2:1–20, Oct 2024. ISSN 2837-6056. doi: 10.1162/imag_a_00304. URL https://doi.org/10.1162/imag_a_00304.

[2] Fernando Trincado-Alonso, Iris Dimbwadyo-Terrer, Ana de los Reyes-Guzmán, Patricia López-Monteagudo, Alberto Bernal-Sahún, and Ángel Gil-Agudo. Kinematic metrics based on the virtual reality system toyra as an assessment of the upper limb rehabilitation in people with spinal cord injury. *BioMed Research International*, 2014:904985, Apr 2014. ISSN 2314-6133. doi: 10.1155/2014/904985.

[3] Thomas D Parsons, Arvind Iyer, Louise Cosand, Christopher G Courtney, and Albert A Rizzo. Neurocognitive and psychophysiological analysis of human performance within virtual reality environments. In *MMVR*, pages 247–252, 2009.

[4] Tongyue He, Junxin Chen, Xu Xu, Giancarlo Fortino, and Wei Wang. Early detection of parkinson's disease using deep neuroenhancenet with smartphone walking recordings. *IEEE Transactions on Neural Systems and Rehabilitation Engineering*, 32:3603–3614, 2024. doi: 10.1109/TNSRE.2024.3462392.

[5] Marco Sica, Salvatore Tedesco, Colum Crowe, Lorna Kenny, Kevin Moore, Suzanne Timmons, John Barton, Brendan O'Flynn, and Dimitrios-Sokratis Komaris. Continuous home monitoring of parkinson's disease using inertial sensors: A systematic review. *PLOS ONE*, 16(2):1–22, 02 2021. doi: 10.1371/journal.pone.0246528. URL https://doi.org/10.1371/journal.pone.0246528.

[6] Adriano Ferrari. From movement to action: a new framework for cerebral palsy. *European journal of physical and rehabilitation medicine*, 55(6):852—861, December 2019. ISSN 1973-9087. doi: 10.23736/s1973-9087.19.05845-3. URL https://doi.org/10.23736/S1973-9087.19.05845-3.

[7] Patrick Haggard. Sense of agency in the human brain. *Nature Reviews Neuroscience*, 18(4):196–207, Apr 2017. ISSN 1471-0048. doi: 10.1038/nrn.2017.14. URL https://doi.org/10.1038/nrn.2017.14.

[8] Giovanna Cristella, Martina Allighieri, Guido Pasquini, Laura Simoni, Antonella Antonetti, Chiara Beni, Claudio Macchi, and Adriano Ferrari. Evaluation of sense of

position and agency in children with diplegic cerebral palsy: A pilot study. *Journal of Pediatric Rehabilitation Medicine*, 15:181–191, 2022. ISSN 1875-8894. doi: 10.3233/PRM-200703. 1.

[9] Anina Ritterband-Rosenbaum, Mark S. Christensen, Mette Kliim-Due, Line Z. Petersen, Betina Rasmussen, and Jens B. Nielsen. Altered sense of agency in children with spastic cerebral palsy. *BMC Neurology*, 11(1):150, Nov 2011. ISSN 1471-2377. doi: 10.1186/1471-2377-11-150. URL https://doi.org/10.1186/1471-2377-11-150.

[10] Vladimiro Suglia, Lucia Palazzo, Vitoantonio Bevilacqua, Andrea Passantino, Gaetano Pagano, and Giovanni D'Addio. A novel framework based on deep learning architecture for continuous human activity recognition with inertial sensors. *Sensors*, 24(7), 2024. ISSN 1424-8220. doi: 10.3390/s24072199. URL https://www.mdpi.com/1424-8220/24/7/2199.

[11] Michela Prunella, Roberto Maria Scardigno, Domenico Buongiorno, Antonio Brunetti, Nicola Longo, Raffaele Carli, Mariagrazia Dotoli, and Vitoantonio Bevilacqua. Deep learning for automatic vision-based recognition of industrial surface defects: A survey. *IEEE Access*, 11:43370–43423, 2023. doi: 10.1109/ACCESS.2023.3271748.

[12] Vladimiro Suglia, Antonio Brunetti, Guido Pasquini, Mariapia Caputo, Tommaso Maria Marvulli, Elena Sibilano, Sara Della Bella, Paola Carrozza, Chiara Beni, David Naso, Vito Monaco, Giovanna Cristella, Vitoantonio Bevilacqua, and Domenico Buongiorno. A serious game for the assessment of visuomotor adaptation capabilities during locomotion tasks employing an embodied avatar in virtual reality. *Sensors*, 23(11), 2023. ISSN 1424-8220. URL https://www.mdpi.com/1424-8220/23/11/5017.

[13] Vladimiro Suglia, Lucia Palazzo, Sabrina Grieco, Domenico Buongiorno, Antonio Brunetti, Leonarda Carnimeo, Gaetano Pagano, Giovanni D'Addio, and Vitoantonio Bevilacqua. A deep learning-based framework oriented to pathological gait recognition with inertial sensors. *Sensors*, 25(1), 2024. doi: 10.3390/s25010260.

[14] Sylvie Abeele and Otmar Bock. Mechanisms for sensorimotor adaptation to rotated visual input. *Experimental Brain Research*, 139(2):248–253, Jul 2001. ISSN 1432-1106. doi: 10.1007/s002210100768.

[15] Jennifer A. Semrau, Joel S. Perlmutter, and Kurt A. Thoroughman. Visuomotor adaptation in parkinson's disease: effects of perturbation type and medication state. *J Neurophysiol*, 111:2675–2687, 2014. doi: 10.1152/jn.00095.2013.

[16] Antonios I. Christou, R. Chris Miall, Fiona McNab, and Joseph M. Galea. Individual differences in explicit and implicit visuomotor learning and working memory capacity. *Scientific Reports*, 6(1):36633, Nov 2016. ISSN 2045-2322. doi: 10.1038/srep36633.

[17] Anna Sadnicka, Anna Stevenson, Kailash P. Bhatia, John C. Rothwell, Mark J. Edwards, and Joseph M. Galea. High motor variability in dyt1 dystonia is associated with impaired

visuomotor adaptation. *Scientific Reports*, 8, 12 2018. ISSN 20452322. doi: 10.1038/s41598-018-21545-0.

[18] Sydney Y. Schaefer, Kathleen Y. Haaland, and Robert L. Sainburg. Dissociation of initial trajectory and final position errors during visuomotor adaptation following unilateral stroke. *Brain Research*, 1298:78–91, 2009. ISSN 0006-8993. doi: https://doi.org/10.1016/j.brainres.2009.08.063.

[19] Muhammad Nabeel Anwar, Muhammad Samran Navid, Mushtaq Khan, and Keiichi Kitajo. A possible correlation between performance iq, visuomotor adaptation ability and mu suppression. *Brain Research*, 1603:84–93, 2015. ISSN 0006-8993. doi: https://doi.org/10.1016/j.brainres.2015.01.045.

[20] Na Li, Guopeng Chen, Yong Xie, and Zhongting Chen. Aging effect on visuomotor adaptation: Mediated by cognitive decline. *Frontiers in Aging Neuroscience*, 13, 2021. doi: 10.3389/fnagi.2021.742928.

[21] Gerd Schmitz. Interference between adaptation to double steps and adaptation to rotated feedback in spite of differences in directional selectivity. *Experimental Brain Research*, 234(6):1491–1504, Jun 2016. ISSN 1432-1106. doi: 10.1007/s00221-016-4559-y.

[22] Gerd Schmitz. Enhanced cognitive performance after multiple adaptations to visuomotor transformations. *PLOS ONE*, 17(9):1–19, 09 2022. doi: 10.1371/journal.pone.0274759.

[23] Jenny Lin, Yixin Zhu, James Kubricht, Song-Chun Zhu, and Hongjing Lu. Visuomotor adaptation and sensory recalibration in reversed hand movement task. In *CogSci*, 2017.

[24] O.A. Kannape, L. Schwabe, T. Tadi, and O. Blanke. The limits of agency in walking humans. *Neuropsychologia*, 48(6):1628–1636, 2010. ISSN 0028-3932. doi: https://doi.org/10.1016/j.neuropsychologia.2010.02.005.

[25] Oliver Alan Kannape, Arnaud Barré, Kamiar Aminian, and Olaf Blanke. Cognitive loading affects motor awareness and movement kinematics but not locomotor trajectories during goal-directed walking in a virtual reality environment. *PLOS ONE*, 9(1):1–11, 01 2014. doi: 10.1371/journal.pone.0085560.

[26] Simin Zhu, Ronny Gerhard Guendel, Alexander Yarovoy, and Francesco Fioranelli. Continuous human activity recognition with distributed radar sensor networks and cnn–rnn architectures. *IEEE Transactions on Geoscience and Remote Sensing*, 60:1–15, 2022. URL https://www.doi.org/10.1109/TGRS.2022.3189746.

[27] Ruchita Mehta, Sara Sharifzadeh, Vasile Palade, Bo Tan, Alireza Daneshkhah, and Yordanka Karayaneva. Deep learning techniques for radar-based continuous human activity recognition. *Machine Learning and Knowledge Extraction*, 5(4):1493–1518, 2023. ISSN 2504-4990. doi: 10.3390/make5040075. URL https://www.mdpi.com/2504-4990/5/4/75.

[28] Ronny G. Guendel, Francesco Fioranelli, and Alexander Yarovoy. Distributed radar fusion and recurrent networks for classification of continuous human activities. *IET Radar, Sonar & Navigation*, 16(7):1144–1161, 2022. URL https://doi.org/10.1049/rsn2.12249.

[29] Ingrid Ullmann, Ronny G. Guendel, Nicolas Christian Kruse, Francesco Fioranelli, and Alexander Yarovoy. Radar-based continuous human activity recognition with multi-label classification. In *2023 IEEE SENSORS*, pages 1–4, 2023. doi: 10.1109/SENSORS56945.2023.10324957.

[30] Ismael Espinoza Jaramillo, Jin Gyun Jeong, Patricio Rivera Lopez, Choong Ho Lee, Do Yeon Kang, Tae Jun Ha, Ji Heon Oh, Hwanseok Jung, Jin Hyuk Lee, Won Hee Lee, and Tae Seong Kim. Real-Time Human Activity Recognition with IMU and Encoder Sensors in Wearable Exoskeleton Robot via Deep Learning Networks. *Sensors*, 22(24), 2022. ISSN 14248220. doi: 10.3390/s22249690.

[31] Diego Robles, Mouna Benchekroun, Andrea Lira, Carla Taramasco, Vincent Zalc, Igor Irazzoky, and Dan Istrate. Real-time gait pattern classification using artificial neural networks. *2022 IEEE International Workshop on Metrology for Living Environment, MetroLivEn 2022 - Proceedings*, pages 76–80, 2022. doi: 10.1109/MetroLivEnv54405.2022.9826927.

[32] Mostafa Ghobadi and Ehsan Tarkesh Esfahani. A robust automatic gait monitoring approach using a single imu for home-based applications. *Journal of Mechanics in Medicine and Biology*, 17, 08 2017. doi: 10.1142/S0219519417500774.

[33] Shubao Yin, Chen Chen, Hangyu Zhu, Xinping Wang, and Wei Chen. Neural networks for pathological gait classification using wearable motion sensors. *2019 IEEE Biomedical Circuits and Systems Conference (BioCAS)*, pages 1–4, 2019.

[34] The effects of brain lateralization on motor control and adaptation. *Journal of Motor Behavior*, 44(6):455–469, 2012. ISSN 00222895. doi: 10.1080/00222895.2012.747482.

[35] Carole Ferrel, Chantal Bard, and Michelle Fleury. Coordination in childhood: modifications of visuomotor representations in 6- to 11-year-old children. *Experimental Brain Research*, 138(3):313–321, Jun 2001. ISSN 1432-1106. doi: 10.1007/s002210100697.

[36] Carole Ferrel-Chapus, Laurette Hay, Isabelle Olivier, Chantal Bard, and Michelle Fleury. Visuomanual coordination in childhood: adaptation to visual distortion. *Experimental Brain Research*, 144(4):506–517, Jun 2002. ISSN 1432-1106. doi: 10.1007/s00221-002-1064-2.

[37] José L. Contreras-Vidal, Jin Bo, J. Paul Boudreau, and Jane E. Clark. Development of visuomotor representations for hand movement in young children. *Experimental Brain Research*, 162(2):155–164, Apr 2005. ISSN 1432-1106. doi: 10.1007/s00221-004-2123-7.

[38] Sylvie Abeele and Otmar Bock. Sensorimotor adaptation to rotated visual input: different mechanisms for small versus large rotations. *Experimental Brain Research*, 140(4):407–410, Oct 2001. ISSN 1432-1106. doi: 10.1007/s002210100846.

[39] Jessica L. Allen and Jason R. Franz. The motor repertoire of older adult fallers may constrain their response to balance perturbations. *Journal of Neurophysiology*, 120(5): 2368–2378, 2018. doi: 10.1152/jn.00302.2018.

[40] Jason R Franz, Carrie A Francis, Matthew S Allen, and Darryl G Thelen. Visuomotor entrainment and the frequency-dependent response of walking balance to perturbations. *IEEE transactions on neural systems and rehabilitation engineering*, 25(8):1135–1142, 2016. doi: 10.1109/TNSRE.2016.2603340.

[41] Jessica D. Thompson and Jason R. Franz. Do kinematic metrics of walking balance adapt to perturbed optical flow? *Human Movement Science*, 54:34–40, 2017. ISSN 0167-9457. doi: https://doi.org/10.1016/j.humov.2017.03.004.

[42] John W. Krakauer, Zachary M. Pine, Maria-Felice Ghilardi, and Claude Ghez. "learning of visuomotor transformations for vectorial planning of reaching trajectories": Correction. *The Journal of Neuroscience*, 21:1–1, 2001.

[43] Pietro Mazzoni and John W. Krakauer. An implicit plan overrides an explicit strategy during visuomotor adaptation. *Journal of Neuroscience*, 26(14):3642–3645, apr 2006. ISSN 02706474. doi: 10.1523/JNEUROSCI.5317-05.2006.

[44] Jordan A. Taylor, John W. Krakauer, and Richard B. Ivry. Explicit and implicit contributions to learning in a sensorimotor adaptation task. *Journal of Neuroscience*, 34 (8):3023–3032, 2014. ISSN 02706474. doi: 10.1523/JNEUROSCI.3619-13.2014.

[45] Adrian M. Haith, David M. Huberdeau, and John W. Krakauer. The influence of movement preparation time on the expression of visuomotor learning and savings. *Journal of Neuroscience*, 35(13):5109–5117, apr 2015. ISSN 15292401. doi: 10.1523/JNEUROSCI.3869-14.2015.

[46] Hamid F. Bagce, Soha Saleh, Sergei V. Adamovich, John W. Krakauer, and Eugene Tunik. Corticospinal excitability is enhanced after visuomotor adaptation and depends on learning rather than performance or error. *Journal of Neurophysiology*, 109(4): 1097–1106, feb 2013. ISSN 00223077. doi: 10.1152/jn.00304.2012.

[47] David M. Huberdeau, Adrian M. Haith, and John W. Krakauer. Formation of a long-term memory for visuomotor adaptation following only a few trials of practice. *Journal of Neurophysiology*, 114(2):969–977, jun 2015. ISSN 15221598. doi: 10.1152/jn.00369.2015.

[48] David M. Huberdeau, John W. Krakauer, and Adrian M. Haith. Practice induces a qualitative change in the memory representation for visuomotor learning. *Journal of Neurophysiology*, 122(3):1050–1059, 2019. ISSN 15221598. doi: 10.1152/JN.00830.2018/ASSET/IMAGES/LARGE/Z9K0091952080003.JPEG.

[49] Xing Xing and Jeffrey A. Saunders. Different generalization of fast and slow visuomotor adaptation across locomotion and pointing tasks. *Experimental Brain Research*, 239(9): 2859–2871, Sep 2021. ISSN 1432-1106. doi: 10.1007/s00221-021-06112-w.

[50] Joaquin A. Anguera, Patricia A. Reuter-Lorenz, Daniel T. Willingham, and Rachael D. Seidler. Contributions of Spatial Working Memory to Visuomotor Learning. *Journal of Cognitive Neuroscience*, 22(9):1917–1930, 09 2010. ISSN 0898-929X. doi: 10.1162/jocn.2009.21351.

[51] Heiko Lex, Matthias Weigelt, Andreas Knoblauch, and Thomas Schack. Functional relationship between cognitive representations of movement directions and visuomotor adaptation performance. *Experimental Brain Research*, 223(4):457–467, Dec 2012. ISSN 1432-1106. doi: 10.1007/s00221-012-3273-7.

[52] Heiko Lex, Matthias Weigelt, Andreas Knoblauch, and Thomas Schack. The functional role of cognitive frameworks on visuomotor adaptation performance. *Journal of Motor Behavior*, 46(6):389–396, 2014. doi: 10.1080/00222895.2014.920290.

[53] Gerd Schmitz, Mirco Dierking, and Anthea Guenther. Correlations between executive functions and adaptation to incrementally increasing sensorimotor discordances. *Experimental Brain Research*, 236(12):3417–3426, Dec 2018. ISSN 1432-1106. doi: 10.1007/s00221-018-5388-y.

[54] Muyinat Y. Osaba, Dario Martelli, Antonio Prado, Sunil K. Agrawal, and Anil K. Lalwani. Age-related differences in gait adaptations during overground walking with and without visual perturbations using a virtual reality headset. *Scientific Reports*, 10(1): 15376, Sep 2020. ISSN 2045-2322. doi: 10.1038/s41598-020-72408-6.

[55] Otmar Bock. Components of sensorimotor adaptation in young and elderly subjects. *Experimental Brain Research*, 160(2):259–263, Jan 2005. ISSN 1432-1106. doi: 10.1007/s00221-004-2133-5.

[56] Joaquin A. Anguera, Patricia A. Reuter-Lorenz, Daniel T. Willingham, and Rachael D. Seidler. Failure to engage spatial working memory contributes to age-related declines in visuomotor learning. *Journal of Cognitive Neuroscience*, 23(1):11–25, Jan 2011. ISSN 0898-929X. doi: 10.1162/jocn.2010.21451.

[57] Otmar Bock and Michaela Girgenrath. Relationship between sensorimotor adaptation and cognitive functions in younger and older subjects. *Experimental Brain Research*, 169(3):400–406, Mar 2006. ISSN 1432-1106. doi: 10.1007/s00221-005-0153-4.

[58] Anja Simon and Otmar Bock. Influence of divergent and convergent thinking on visuomotor adaptation in young and older adults. *Human Movement Science*, 46:23–29, 2016. ISSN 0167-9457. doi: https://doi.org/10.1016/j.humov.2015.11.020.

[59] Aaron L. Wong, Cherie L. Marvel, Jordan A. Taylor, and John W. Krakauer. Can patients with cerebellar disease switch learning mechanisms to reduce their adaptation deficits? *Brain*, 142(3):662–673, mar 2019. ISSN 0006-8950. doi: 10.1093/BRAIN/AWY334.

[60] Chimei M. Lee and Jin Bo. Visuomotor adaptation and its relationship with motor ability in children with and without autism spectrum disorder. *Human Movement Science*, 78:102826, 2021. ISSN 0167-9457. doi: https://doi.org/10.1016/j.humov.2021.102826.

[61] F.A. Kagerer, J.L. Contreras-Vidal, J. Bo, and J.E. Clark. Abrupt, but not gradual visuomotor distortion facilitates adaptation in children with developmental coordination disorder. *Human Movement Science*, 25(4):622–633, 2006. ISSN 0167-9457. doi: https://doi.org/10.1016/j.humov.2006.06.003. Advances in Graphonomics: Studies on Fine Motor Control, Its Development and Disorders.

[62] José L. Contreras-Vidal and Ethan R. Buch. Effects of parkinson's disease on visuomotor adaptation. *Experimental Brain Research*, 150(1):25–32, May 2003. ISSN 1432-1106. doi: 10.1007/s00221-003-1403-y.

[63] Erin K. Cressman, Danielle Salomonczyk, Alina Constantin, Janis Miyasaki, Elena Moro, Robert Chen, Antonio Strafella, Susan Fox, Anthony E. Lang, Howard Poizner, and Denise Y.P. Henriques. Proprioceptive recalibration following implicit visuomotor adaptation is preserved in parkinson's disease. *Experimental Brain Research*, 239: 1551–1565, 5 2021. ISSN 14321106. doi: 10.1007/s00221-021-06075-y.

[64] Carine Nguemeni, Luis Nakchbandi, György Homola, and Daniel Zeller. Impaired consolidation of visuomotor adaptation in patients with multiple sclerosis. *European Journal of Neurology*, 28(3):884–892, 2021. doi: 10.1111/ene.14599.

[65] Laura B. F. Kurdziel, Katherine Dempsey, Mackenzie Zahara, Eve Valera, and Rebecca M. C. Spencer. Impaired visuomotor adaptation in adults with adhd. *Experimental Brain Research*, 233(4):1145–1153, Apr 2015. ISSN 1432-1106. doi: 10.1007/s00221-014-4190-8.

[66] Laura Bindel, Christoph Mühlberg, Victoria Pfeiffer, Matthias Nitschke, Annekatrin Müller, Mirko Wegscheider, Jost Julian Rumpf, Kirsten E. Zeuner, Jos S. Becktepe, Julius Welzel, Miriam Güthe, Joseph Classen, and Elinor Tzvi. Visuomotor adaptation deficits in patients with essential tremor. *Cerebellum*, 2022. ISSN 14734230. doi: 10.1007/s12311-022-01474-5.

[67] Reza Shadmehr, Maurice A. Smith, and John W. Krakauer. Error correction, sensory prediction, and adaptation in motor control. *https://doi.org/10.1146/annurev-neuro-060909-153135*, 33:89–108, jun 2010. ISSN 0147006X. doi: 10.1146/ANNUREV-NEURO-060909-153135.

[68] Denise J. Berger, Reinhard Gentner, Timothy Edmunds, Dinesh K. Pai, and Andrea d'Avella. Differences in adaptation rates after virtual surgeries provide direct evidence for modularity. *Journal of Neuroscience*, 33(30):12384–12394, 2013. ISSN 0270-6474. doi: 10.1523/JNEUROSCI.0122-13.2013.

[69] Omar Janeh, Eike Langbehn, Frank Steinicke, Gerd Bruder, Alessandro Gulberti, and Monika Poetter-Nerger. Walking in virtual reality: Effects of manipulated visual self-motion on walking biomechanics. *ACM Transactions on Applied Perception (TAP)*, 14 (2):1–15, 2017. doi: 10.1145/3022731.

[70] Dario Martelli, Boxi Xia, Antonio Prado, and Sunil K. Agrawal. Gait adaptations during overground walking and multidirectional oscillations of the visual field in a virtual reality headset. *Gait & Posture*, 67:251–256, 2019. ISSN 0966-6362. doi: 10.1016/j.gaitpost.2018.10.029.

[71] Domenico Buongiorno, Francesco Barone, Massimiliano Solazzi, Vitoantonio Bevilacqua, and Antonio Frisoli. A linear optimization procedure for an emg-driven neuromusculoskeletal model parameters adjusting: Validation through a myoelectric exoskeleton control. In Fernando Bello, Hiroyuki Kajimoto, and Yon Visell, editors, *Haptics: Perception, Devices, Control, and Applications*, pages 218–227, Cham, 2016. Springer International Publishing. ISBN 978-3-319-42324-1. doi: 10.1007/978-3-319-42324-1_22.

[72] Domenico Buongiorno, Francesco Barone, Denise J. Berger, Benedetta Cesqui, Vitoantonio Bevilacqua, Andrea d'Avella, and Antonio Frisoli. Evaluation of a pose-shared synergy-based isometric model for hand force estimation: Towards myocontrol. In Jaime Ibáñez, José González-Vargas, José María Azorín, Metin Akay, and José Luis Pons, editors, *Converging Clinical and Engineering Research on Neurorehabilitation II*, pages 953–958, Cham, 2017. Springer International Publishing. ISBN 978-3-319-46669-9. doi: 10.1007/978-3-319-46669-9_154.

[73] Domenico Buongiorno, Cristian Camardella, Giacomo Donato Cascarano, Luis Pelaez Murciego, Michele Barsotti, Irio De Feudis, Antonio Frisoli, and Vitoantonio Bevilacqua. An undercomplete autoencoder to extract muscle synergies for motor intention detection. In *2019 International Joint Conference on Neural Networks (IJCNN)*, pages 1–8, 2019. doi: 10.1109/IJCNN.2019.8851975.

[74] David W. Franklin, Etienne Burdet, Keng Peng Tee, Rieko Osu, Chee-Meng Chew, Theodore E. Milner, and Mitsuo Kawato. Cns learns stable, accurate, and efficient movements using a simple algorithm. *Journal of Neuroscience*, 28(44):11165–11173, 2008. ISSN 0270-6474. doi: 10.1523/JNEUROSCI.3099-08.2008.

[75] Domenico Buongiorno, Giacomo Donato Cascarano, Cristian Camardella, Irio De Feudis, Antonio Frisoli, and Vitoantonio Bevilacqua. Task-oriented muscle synergy extraction using an autoencoder-based neural model. *Information*, 11(4), 2020. ISSN 2078-2489. doi: 10.3390/info11040219.

[76] Cristian Camardella, Michele Barsotti, Domenico Buongiorno, Antonio Frisoli, and Vitoantonio Bevilacqua. Towards online myoelectric control based on muscle synergies-to-force mapping for robotic applications. *Neurocomputing*, 452:768–778, 2021. ISSN 0925-2312. doi: 10.1016/j.neucom.2020.08.081.

[77] Pierre Baraduc and Daniel M. Wolpert. Adaptation to a visuomotor shift depends on the starting posture. *Journal of Neurophysiology*, 88(2):973–981, 2002. doi: 10.1152/jn.2002.88.2.973.

[78] Mathias Hegele and Herbert Heuer. Adaptation to a direction-dependent visuomotor gain in the young and elderly. *Psychological Research PRPF*, 74(1):21, Dec 2008. ISSN 1430-2772. doi: 10.1007/s00426-008-0221-z.

[79] Jeanne Langan and Rachael D Seidler. Age differences in spatial working memory contributions to visuomotor adaptation and transfer. *Behavioural brain research*, 225(1): 160–168, 2011. doi: 10.1016/j.bbr.2011.07.014.

[80] Benjamin Michaud, Yosra Cherni, Mickael Begon, Geneviève Girardin-Vignola, and Patrick Roussel. A serious game for gait rehabilitation with the lokomat. In *2017 International Conference on Virtual Rehabilitation (ICVR)*, pages 1–2. IEEE, 2017. doi: 10.1109/ICVR.2017.8007482.

[81] Rob Labruyère, Corinna N Gerber, Karin Birrer-Brütsch, Andreas Meyer-Heim, and Hubertus JA van Hedel. Requirements for and impact of a serious game for neuropediatric robot-assisted gait training. *Research in developmental disabilities*, 34(11): 3906–3915, 2013. doi: 10.1016/j.ridd.2013.07.031.

[82] Jingjing Zhang, Mengjie Huang, Lixiang Zhao, Rui Yang, Hai-Ning Liang, Ji Han, Liu Wang, and Wenxin Sun. Influence of hand representation design on presence and embodiment in virtual environment. In *2020 13th International Symposium on Computational Intelligence and Design (ISCID)*, pages 364–367. IEEE, 2020. doi: 10.1109/ISCID51228.2020.00088.

[83] Guilherme Gonçalves, Miguel Melo, Luís Barbosa, José Vasconcelos-Raposo, and Maximino Bessa. Evaluation of the impact of different levels of self-representation and body tracking on the sense of presence and embodiment in immersive vr. *Virtual Reality*, 26(1):1–14, Mar 2022. ISSN 1434-9957. doi: 10.1007/s10055-021-00530-5.

[84] Azure Kinect DK hardware specifications. Available online: https://learn.microsoft.com/it-it/azure/kinect-dk/hardware-specification, .

[85] Vito Modesto Manghisi, Antonio Emmanuele Uva, Michele Fiorentino, Vitoantonio Bevilacqua, Gianpaolo Francesco Trotta, and Giuseppe Monno. Real time rula assessment using kinect v2 sensor. *Applied Ergonomics*, 65:481–491, 2017. ISSN 0003-6870. doi: 10.1016/j.apergo.2017.02.015.

[86] Antonio Brunetti, Domenico Buongiorno, Gianpaolo Francesco Trotta, and Vitoantonio Bevilacqua. Computer vision and deep learning techniques for pedestrian detection and tracking: A survey. *Neurocomputing*, 300:17–33, 2018. ISSN 0925-2312. doi: https://doi.org/10.1016/j.neucom.2018.01.092.

[87] Domenico Buongiorno, Gianpaolo Francesco Trotta, Ilaria Bortone, Nicola Di Gioia, Felice Avitto, Giacomo Losavio, and Vitoantonio Bevilacqua. Assessment and rating of movement impairment in parkinson's disease using a low-cost vision-based system. In De-Shuang Huang, M. Michael Gromiha, Kyungsook Han, and Abir Hussain, editors, *Intelligent Computing Methodologies*, pages 777–788, Cham, 2018. Springer International Publishing. ISBN 978-3-319-95957-3. doi: 10.1007/978-3-319-95957-3_82.

[88] Ilaria Bortone, Domenico Buongiorno, Giuseppina Lelli, Andrea Di Candia, Giacomo Donato Cascarano, Gianpaolo Francesco Trotta, Pietro Fiore, and Vitoantonio Bevilacqua. Gait analysis and parkinson's disease: Recent trends on main applications in healthcare. In Lorenzo Masia, Silvestro Micera, Metin Akay, and José L. Pons, editors, *Converging Clinical and Engineering Research on Neurorehabilitation III*, pages 1121–1125, Cham, 2019. Springer International Publishing. ISBN 978-3-030-01845-0. doi: 10.1007/978-3-030-01845-0_224.

[89] Azure-Kinect-Samples. Available online: https://github.com/microsoft/Azure-Kinect-Samples/tree/master/body-tracking-samples/sample_unity_bodytracking, .

[90] Yongshi Wang, Lei Gao, Hongjiao Yan, Zhaohui Jin, Jinping Fang, Lin Qi, Qiaoxia Zhen, Cui Liu, Ping Wang, Yonghong Liu, Ruidan Wang, Yanjun Liu, Yuan Su, Aixian Liu, and Boyan Fang. Efficacy of c-mill gait training for improving walking adaptability in early and middle stages of parkinson's disease. *Gait and Posture*, 91(October 2021): 79–85, 2022. ISSN 18792219. doi: 10.1016/j.gaitpost.2021.10.010.

[91] Determination of preferred walking speed on treadmill may lead to high oxygen cost on treadmill walking. *Gait and Posture*, 31(3):366–369, 2010. ISSN 09666362. doi: 10.1016/j.gaitpost.2010.01.006.

[92] ArUco: a minimal library for Augmented Reality applications based on OpenCV. Available online: https://www.uco.es/investiga/grupos/ava/portfolio/aruco/.

[93] Marley W. Watkins. Structure of the wechsler intelligence scale for children—fourth edition among a national sample of referred students. *Psychological Assessment*, 22: 782–787, 2010. doi: 10.1037/a0020043.

[94] John L. Davis and Robb N. Matthews. Nepsy-ii review: Korkman, m., kirk, u., & kemp, s. (2007). nepsy—second edition (nepsy-ii). san antonio, tx: Harcourt assessment. *Journal of Psychoeducational Assessment*, 28(2):175–182, 2010. doi: 10.1177/0734282909346716.

[95] Carmelo Ardito, Danilo Caivano, Lucio Colizzi, Giovanni Dimauro, and Loredana Verardi. Design and execution of integrated clinical pathway: A simplified meta-model and associated methodology. *Information*, 11(7), 2020. ISSN 2078-2489. doi: 10.3390/info11070362.

[96] Shafaq Irshad, Andrew Perkis, and Waleed Azam. Wayfinding in virtual reality serious game: An exploratory study in the context of user perceived experiences. *Applied Sciences (Switzerland)*, 11(17), 2021. ISSN 20763417. doi: 10.3390/app11177822.

[97] Stylianos Mystakidis, Jeries Besharat, George Papantzikos, Athanasios Christopoulos, Chrysostomos Stylios, Spiros Agorgianitis, and Dimitrios Tselentis. Design, development, and evaluation of a virtual reality serious game for school fire preparedness training. *Education Sciences*, 12(4), 2022. ISSN 22277102. doi: 10.3390/educsci12040281.

[98] Sardar Mehboob Hussain, Antonio Brunetti, Giuseppe Lucarelli, Riccardo Memeo, Vitoantonio Bevilacqua, and Domenico Buongiorno. Deep learning based image processing for robot assisted surgery: A systematic literature survey. *IEEE Access*, 10(September): 122627–122657, 2022. ISSN 21693536. doi: 10.1109/ACCESS.2022.3223704.

[99] Randi Q. Mao, Lucy Lan, Jeffrey Kay, Ryan Lohre, Olufemi R. Ayeni, Danny P. Goel, and Darren de SA. Immersive virtual reality for surgical training: A systematic review. *Journal of Surgical Research*, 268(December):40–58, 2021. ISSN 10958673. doi: 10.1016/j.jss.2021.06.045.

[100] Carla Winter, Florian Kern, Dominik Gall, Marc Erich Latoschik, Paul Pauli, and Ivo Käthner. Immersive virtual reality during gait rehabilitation increases walking speed and motivation: a usability evaluation with healthy participants and patients with multiple sclerosis and stroke. *Journal of NeuroEngineering and Rehabilitation*, 18(1):1–14, 2021. ISSN 17430003. doi: 10.1186/s12984-021-00848-w.

[101] Stephen R. Serge and Gino Fragomeni. Assessing the relationship between type of head movement and simulator sickness using an immersive virtual reality head mounted display: A pilot study. In Stephanie Lackey and Jessie Chen, editors, *Virtual, Augmented and Mixed Reality*, pages 556–566, Cham, 2017. Springer International Publishing. ISBN 978-3-319-57987-0. doi: 10.1007/978-3-319-57987-0_45.

[102] Maxime T. Robert, Laurent Ballaz, and Martin Lemay. The effect of viewing a virtual environment through a head-mounted display on balance. *Gait & Posture*, 48:261–266, 2016. ISSN 0966-6362. doi: https://doi.org/10.1016/j.gaitpost.2016.06.010.

[103] Kenta Kamikokuryo, Takumi Haga, Gentiane Venture, and Vincent Hernandez. Adversarial autoencoder and multi-armed bandit for dynamic difficulty adjustment in immersive virtual reality for rehabilitation: Application to hand movement. *Sensors*, 22(12), 2022. ISSN 14248220. doi: 10.3390/s22124499.

[104] Eduardo Casilari, Moisés Álvarez Marco, and Francisco García-Lagos. A study of the use of gyroscope measurements in wearable fall detection systems. *Symmetry*, 12(4), 2020. ISSN 2073-8994. URL https://www.doi.org.com/10.3390/sym12040649.

[105] Abbas Shah Syed, Daniel Sierra-Sosa, Anup Kumar, and Adel Elmaghraby. A Deep Convolutional Neural Network-XGB for Direction and Severity Aware Fall Detection

and Activity Recognition. *Sensors*, 22(7):1–22, 2022. ISSN 14248220. doi: 10.3390/s22072547.

[106] Thomas A. Buckley, Chris Pitsikoulis, and Chris J. Hass. Dynamic postural stability during sit-to-walk transitions in parkinson disease patients. *Movement Disorders*, 23(9): 1274–1280, 2008. URL https://doi.org/10.1002/mds.22079.

[107] Natacha Oliveira, Filipe Carvalho, Jorge Laíns, Deolinda Rasteiro, and Luis Roseiro. Development of a biomechanical device for parameter quantification associated with the sit-to-stand movement. *Sensors*, 23(4), 2023. ISSN 1424-8220. doi: 10.3390/s23041837.

[108] Yan Wang, Shuang Cang, and Hongnian Yu. A survey on wearable sensor modality centred human activity recognition in health care. *Expert Systems with Applications*, 137:167–190, 2019. ISSN 0957-4174. URL https://www.doi.org/j.eswa.2019.04.057.

[109] A. Moncada-Torres, K. Leuenberger, R. Gonzenbach, A. Luft, and R. Gassert. Activity classification based on inertial and barometric pressure sensors at different anatomical locations. *Physiological Measurement*, 35(7):1245–1263, 2014. ISSN 13616579. doi: 10.1088/0967-3334/35/7/1245.

[110] Jaeyoung Yang, Joonwhan Lee, and Joongmin Choi. Activity recognition based on rfid object usage for smart mobile devices. *Journal of Computer Science and Technology*, 26(2):239–246, Mar 2011. ISSN 1860-4749. URL https://doi.org/10.1007/s11390-011-9430-9.

[111] Rene Grzeszick, Jan Marius Lenk, Fernando Moya Rueda, Gernot A. Fink, Sascha Feldhorst, and Michael Ten Hompel. Deep neural network based human activity recognition for the order picking process. *ACM International Conference Proceeding Series*, Part F1319, 2017. doi: 10.1145/3134230.3134231.

[112] Georgios Sopidis, Michael Haslgrübler, and Alois Ferscha. Counting activities using weakly labeled raw acceleration data: A variable-length sequence approach with deep learning to maintain event duration flexibility. *Sensors*, 23(11), 2023. ISSN 1424-8220. URL https://www.doi.org/10.3390/s23115057.

[113] Bonhak Koo, Ngoc Tram Nguyen, and Jooyong Kim. Identification and classification of human body exercises on smart textile bands by combining decision tree and convolutional neural networks. *Sensors*, 23(13), 2023. ISSN 1424-8220. URL https://www.doi.com/10.3390/s23136223.

[114] Christopher Moufawad el Achkar, Constanze Lenoble-Hoskovec, Anisoara Paraschiv-Ionescu, Kristof Major, Christophe Büla, and Kamiar Aminian. Instrumented shoes for activity classification in the elderly. *Gait & posture*, 44:12–17, 2016. URL https://doi.org/10.1016/j.gaitpost.2015.10.016.

[115] Hung Nguyen, Karina Lebel, Patrick Boissy, Sarah Bogard, Etienne Goubault, and Christian Duval. Auto detection and segmentation of daily living activities during a

Timed Up and Go task in people with Parkinson's disease using multiple inertial sensors. *Journal of NeuroEngineering and Rehabilitation*, 14(1):1–13, 2017. ISSN 17430003. doi: 10.1186/s12984-017-0241-2.

[116] Katia Turcot, Stéphane Armand, Daniel Fritschy, Pierre Hoffmeyer, and Domizio Suvà. Sit-to-stand alterations in advanced knee osteoarthritis. *Gait and Posture*, 36(1): 68–72, 2012. ISSN 09666362. doi: 10.1016/j.gaitpost.2012.01.005.

[117] Daniele Riboni, Gabriele Civitarese, and Claudio Bettini. Analysis of long-term abnormal behaviors for early detection of cognitive decline. *2016 IEEE International Conference on Pervasive Computing and Communication Workshops, PerCom Workshops 2016*, pages 1–6, 2016. doi: 10.1109/PERCOMW.2016.7457139.

[118] Jay-shian Tan, Behrouz Khabbaz Beheshti, Tara Binnie, Paul Davey, J P Caneiro, Peter Kent, Anne Smith, Peter O Sullivan, and Amity Campbell. Human Activity Recognition for People with Knee Osteoarthritis. *Sensors*, 21(3381):1–16, 2021. URL https://doi.org/10.3390/s21103381.

[119] Ong Chin Ann and Lau Bee Theng. Human activity recognition: A review. In *2014 IEEE international conference on control system, computing and engineering (ICCSCE 2014)*, pages 389–393. IEEE, 2014. URL https://www.doi.org/10.1109/ICCSCE.2014.7072750.

[120] Yunus Celik, M. Fatih Aslan, Kadir Sabanci, Sam Stuart, Wai Lok Woo, and Alan Godfrey. Improving Inertial Sensor-Based Activity Recognition in Neurological Populations. *Sensors*, 22(24), 2022. ISSN 14248220. doi: 10.3390/s22249891.

[121] Zhaozong Meng, Mingxing Zhang, Changxin Guo, Qirui Fan, Hao Zhang, Nan Gao, and Zonghua Zhang. Recent progress in sensing and computing techniques for human activity recognition and motion analysis. *Electronics*, 9(9), 2020. ISSN 2079-9292. URL https://www.doi.org/10.3390/electronics9091357.

[122] Giovanni Paragliola and Antonio Coronato. Intelligent monitoring of stereotyped motion disorders in case of children with autism. In *2013 9th International Conference on Intelligent Environments*, pages 258–261, 2013. doi: 10.1109/IE.2013.12.

[123] Shusuke Okita, Roman Yakunin, Jathin Korrapati, Mina Ibrahim, Diogo Schwerz de Lucena, Vicky Chan, and David J. Reinkensmeyer. Counting Finger and Wrist Movements Using Only a Wrist-Worn, Inertial Measurement Unit: Toward Practical Wearable Sensing for Hand-Related Healthcare Applications. *Sensors*, 23(12):5690, 2023. ISSN 14248220. doi: 10.3390/s23125690.

[124] Muhammad Shoaib, Hans Scholten, and P. J.M. Havinga. Towards physical activity recognition using smartphone sensors. *Proceedings - IEEE 10th International Conference on Ubiquitous Intelligence and Computing, UIC 2013 and IEEE 10th International Conference on Autonomic and Trusted Computing, ATC 2013*, pages 80–87, 2013. doi: 10.1109/UIC-ATC.2013.43.

[125] Sakorn Mekruksavanich, Ponnipa Jantawong, and Anuchit Jitpattanakul. A Deep Learning-based Model for Human Activity Recognition using Biosensors embedded into a Smart Knee Bandage. *Procedia Computer Science*, 214(C):621–627, 2022. ISSN 18770509. doi: 10.1016/j.procs.2022.11.220. URL https://doi.org/10.1016/j.procs.2022.11.220.

[126] Valentina Bianchi, Marco Bassoli, Gianfranco Lombardo, Paolo Fornacciari, Monica Mordonini, and Ilaria De Munari. IoT Wearable Sensor and Deep Learning: An Integrated Approach for Personalized Human Activity Recognition in a Smart Home Environment. *IEEE Internet of Things Journal*, 6(5):8553–8562, 2019. ISSN 23274662. doi: 10.1109/JIOT.2019.2920283.

[127] Kerem Altun, Billur Barshan, and Orkun Tunçel. Comparative study on classifying human activities with miniature inertial and magnetic sensors. *Pattern Recognition*, 43 (10):3605–3620, 2010. ISSN 00313203. doi: 10.1016/j.patcog.2010.04.019.

[128] Fabio Bagala, Jochen Klenk, Angelo Cappello, Lorenzo Chiari, Clemens Becker, and Ulrich Lindemann. Quantitative description of the lie-to-sit-to-stand-to-walk transfer by a single body-fixed sensor. *IEEE Transactions on Neural Systems and Rehabilitation Engineering*, 21(4):624–633, 2013. ISSN 15344320. doi: 10.1109/TNSRE.2012.2230189.

[129] Oresti Banos, Claudia Villalonga, Rafael Garcia, Alejandro Saez, Miguel Damas, Juan A. Holgado-Terriza, Sungyong Lee, Hector Pomares, and Ignacio Rojas. Design, implementation and validation of a novel open framework for agile development of mobile health applications. *BioMedical Engineering Online*, 14(2):1–20, 2015. ISSN 1475925X. doi: 10.1186/1475-925X-14-S2-S6.

[130] Fernando Moya Rueda, René Grzeszick, Gernot A. Fink, Sascha Feldhorst, and Michael Ten Hompel. Convolutional neural networks for human activity recognition using body-worn sensors. *Informatics*, 5(2):1–17, 2018. ISSN 22279709. doi: 10.3390/informatics5020026.

[131] Marjan Gholamrezaii and Smt AlModarresi. A time-efficient convolutional neural network model in human activity recognition. *Multimedia Tools and Applications*, 80 (13):19361–19376, 2021. ISSN 15737721. doi: 10.1007/s11042-020-10435-1.

[132] Giuseppe De Leonardis, Samanta Rosati, Gabriella Balestra, Valentina Agostini, Elisa Panero, Laura Gastaldi, and Marco Knaflitz. Human activity recognition by wearable sensors: Comparison of different classifiers for real-time applications. In *2018 IEEE international symposium on medical measurements and applications (memea)*, pages 1–6. IEEE, 2018. URL https://www.doi.org/10.1109/MeMeA.2018.8438750.

[133] Walid Gomaa and Mohamed A Khamis. A perspective on human activity recognition from inertial motion data. *Neural Computing and Applications*, 35(28):20463–20568, 2023. URL https://doi.org/10.1007/s00521-023-08863-9.

[134] Eliasz Kańtoch and Piotr Augustyniak. Human activity surveillance based on wearable body sensor network. In *2012 computing in cardiology*, pages 325–328. IEEE, 2012.

[135] Kaixuan Chen, Dalin Zhang, Lina Yao, Bin Guo, Zhiwen Yu, and Yunhao Liu. Deep learning for sensor-based human activity recognition: Overview, challenges, and opportunities. *ACM Computing Surveys (CSUR)*, 54(4):1–40, 2021. URL https://doi.org/10.1145/3447744.

[136] Domenico Buongiorno, Giacomo Donato Cascarano, Irio De Feudis, Antonio Brunetti, Leonarda Carnimeo, Giovanni Dimauro, and Vitoantonio Bevilacqua. Deep learning for processing electromyographic signals: A taxonomy-based survey. *Neurocomputing*, 452: 549–565, 2021. ISSN 0925-2312. doi: https://doi.org/10.1016/j.neucom.2020.06.139. URL https://www.sciencedirect.com/science/article/pii/S0925231220319020.

[137] Kieran Woodward, Eiman Kanjo, Kyle Taylor, and John A. Hunt. A multi-sensor deep learning approach for complex daily living activity recognition. *DigiBiom 2022 - Proceedings of the 2022 Emerging Devices for Digital Biomarkers*, pages 13–17, 2022. doi: 10.1145/3539494.3542753.

[138] Lina Tong, Hanghang Ma, Qianzhi Lin, Jiaji He, and Liang Peng. A Novel Deep Learning Bi-GRU-I Model for Real-Time Human Activity Recognition Using Inertial Sensors. *IEEE Sensors Journal*, 22(6):6164–6174, 2022. ISSN 15581748. URL https://www.doi.org/10.1109/JSEN.2022.3148431.

[139] Vincent Xeno Rahn, Lin Zhou, Eric Klieme, and Bert Arnrich. Optimal sensor placement for human activity recognition with a minimal smartphone-imu setup. In *SENSORNETS*, pages 37–48, 2021.

[140] Ankit Vijayvargiya, Khimraj, Rajesh Kumar, and Nilanjan Dey. Voting-based 1d cnn model for human lower limb activity recognition using semg signal. *Physical and Engineering Sciences in Medicine*, 44(4):1297–1309, Dec 2021. ISSN 2662-4737. doi: 10.1007/s13246-021-01071-6.

[141] L Minh Dang, Kyungbok Min, Hanxiang Wang, Md Jalil Piran, Cheol Hee Lee, and Hyeonjoon Moon. Sensor-based and vision-based human activity recognition: A comprehensive survey. *Pattern Recognition*, 108:107561, 2020. URL https://doi.org/10.1016/j.patcog.2020.107561.

[142] R. Anto Arockia Rosaline, Ponnuviji N.P., Subbu Lakshmi T.C., and Manisha G. Enhancing lifestyle and health monitoring of elderly populations using CSA-TkELM classifier. *Knowledge-Based Systems*, 276:110758, 2023. ISSN 09507051. doi: 10.1016/j.knosys.2023.110758. URL https://doi.org/10.1016/j.knosys.2023.110758.

[143] Milagros Jaén-Vargas, Karla Miriam Reyes Leiva, Francisco Fernandes, Sérgio Barroso Goncalves, Miguel Tavares Silva, Daniel Simões Lopes, and José Javier Serrano Olmedo. Effects of sliding window variation in the performance of acceleration-based

human activity recognition using deep learning models. *PeerJ Computer Science*, 8: 1–22, 2022. ISSN 23765992. doi: 10.7717/PEERJ-CS.1052.

[144] A. Nouriani, R. McGovern, and R. Rajamani. Activity recognition using a combination of high gain observer and deep learning computer vision algorithms. *Intelligent Systems with Applications*, 18(January):200213, 2023. ISSN 26673053. doi: 10.1016/j.iswa.2023.200213. URL https://doi.org/10.1016/j.iswa.2023.200213.

[145] Mark Nutter, Catherine H. Crawford, and Jorge Ortiz. Design of Novel Deep Learning Models for Real-time Human Activity Recognition with Mobile Phones. *Proceedings of the International Joint Conference on Neural Networks*, 2018-July:1–8, 2018. doi: 10.1109/IJCNN.2018.8489319.

[146] Nguyen Thi Hoai Thu and Dong Seog Han. An Investigation on Deep Learning-Based Activity Recognition Using IMUs and Stretch Sensors. *4th International Conference on Artificial Intelligence in Information and Communication, ICAIIC 2022 - Proceedings*, pages 377–382, 2022. doi: 10.1109/ICAIIC54071.2022.9722621.

[147] Domenico Buongiorno, Michela Prunella, Stefano Grossi, Sardar Mehboob Hussain, Alessandro Rennola, Nicola Longo, Giovanni Di Stefano, Vitoantonio Bevilacqua, and Antonio Brunetti. Inline defective laser weld identification by processing thermal image sequences with machine and deep learning techniques. *Applied Sciences*, 12(13), 2022. ISSN 2076-3417. doi: 10.3390/app12136455. URL https://www.mdpi.com/2076-3417/12/13/6455.

[148] Daniela Micucci, Marco Mobilio, and Paolo Napoletano. Unimib shar: A dataset for human activity recognition using acceleration data from smartphones. *Applied Sciences*, 7(10):1101, 2017.

[149] Gaetano Pagano, Leandro Donisi, Vito Marsico, Ernesto Losavio, Mario Cesarelli, and Giovanni D'Addio. Reliability of kinematic parameters related to the timed up and go test in patients with gait impairments. In *2021 IEEE International Symposium on Medical Measurements and Applications (MeMeA)*, pages 1–5, 2021. doi: 10.1109/MeMeA52024.2021.9478762.

[150] Seungeun Chung, Jiyoun Lim, Kyoung Ju Noh, Gague Kim, and Hyuntae Jeong. Sensor data acquisition and multimodal sensor fusion for human activity recognition using deep learning. *Sensors (Switzerland)*, 19(7), 2019. ISSN 14248220. doi: 10.3390/s19071716.

[151] Domenico Chiaradia, Luca Tiseni, Michele Xiloyannis, Massimiliano Solazzi, Lorenzo Masia, and Antonio Frisoli. An assistive soft wrist exosuit for flexion movements with an ergonomic reinforced glove. *Frontiers in Robotics and AI*, 7, 2021. ISSN 2296-9144. URL https://www.doi.org/10.3389/frobt.2020.595862.

[152] Gianluca Rinaldi, Luca Tiseni, Michele Xiloyannis, Lorenzo Masia, Antonio Frisoli, and Domenico Chiaradia. Flexos: A portable, sea-based shoulder exoskeleton with

hyper-redundant kinematics for weight lifting assistance. In *2023 IEEE World Haptics Conference (WHC)*, pages 252–258, 2023. doi: 10.1109/WHC56415.2023.10224485.

[153] Jeremy Kulchyk and Ali Etemad. Activity Recognition with Wearable Accelerometers using Deep Convolutional Neural Network and the Effect of Sensor Placement. *Proceedings of IEEE Sensors*, 2019-Octob:1–4, 2019. ISSN 21689229. doi: 10.1109/SENSORS43011.2019.8956668.

[154] Manuel Gil-Martín, Rubén San-Segundo, Fernando Fernández-Martínez, and Javier Ferreiros-López. Time analysis in human activity recognition. *Neural Processing Letters*, 53(6):4507–4525, Dec 2021. ISSN 1573-773X. URL https://doi.org/10.1007/s11063-021-10611-w.

[155] Tianpeng Li, Jiansheng Chen, Chunhua Hu, Yu Ma, Zhiyuan Wu, Weitao Wan, Yiqing Huang, Fuming Jia, Chen Gong, Sen Wan, and Luming Li. Automatic timed up-and-go sub-task segmentation for parkinson's disease patients using video-based activity classification. *IEEE Transactions on Neural Systems and Rehabilitation Engineering*, 26 (11):2189–2199, 2018. URL https://doi.org/10.1109/TNSRE.2018.2875738.

[156] Margaret KY Mak and Christina WY Hui-Chan. Audiovisual cues can enhance sit-to-stand in patients with parkinson's disease. *Movement disorders*, 19(9):1012–1019, 2004. URL https://doi.org/10.1002/mds.20196.

[157] Minh H. Pham, Elke Warmerdam, Morad Elshehabi, Christian Schlenstedt, Lu-Marie Bergeest, Maren Heller, Linda Haertner, Joaquim J. Ferreira, Daniela Berg, Gerhard Schmidt, Clint Hansen, and Walter Maetzler. Validation of a lower back "wearable"-based sit-to-stand and stand-to-sit algorithm for patients with parkinson's disease and older adults in a home-like environment. *Frontiers in Neurology*, 9, 2018. ISSN 1664-2295. URL https://doi.org/10.3389/fneur.2018.00652.

[158] Brian Kenji Iwana and Seiichi Uchida. An empirical survey of data augmentation for time series classification with neural networks. *PLOS ONE*, 16(7):1–32, 07 2021. doi: 10.1371/journal.pone.0254841. URL https://doi.org/10.1371/journal.pone.0254841.

[159] Louis Atallah, Benny Lo, Rachel King, and Guang Zhong Yang. Sensor positioning for activity recognition using wearable accelerometers. *IEEE Transactions on Biomedical Circuits and Systems*, 5(4):320–329, 2011. ISSN 19324545. doi: 10.1109/TBCAS.2011.2160540.

[160] Hazar Zilelioglu, Ghazaleh Khodabandelou, Abdelghani Chibani, and Yacine Amirat. Semisupervised Generative Adversarial Networks With Temporal Convolutions for Human Activity Recognition. *IEEE Sensors Journal*, 23(11):12355–12369, 2023. ISSN 15581748. doi: 10.1109/JSEN.2023.3267243.

[161] Elena Sibilano, Antonio Brunetti, Domenico Buongiorno, Michael Lassi, Antonello Grippo, Valentina Bessi, Silvestro Micera, Alberto Mazzoni, and Vitoantonio Bevilacqua.

An attention-based deep learning approach for the classification of subjective cognitive decline and mild cognitive impairment using resting-state EEG. *Journal of Neural Engineering*, 20(1), 2023. ISSN 17412552. doi: 10.1088/1741-2552/acb96e.

[162] Tanushree Meena and Kishor Sarawadekar. An explainable self-attention-based spatial–temporal analysis for human activity recognition. *IEEE Sensors Journal*, 24(1): 635–644, 2024. URL https://www.doi.org/10.1109/JSEN.2023.3335449.

[163] Mst. Alema Khatun, Mohammad Abu Yousuf, Sabbir Ahmed, Md. Zia Uddin, Salem A. Alyami, Samer Al-Ashhab, Hanan F. Akhdar, Asaduzzaman Khan, Akm Azad, and Mohammad Ali Moni. Deep cnn-lstm with self-attention model for human activity recognition using wearable sensor. *IEEE Journal of Translational Engineering in Health and Medicine*, 10:1–16, 2022. URL https://www.doi.org/10.1109/JTEHM.2022.3177710.

[164] Carlos Betancourt, Wen-Hui Chen, and Chi-Wei Kuan. Self-attention networks for human activity recognition using wearable devices. In *2020 IEEE International Conference on Systems, Man, and Cybernetics (SMC)*, pages 1194–1199, 2020. doi: 10.1109/SMC42975.2020.9283381.

[165] Xiuhua Liu, Zhihao Zhou, and Qining Wang. Real-time onboard human motion recognition based on inertial measurement units. In *2018 IEEE 8th Annual International Conference on CYBER Technology in Automation, Control, and Intelligent Systems (CYBER)*, pages 724–728, 2018. doi: 10.1109/CYBER.2018.8688093.

[166] Jun-Ji Lin, Che-Kang Hsu, Wei-Li Hsu, Tsu-Chin Tsao, Fu-Cheng Wang, and Jia-Yush Yen. Machine learning for human motion intention detection. *Sensors*, 23(16), 2023. ISSN 1424-8220. doi: https://www.doi.org/10.3390/s23167203.

[167] Yifan Liu, Xing Liu, Zhongyan Wang, Xu Yang, and Xingjun Wang. Improving performance of human action intent recognition: Analysis of gait recognition machine learning algorithms and optimal combination with inertial measurement units. *Computers in Biology and Medicine*, 163:107192, 2023. ISSN 0010-4825. URL https://doi.org/10.1016/j.compbiomed.2023.107192.

[168] Sakorn Mekruksavanich and Anuchit Jitpattanakul. Deep residual network with a cbam mechanism for the recognition of symmetric and asymmetric human activity using wearable sensors. *Symmetry*, 16(5), 2024. ISSN 2073-8994. doi: 10.3390/sym16050554.

[169] Jing Gao, Peishang Gu, Qing Ren, Jinde Zhang, and Xin Song. Abnormal gait recognition algorithm based on lstm-cnn fusion network. *IEEE Access*, 7:163180–163190, 2019. doi: 10.1109/ACCESS.2019.2950254.

[170] Wonjin Kim and Yanggon Kim. Abnormal gait recognition based on integrated gait features in machine learning. In *2021 IEEE 45th Annual Computers, Software, and Applications Conference (COMPSAC)*, pages 1683–1688, 2021. doi: 10.1109/COMPSAC51774.2021.00251.

[171] Yao Guo, Fani Deligianni, Xiao Gu, and Guang-Zhong Yang. 3d canonical pose estimation and abnormal gait recognition with a single rgb-d camera. *IEEE Robotics and Automation Letters*, PP:1–1, 07 2019. doi: 10.1109/LRA.2019.2928775.

[172] Yi Chiew Han, Kiing Wong, and Iain Murray. Comparison of machine learning methods for the construction of a standalone gait diagnosis device. *IET Signal Processing*, 14, 06 2020. doi: 10.1049/iet-spr.2019.0228.

[173] Youngmin Oh, Sol A. Choi, Yumi Shin, Yeonwoo Jeong, Jongkuk Lim, and Sujin Kim. Investigating activity recognition for hemiparetic stroke patients using wearable sensors: A deep learning approach with data augmentation. *Sensors*, 24, 2024. ISSN 14248220. doi: 10.3390/s24010210.

[174] Thanaporn Jinnovart, Xiongcai Cai, and Kundjanasith Thonglek. Abnormal gait recognition in real-time using recurrent neural networks. In *2020 59th IEEE Conference on Decision and Control (CDC)*, pages 972–977, 2020. doi: 10.1109/CDC42340.2020.9304106.

[175] Mohammad Iman Mokhlespour Esfahani and Maury Nussbaum. Using smart garments to differentiate among normal and simulated abnormal gaits. *Journal of Biomechanics*, 93, 06 2019. doi: 10.1016/j.jbiomech.2019.06.009.

[176] Marianna Amboni, Carlo Ricciardi, Sarah Adamo, Emanuele Nicolai, Antonio Volzone, Roberto Erro, Sofia Cuoco, Giuseppe Cesarelli, Luca Basso, Giovanni D'Addio, Marco Salvatore, Leonardo Pace, and Paolo Barone. Machine learning can predict mild cognitive impairment in parkinson's disease. *Frontiers in Neurology*, 13, 2022. ISSN 16642295. doi: 10.3389/fneur.2022.1010147.

[177] Claudio Loconsole, Giacomo Donato Cascarano, Antonio Lattarulo, Antonio Brunetti, Gianpaolo Francesco Trotta, Domenico Buongiorno, Ilaria Bortone, Irio De Feudis, Giacomo Losavio, Vitoantonio Bevilacqua, and Eugenio Di Sciascio. A comparison between ann and svm classifiers for parkinson's disease by using a model-free computer-assisted handwriting analysis based on biometric signals. In *2018 International Joint Conference on Neural Networks (IJCNN)*, pages 1–8, 2018. doi: 10.1109/IJCNN.2018.8489293.

[178] Giacomo Donato Cascarano, Antonio Brunetti, Domenico Buongiorno, Gianpaolo Francesco Trotta, Claudio Loconsole, Ilaria Bortone, and Vitoantonio Bevilacqua. *A Multi-modal Tool Suite for Parkinson's Disease Evaluation and Grading*, pages 257–268. Springer Singapore, Singapore, 2020. ISBN 978-981-13-8950-4. doi: 10.1007/978-981-13-8950-4_24. URL https://doi.org/10.1007/978-981-13-8950-4_24.

[179] Domenico Buongiorno, Ilaria Bortone, Giacomo Donato Cascarano, Gianpaolo Francesco Trotta, Antonio Brunetti, and Vitoantonio Bevilacqua. A low-cost vision system based on the analysis of motor features for recognition and severity rating of parkinson's disease. *BMC Medical Informatics and Decision Making*, 19

(9):243, Dec 2019. ISSN 1472-6947. doi: 10.1186/s12911-019-0987-5. URL https://doi.org/10.1186/s12911-019-0987-5.

[180] Domenico Buongiorno, Gianpaolo Francesco Trotta, Ilaria Bortone, Nicola Di Gioia, Felice Avitto, Giacomo Losavio, and Vitoantonio Bevilacqua. Assessment and rating of movement impairment in parkinson's disease using a low-cost vision-based system. In De-Shuang Huang, M. Michael Gromiha, Kyungsook Han, and Abir Hussain, editors, *Intelligent Computing Methodologies*, pages 777–788, Cham, 2018. Springer International Publishing. ISBN 978-3-319-95957-3.

[181] Giuseppe Cesarelli, Leandro Donisi, Armando Coccia, Federica Amitrano, Arcangelo Biancardi, Bernardo Lanzillo, and Giovanni D'Addio. Ataxia and parkinson's disease patients classification using tree-based machine learning algorithms fed by spatiotemporal features: a pilot study. *2022 IEEE International Symposium on Medical Measurements and Applications, MeMeA 2022 - Conference Proceedings*, pages 1–6, 2022. doi: 10.1109/MeMeA54994.2022.9856460.

[182] Ho Seok Lee, Hokyoung Ryu, Shi-Uk Lee, Jae-sung Cho, Sungmin You, Jae Hyeon Park, and Seong-Ho Jang. Analysis of gait characteristics using hip-knee cyclograms in patients with hemiplegic stroke. *Sensors*, 21(22), 2021. ISSN 1424-8220. doi: 10.3390/s21227685. URL https://www.mdpi.com/1424-8220/21/22/7685.

[183] Joohwan Sung, Sungmin Han, Heesu Park, Soree Hwang, Song Joo Lee, Jong Woong Park, and Inchan Youn. Classification of stroke severity using clinically relevant symmetric gait features based on recursive feature elimination with cross-validation. *IEEE Access*, 10:119437–119447, 2022. doi: 10.1109/ACCESS.2022.3218118.

[184] Djordje Slijepcevic, Matthias Zeppelzauer, Anna-Maria Gorgas, Caterine Schwab, Michael Schüller, Arnold Baca, Christian Breiteneder, and Brian Horsak. Automatic classification of functional gait disorders. *IEEE Journal of Biomedical and Health Informatics*, 22(5):1653–1661, 2018. doi: 10.1109/JBHI.2017.2785682.

[185] Sasanka Potluri, Srinivas Ravuri, Christian Diedrich, and Lutz Schega. Deep learning based gait abnormality detection using wearable sensor system. In *2019 41st Annual International Conference of the IEEE Engineering in Medicine and Biology Society (EMBC)*, pages 3613–3619, 2019. doi: 10.1109/EMBC.2019.8856454.

[186] Tanmay Tulsidas Verlekar, Pedro Albuquerque, Luís Ducla Soares, and Paulo Lobato Correia. Using transfer learning for classification of gait pathologies. *Proceedings of the IEEE International Conference on Bioinformatics and Biomedicine (BIBM)*, 2018.

[187] Pedro Albuquerque, João Machado, Tanmay Tulsidas Verlekar, Luís Ducla Soares, and Paulo Lobato Correia. Remote pathological gait classification system. *IEEE Journal of Biomedical and Health Informatics*, 11(XX):1894, 2021.

[188] Elham Dolatabadi, Babak Taati, and Alex Mihailidis. An automated classification of pathological gait using unobtrusive sensing technology. *IEEE Transactions on Neural*

Systems and Rehabilitation Engineering, 25(12):2336–2346, 2017. doi: 10.1109/TNSRE.2017.2736939.

[189] Avijoy Chakma, Abu Zaher Md Faridee, Indrajeet Ghosh, and Nirmalya Roy. Domain adaptation for inertial measurement unit-based human activity recognition: A survey, 2023. URL https://arxiv.org/abs/2304.06489.

[190] Valentina Bianchi, Marco Bassoli, Gianfranco Lombardo, Paolo Fornacciari, Monica Mordonini, and Ilaria De Munari. Iot wearable sensor and deep learning: An integrated approach for personalized human activity recognition in a smart home environment. *IEEE Internet of Things Journal*, 6(5):8553–8562, 2019. doi: 10.1109/JIOT.2019.2920283.

[191] Hao Ma and Wei-Hsin Liao. Human gait modeling and analysis using a semi-markov process with ground reaction forces. *IEEE Transactions on Neural Systems and Rehabilitation Engineering*, 25(6):597–607, 2017. doi: 10.1109/TNSRE.2016.2584923.

[192] Santosh Kumar Yadav, Kamlesh Tiwari, Hari Mohan Pandey, and Shaik Ali Akbar. A review of multimodal human activity recognition with special emphasis on classification, applications, challenges and future directions. *Knowledge-Based Systems*, 223:106970, 2021. ISSN 0950-7051. doi: https://doi.org/10.1016/j.knosys.2021.106970. URL https://www.sciencedirect.com/science/article/pii/S0950705121002331.

[193] Ilaria Bortone, Domenico Buongiorno, Giuseppina Lelli, Andrea Di Candia, Giacomo Donato Cascarano, Gianpaolo Francesco Trotta, Pietro Fiore, and Vitoantonio Bevilacqua. Gait analysis and parkinson's disease: Recent trends on main applications in healthcare. In Lorenzo Masia, Silvestro Micera, Metin Akay, and José L. Pons, editors, *Converging Clinical and Engineering Research on Neurorehabilitation III*, pages 1121–1125, Cham, 2019. Springer International Publishing. ISBN 978-3-030-01845-0.

[194] Nastaran Mohammadian Rad, Twan Van Laarhoven, Cesare Furlanello, and Elena Marchiori. Novelty detection using deep normative modeling for imu-based abnormal movement monitoring in parkinson's disease and autism spectrum disorders. *Sensors*, 18 (10), 2018. ISSN 1424-8220. doi: 10.3390/s18103533. URL https://www.mdpi.com/1424-8220/18/10/3533.

[195] K Mohan Iyer. *Clinical examination in orthopedics*. Springer Science & Business Media, 2011.

[196] Susan Sienko Thomas, Carolyn Moore, Claudia Kelp-Lenane, and Carolyn Norris. Simulated gait patterns: The resulting effects on gait parameters, dynamic electromyography, joint moments, and physiological cost index. *Gait and Posture*, 4:100–107, 1996. ISSN 09666362. doi: 10.1016/0966-6362(95)01039-4.

[197] Kooksung Jun, Keunhan Lee, Sanghyub Lee, Hwanho Lee, and Mun Sang Kim. Hybrid deep neural network framework combining skeleton and gait features for pathological gait recognition. *Bioengineering*, 10(10), 2023. ISSN 2306-5354. doi: 10.3390/bioengineering10101133. URL https://www.mdpi.com/2306-5354/10/10/1133.

[198] G. D'Addio, S. Evangelista, L. Donisi, A. Biancardi, E. Andreozzi, G. Pagano, P. Arpaia, and M. Cesarelli. Development of a prototype e-textile sock. In *2019 41st Annual International Conference of the IEEE Engineering in Medicine and Biology Society (EMBC)*, pages 17498–1752, 2019. doi: 10.1109/EMBC.2019.8856739.

[199] Giovanni Diraco, Gabriele Rescio, Pietro Siciliano, and Alessandro Leone. Review on Human Action Recognition in Smart Living: Sensing Technology, Multimodality, Real-Time Processing, Interoperability, and Resource-Constrained Processing. *Sensors*, 23(11), 2023. ISSN 14248220. doi: 10.3390/s23115281.

[200] Gaetano Pagano, Leandro Donisi, Vito Marsico, Ernesto Losavio, Mario Cesarelli, and Giovanni D'Addio. Reliability of kinematic parameters related to the timed up and go test in patients with gait impairments. In *2021 IEEE International Symposium on Medical Measurements and Applications (MeMeA)*, pages 1–5, 2021. doi: 10.1109/MeMeA52024.2021.9478762.

[201] Gait abnormalities 25 gaits. URL https://stanfordmedicine25.stanford.edu/the25/gait.html.

[202] Milagros Jaén-Vargas, Karla Miriam Reyes Leiva, Francisco Fernandes, Sérgio Barroso Goncalves, Miguel Tavares Silva, Daniel Simões Lopes, and José Javier Serrano Olmedo. Effects of sliding window variation in the performance of acceleration-based human activity recognition using deep learning models. *PeerJ Computer Science*, 8: 1–22, 2022. ISSN 23765992. doi: 10.7717/PEERJ-CS.1052.

[203] Giovanni Diraco, Gabriele Rescio, Andrea Caroppo, Andrea Manni, and Alessandro Leone. Human Action Recognition in Smart Living Services and Applications: Context Awareness, Data Availability, Personalization, and Privacy. *Sensors*, 23(13), 2023. ISSN 14248220. doi: 10.3390/s23136040.

[204] Elena Sibilano, Domenico Buongiorno, Michael Lassi, Antonello Grippo, Valentina Bessi, Sandro Sorbi, Alberto Mazzoni, Vitoantonio Bevilacqua, and Antonio Brunetti. Understanding the role of self-attention in a transformer model for the discrimination of scd from mci using resting-state eeg. *IEEE Journal of Biomedical and Health Informatics*, 28(6):3422–3433, 2024. doi: 10.1109/JBHI.2024.3390606.

[205] Antonio Brunetti, Domenico Buongiorno, Nicola Altini, and Vitoantonio Bevilacqua. Enabling technologies for optimized diagnosis, therapy and rehabilitation: Obtained results and future works. In Mario Bochicchio, Pietro Siciliano, Andrea Monteriù, Alice Bettelli, and Domenico De Fano, editors, *Ambient Assisted Living*, pages 206–223, Cham, 2024. Springer Nature Switzerland. ISBN 978-3-031-63913-5.

[206] Eduardo Casilari, Moisés Álvarez Marco, and Francisco García-Lagos. A study of the use of gyroscope measurements in wearable fall detection systems. *Symmetry*, 12 (4), 2020. ISSN 2073-8994. doi: 10.3390/sym12040649. URL https://www.mdpi.com/2073-8994/12/4/649.

[207] Ana-Cosmina Popescu, Irina Mocanu, and Bogdan Cramariuc. Fusion mechanisms for human activity recognition using automated machine learning. *IEEE Access*, 8: 143996–144014, 2020. doi: 10.1109/ACCESS.2020.3013406.

[208] Saurabh Sawant and Anurag Singh. Malaria cell detection using deep neural networks. *arXiv preprint arXiv:2406.20005*, 2024.

[209] Huy Q Vo, Pietro A Cicalese, Surya Seshan, Syed A Rizvi, Aneesh Vathul, Gloria Bueno, Anibal Pedraza Dorado, Niels Grabe, Katharina Stolle, Francesco Pesce, et al. Segmentation of diagnostic tissue compartments on whole slide images with renal thrombotic microangiopathies (tmas). *arXiv preprint arXiv:2311.14971*, 2023.

[210] Usamah Rashid Qureshi, Aiman Rashid, Nicola Altini, Vitoantonio Bevilacqua, and Massimo La Scala. Radiometric infrared thermography of solar photovoltaic systems: An explainable predictive maintenance approach for remote aerial diagnostic monitoring. *Smart Cities*, 7(3):1261–1288, 2024. ISSN 2624-6511. doi: 10.3390/smartcities7030053. URL https://www.mdpi.com/2624-6511/7/3/53.

[211] Domenico Buongiorno, Michela Prunella, Stefano Grossi, Sardar Mehboob Hussain, Alessandro Rennola, Nicola Longo, Giovanni Di Stefano, Vitoantonio Bevilacqua, and Antonio Brunetti. Inline defective laser weld identification by processing thermal image sequences with machine and deep learning techniques. *Applied Sciences*, 12(13), 2022. ISSN 2076-3417. doi: 10.3390/app12136455. URL https://www.mdpi.com/2076-3417/12/13/6455.

[212] Ismael Espinoza Jaramillo, Jin Gyun Jeong, Patricio Rivera Lopez, Choong-Ho Lee, Do-Yeon Kang, Tae-Jun Ha, Ji-Heon Oh, Hwanseok Jung, Jin Hyuk Lee, Won Hee Lee, and Tae-Seong Kim. Real-time human activity recognition with imu and encoder sensors in wearable exoskeleton robot via deep learning networks. *Sensors*, 22(24), 2022. ISSN 1424-8220. doi: 10.3390/s22249690. URL https://www.mdpi.com/1424-8220/22/24/9690.

[213] Cristian Camardella, Francesco Porcini, Alessandro Filippeschi, Simone Marcheschi, Massimiliano Solazzi, and Antonio Frisoli. Gait phases blended control for enhancing transparency on lower-limb exoskeletons. *IEEE Robotics and Automation Letters*, 6(3): 5453–5460, 2021. doi: 10.1109/LRA.2021.3075368.

[214] Vittorio Lippi, Alessandro Filippeschi, Cristian Camardella, Francesco Porcini, Christoph Maurer, and Lucia Lencioni. Exosmooth: Test of innovative exoskeleton control for smooth assistance, with and without ankle actuation. In *2022 17th ACM/IEEE International Conference on Human-Robot Interaction (HRI)*, pages 890–894, 2022. doi: 10.1109/HRI53351.2022.9889378.

[215] Vittorio Lippi, Cristian Camardella, Alessandro Filippeschi, and Francesco Porcini. Identification of gait phases with neural networks for smooth transparent control of a lower limb exoskeleton. *Proceedings of the 18th International Conference on Informatics*

in Control, Automation and Robotics, ICINCO 2021, pages 171–178, 2021. doi: 10.5220/0010554401710178.

[216] Cristian Camardella, Vittorio Lippi, Francesco Porcini, Giulia Bassani, Lucia Lencioni, Christoph Mauer, Christian Haverkamp, Carlo Alberto Avizzano, Antonio Frisoli, and Alessandro Filippeschi. User-centered evaluation of the Wearable Walker lower limb exoskeleton, preliminary assessment based on the Experience protocol. pages 1–12, 2024. ISSN 14248220. doi: 10.3390/s24165358. URL http://arxiv.org/abs/2408.08734.

[217] Domenico Chiaradia, Gianluca Rinaldi, Massimiliano Solazzi, Rocco Vertechy, and Antonio Frisoli. Design and control of the rehab-exos, a joint torque-controlled upper limb exoskeleton. *Robotics*, 13(2), 2024. ISSN 2218-6581. doi: 10.3390/robotics13020032. URL https://www.mdpi.com/2218-6581/13/2/32.

[218] Gianluca Rinaldi, Luca Tiseni, Michele Xiloyannis, Lorenzo Masia, Antonio Frisoli, and Domenico Chiaradia. Flexos: A portable, sea-based shoulder exoskeleton with hyper-redundant kinematics for weight lifting assistance. In *2023 IEEE World Haptics Conference (WHC)*, pages 252–258. IEEE, 2023. URL https://www.doi.org/10.1109/WHC56415.2023.10224485.

[219] Nicola Lotti, Michele Xiloyannis, Francesco Missiroli, Domenico Chiaradia, Antonio Frisoli, Vittorio Sanguineti, and Lorenzo Masia. Intention-detection strategies for upper limb exosuits: model-based myoelectric vs dynamic-based control. In *2020 8th IEEE RAS/EMBS International Conference for Biomedical Robotics and Biomechatronics (BioRob)*, pages 410–415, 2020. doi: 10.1109/BioRob49111.2020.9224284.

[220] Hung Nguyen, Karina Lebel, Patrick Boissy, Sarah Bogard, Etienne Goubault, and Christian Duval. Auto detection and segmentation of daily living activities during a timed up and go task in people with parkinson's disease using multiple inertial sensors. *Journal of NeuroEngineering and Rehabilitation*, 14(1):26, Apr 2017. ISSN 1743-0003. doi: 10.1186/s12984-017-0241-2. URL https://doi.org/10.1186/s12984-017-0241-2.

[221] Giovanni Diraco, Andrea Manni, and Alessandro Leone. Integrating Abnormal Gait Detection with Activities of Daily Living Monitoring in Ambient Assisted Living: A 3D Vision Approach. *Sensors*, 24(1), 2024. ISSN 14248220. doi: 10.3390/s24010082.

[222] R. B. Stein and M. N. Oğuztöreli. Tremor and other oscillations in neuromuscular systems. *Biological Cybernetics*, 22(3):147–157, Sep 1976. ISSN 1432-0770. doi: 10.1007/BF00365525. URL https://doi.org/10.1007/BF00365525.

[223] Pierre R Burkhard, J.William Langston, and James W Tetrud. Voluntarily simulated tremor in normal subjects. *Neurophysiologie Clinique/Clinical Neurophysiology*, 32(2):119–126, 2002. ISSN 0987-7053. doi: https://doi.org/10.1016/S0987-7053(02)00296-4. URL https://www.sciencedirect.com/science/article/pii/S0987705302002964.

[224] Lei Wang, Yun Sun, Qingguo Li, Tao Liu, and Jingang Yi. Imu-based gait normalcy index calculation for clinical evaluation of impaired gait. *IEEE Journal of Biomedical and Health Informatics*, 25(1):3–12, 2021. doi: 10.1109/JBHI.2020.2982978.

[225] Jungi Kim, Haneol Seo, Muhammad Tahir Naseem, and Chan-Su Lee. Pathological-gait recognition using spatiotemporal graph convolutional networks and attention model. *Sensors*, 22(13), 2022. ISSN 1424-8220. doi: 10.3390/s22134863. URL https://www.mdpi.com/1424-8220/22/13/4863.

[226] Fabian Horst, Sebastian Lapuschkin, Wojciech Samek, Klaus-Robert Müller, and Wolfgang I Schöllhorn. What is unique in individual gait patterns? understanding and interpreting deep learning in gait analysis. *arXiv*, 2018.

[227] J. de Kok, P. Vroonhof, J. Snijders, and G. Roullis et al. Work-related msds: prevalence, costs and demographics in the eu. Technical report, European Agency for Safety and Health at Work, 2019.

[228] Feng Yang, Niu Di, Wei-wei Guo, Wen-bin Ding, Ning Jia, Hengdong Zhang, Dongxia Li, Dayu Wang, Rugang Wang, Danying Zhang, et al. The prevalence and risk factors of work related musculoskeletal disorders among electronics manufacturing workers: a cross-sectional analytical study in china. *BMC Public Health*, 23(1):10, 2023. URL https://doi.org/10.1186/s12889-022-14952-6.

[229] Kirsten Huysamen, Tim Bosch, Michiel de Looze, Konrad S. Stadler, Eveline Graf, and Leonard W. O'Sullivan. Evaluation of a passive exoskeleton for static upper limb activities. *Applied Ergonomics*, 70:148–155, 2018. URL https://doi.org/10.1016/j.apergo.2018.02.009.

[230] Muhammad Ahsan Gull, Shaoping Bai, and Thomas Bak. A review on design of upper limb exoskeletons. *Robotics*, 9(1):16, 2020. URL https://doi.org/10.3390/robotics9010016.

[231] Simona Crea, Philipp Beckerle, Michiel De Looze, Kevin De Pauw, Lorenzo Grazi, Tjaša Kermavnar, Jawad Masood, Leonard W O'Sullivan, Ilaria Pacifico, Carlos Rodriguez-Guerrero, et al. Occupational exoskeletons: A roadmap toward large-scale adoption. methodology and challenges of bringing exoskeletons to workplaces. *Wearable Technologies*, 2:e11, 2021. URL https://doi.org/10.1017/wtc.2021.11.

[232] Christian Weckenborg, Christian Thies, and Thomas S Spengler. Harmonizing ergonomics and economics of assembly lines using collaborative robots and exoskeletons. *Journal of Manufacturing Systems*, 62:681–702, 2022. URL https://doi.org/10.1016/j.jmsy.2022.02.005.

[233] Johannes Sänger, Zhejun Yao, Tim Schubert, Alexander Wolf, Carla Molz, Jörg Miehling, Sandro Wartzack, Thomas Gwosch, Sven Matthiesen, and Robert Weidner. Evaluation of active shoulder exoskeleton support to deduce application-oriented optimization potentials for overhead work. *Applied Sciences*, 12(21):10805, 2022.

[234] Pauline Maurice, Jernej Čamernik, Daša Gorjan, Benjamin Schirrmeister, Jonas Bornmann, Luca Tagliapietra, Claudia Latella, Daniele Pucci, Lars Fritzsche, Serena Ivaldi, et al. Objective and subjective effects of a passive exoskeleton on overhead work. *IEEE Transactions on Neural Systems and Rehabilitation Engineering*, 28(1):152–164, 2019. URL https://doi.org/10.1109/TNSRE.2019.2945368.

[235] Lorenzo Grazi, Emilio Trigili, Giulio Proface, Francesco Giovacchini, Simona Crea, and Nicola Vitiello. Design and experimental evaluation of a semi-passive upper-limb exoskeleton for workers with motorized tuning of assistance. *IEEE Transactions on Neural Systems and Rehabilitation Engineering*, 28(10):2276–2285, 2020. URL https://doi.org/10.1016/10.1109/TNSRE.2020.3014408.

[236] Ilaria Pacifico, Federica Aprigliano, Andrea Parri, Giusi Cannillo, Ilaria Melandri, Angelo Maria Sabatini, Francesco Saverio Violante, Franco Molteni, Francesco Giovacchini, Nicola Vitiello, and Simona Crea. Evaluation of a spring-loaded upper-limb exoskeleton in cleaning activities. *Applied Ergonomics*, 106:103877, 2023. ISSN 0003-6870. doi: https://doi.org/10.1016/j.apergo.2022.103877. URL https://www.sciencedirect.com/science/article/pii/S0003687022002009.

[237] Annina Brunner, Rachel van Sluijs, Volker Bartenbach, Dario Bee, Melanie Kos, Lijin Aryananda, and Olivier Lambercy. Effect of a passive shoulder support exoskeleton on fatigue during working with arms over shoulder level. In Daniela Tarnita, Nicolae Dumitru, Doina Pisla, Giuseppe Carbone, and Ionut Geonea, editors, *New Trends in Medical and Service Robotics*, pages 188–197, Cham, 2023. Springer Nature Switzerland. ISBN 978-3-031-32446-8.

[238] Gianluca Rinaldi, Vladimiro Suglia, Luca Tiseni, Cristian Camardella, Michele Xyloyannis, Lorenzo Masia, Domenico Buongiorno, Vitoantonio Bevilacqua, Antonio Frisoli, and Domenico Chiaradia. Towards a healthier workplace: how flexos, an active and bilateral shoulder exoskeleton, provides support in weight-lifting and carrying tasks. *Submitted to IEEE Transactions on Robotics*, 2024.

[239] Vladimiro Suglia, Cristian Camardella, Gianluca Rinaldi, Domenico Chiaradia, Domenico Buongiorno, Hui Zhou, Antonio Frisoli, Daniele Leonardis, and Vitoantonio Bevilacqua. Muscle networks analysis on an active occupational shoulder exoskeleton. *Submitted to IEEE Transactions on Human-Machine Systems*, 2024.

[240] A. Blanco, J. M. Catalán, D. Martínez-Pascual, J. V. García-Pérez, and N. García-Aracil. The effect of an active upper-limb exoskeleton on metabolic parameters and muscle activity during a repetitive industrial task. *IEEE Access*, 10:16479–16488, 2022. ISSN 2169-3536. URL https://doi.org/10.1109/ACCESS.2022.3150104.

[241] Lorenzo Grazi, Emilio Trigili, Noemi Caloi, Giulia Ramella, Francesco Giovacchini, Nicola Vitiello, and Simona Crea. Kinematics-based adaptive assistance of a semi-passive upper-limb exoskeleton for workers in static and dynamic tasks. *IEEE Robotics*

and Automation Letters, 7(4):8675–8682, 2022. URL https://doi.org/10.1109/LRA.2022.3188402.

[242] Yu Meng Zhou, Cameron Hohimer, Tommaso Proietti, Ciarán Tomás O'Neill, and Conor J Walsh. Kinematics-based control of an inflatable soft wearable robot for assisting the shoulder of industrial workers. *IEEE Robotics and Automation Letters*, 6 (2):2155–2162, 2021. URL https://doi.org/10.1109/LRA.2021.3061365.

[243] Yongtae G. Kim, Michele Xiloyannis, Dino Accoto, and Lorenzo Masia. Development of a soft exosuit for industrial applications. In *2018 7th IEEE International Conference on Biomedical Robotics and Biomechatronics (Biorob)*, pages 324–329, 2018. URL https://doi.org/10.1109/BIOROB.2018.8487907.

[244] Armando Coccia, Edda Maria Capodaglio, Federica Amitrano, Vittorio Gabba, Monica Panigazzi, Gaetano Pagano, and Giovanni D'Addio. Biomechanical effects of using a passive exoskeleton for the upper limb in industrial manufacturing activities: A pilot study. *Sensors*, 24(5), 2024. ISSN 1424-8220. URL https://www.mdpi.com/1424-8220/24/5/1445.

[245] Jean Theurel, Kevin Desbrosses, Terence Roux, and Adriana Savescu. Physiological consequences of using an upper limb exoskeleton during manual handling tasks. *Applied ergonomics*, 67:211–217, 2018. URL https://doi.org/10.1016/j.apergo.2017.10.008.

[246] Sander De Bock, Marco Rossini, Dirk Lefeber, Carlos Rodriguez-Guerrero, Joost Geeroms, Romain Meeusen, and Kevin De Pauw. An occupational shoulder exoskeleton reduces muscle activity and fatigue during overhead work. *IEEE Transactions on Biomedical Engineering*, 69(10):3008–3020, 2022. URL https://www.doi.org/10.1109/TBME.2022.3159094.

[247] Adriana Cancrini, Paolo Baitelli, Matteo Lavit Nicora, Matteo Malosio, Alessandra Pedrocchi, and Alessandro Scano. The effects of robotic assistance on upper limb spatial muscle synergies in healthy people during planar upper-limb training. *PLOS ONE*, 17 (8):1–25, 08 2022. doi: 10.1371/journal.pone.0272813. URL https://www.doi.org/10.1371/journal.pone.0272813.

[248] A. Scano, A. Chiavenna, M. Caimmi, M. Malosio, L. M. Tosatti, and F. Molteni. Effect of human-robot interaction on muscular synergies on healthy people and post-stroke chronic patients. In *2017 International Conference on Rehabilitation Robotics (ICORR)*, pages 527–532, 2017. doi: 10.1109/ICORR.2017.8009302.

[249] Simon Christensen, Shaoping Bai, Sajid Rafique, Magnus Isaksson, Leonard O'Sullivan, Valerie Power, and Gurvinder Singh Virk. Axo-suit-a modular full-body exoskeleton for physical assistance. In *IFToMM Symposium on Mechanism Design for Robotics*, pages 443–450. Springer, 2018. URL https://doi.org/10.1007/978-3-030-00365-4_52.

[250] Anna-Maria Georgarakis, Michele Xiloyannis, Peter Wolf, and Robert Riener. A textile exomuscle that assists the shoulder during functional movements for everyday life. *Nature Machine Intelligence*, 4(6):574–582, 2022. URL https://doi.org/10.1038/s42256-022-00495-3.

[251] Nicola Lotti, Michele Xiloyannis, Francesco Missiroli, Casimir Bokranz, Domenico Chiaradia, Antonio Frisoli, Robert Riener, and Lorenzo Masia. Myoelectric or force control? a comparative study on a soft arm exosuit. *IEEE Transactions on Robotics*, 38(3): 1363–1379, 2022. URL https://doi.org/https://www.doi.org/10.1109/TRO.2021.3137748.

[252] Michele Xiloyannis, Ryan Alicea, Anna-Maria Georgarakis, Florian L Haufe, Peter Wolf, Lorenzo Masia, and Robert Riener. Soft robotic suits: State of the art, core technologies, and open challenges. *IEEE Transactions on Robotics*, 2021. URL https://www.doi.org/10.1109/TRO.2021.3084466.

[253] Domenico Chiaradia, Luca Tiseni, Michele Xiloyannis, Massimiliano Solazzi, Lorenzo Masia, and Antonio Frisoli. An assistive soft wrist exosuit for flexion movements with an ergonomic reinforced glove. *Frontiers in Robotics and AI*, 7:595862, 2021. URL https://doi.org/10.3389/frobt.2020.595862.

[254] Anthony Voilqué, Jawad Masood, JC Fauroux, Laurent Sabourin, and Olivier Guezet. Industrial exoskeleton technology: classification, structural analysis, and structural complexity indicator. In *2019 Wearable Robotics Association Conference (WearRAcon)*, pages 13–20. IEEE, 2019. URL https::/www.doi.org/10.1109/WEARRACON.2019.8719395.

[255] Mate by comau. https://mate.comau.com/, Last accessed on 2023-02-04.

[256] Skelex. https://www.skelex.com/, Last accessed on 2023-02-04.

[257] Max by suit x. https://www.suitx.com/, Last accessed on 2023-02-04.

[258] Ergosquelettes. https://gobio-robot.com/, Last accessed on 2023-02-04.

[259] Gill A Pratt and Matthew M Williamson. Series elastic actuators. In *Proceedings 1995 IEEE/RSJ International Conference on Intelligent Robots and Systems. Human Robot Interaction and Cooperative Robots*, volume 1, pages 399–406. IEEE, 1995. URL https://doi.org/10.1109/IROS.1995.525827.

[260] Cristian Camardella, Michele Barsotti, Domenico Buongiorno, Antonio Frisoli, and Vitoantonio Bevilacqua. Towards online myoelectric control based on muscle synergies-to-force mapping for robotic applications. *Neurocomputing*, 452:768–778, 2021. ISSN 0925-2312. URL https://doi.org/10.1016/j.neucom.2020.08.081.

[261] Domenico Buongiorno, Michele Barsotti, Edoardo Sotgiu, Claudio Loconsole, Massimiliano Solazzi, Vitoantonio Bevilacqua, and Antonio Frisoli. A neuromusculoskeletal model of the human upper limb for a myoelectric exoskeleton control using a reduced

number of muscles. In *2015 IEEE World Haptics Conference (WHC)*, pages 273–279, 2015. URL https://www.doi.org/10.1109/WHC.2015.7177725.

[262] Amir Ebrahimi. Stuttgart exo-jacket: An exoskeleton for industrial upper body applications. In *2017 10th International Conference on Human System Interactions (HSI)*, pages 258–263. IEEE, 2017. URL https://doi.org/10.1109/HSI.2017.8005042.

[263] Luca Tiseni, Michele Xiloyannis, Domenico Chiaradia, Nicola Lotti, Massimiliano Solazzi, Herman Van der Kooij, Antonio Frisoli, and Lorenzo Masia. On the edge between soft and rigid: an assistive shoulder exoskeleton with hyper-redundant kinematics. In *2019 IEEE 16th International Conference on Rehabilitation Robotics (ICORR)*, pages 618–624. IEEE, 2019. URL https://www.doi.org/10.1109/ICORR.2019.8779546.

[264] Luca Tiseni, Gianluca Rinaldi, Domenico Chiaradia, and Antonio Frisoli. Design and control of a linear springs-based rotary series elastic actuator for portable assistive exoskeletons. In *2021 30th IEEE International Conference on Robot & Human Interactive Communication (RO-MAN)*, pages 434–439, 2021. URL https://doi.org/10.1109/RO-MAN50785.2021.9515444.

[265] Magdalena Żuk, Magdalena Wojtków, Michał Popek, Jakub Mazur, and Katarzyna Bulińska. Three-dimensional gait analysis using a virtual reality tracking system. *Measurement*, 188:110627, 2022. URL https://doi.org/10.1016/j.measurement.2021.110627.

[266] The seniam project (surface electromyography for the non- invasive assessment of muscles. http://www.seniam.org/, Last accessed on 2023-02-04.

[267] R. Merletti and D. Farina. *Myoelectric Manifestations of Muscle Fatigue*. John Wiley & Sons, Ltd, 2006. ISBN 9780471740360. URL https://onlinelibrary.wiley.com/doi/abs/10.1002/9780471740360.ebs1427.

[268] Francesco Missiroli, Nicola Lotti, Enrica Tricomi, Casimir Bokranz, Ryan Alicea, Michele Xiloyannis, Jens Krzywinski, Simona Crea, Nicola Vitiello, and Lorenzo Masia. Rigid, soft, passive, and active: A hybrid occupational exoskeleton for bimanual multijoint assistance. *IEEE Robotics and Automation Letters*, 7(2):2557–2564, 2022. URL https://doi.org/10.1109/LRA.2022.3142447.

[269] Ehsan Rashedi, Sunwook Kim, Maury A Nussbaum, and Michael J Agnew. Ergonomic evaluation of a wearable assistive device for overhead work. *Ergonomics*, 57(12):1864–1874, 2014. URL https://doi.org/10.1080/00140139.2014.952682.

[270] Sandra G. Hart. Nasa-task load index (nasa-tlx); 20 years later. *Proceedings of the Human Factors and Ergonomics Society Annual Meeting*, 50(9):904–908, 2006. doi: 10.1177/154193120605000909. URL https://doi.org/10.1177/154193120605000909.

[271] Gunnar Borg. Psychophysical scaling with applications in physical work and the perception of exertion. *Scandinavian Journal of Work, Environment & Health*, 16:55–58, 2024/04/10/ 1990. URL http://www.jstor.org/stable/40965845.

[272] Ge Wu, F.C.T. van der Helm, H.E.J. (Dirkjan) Veeger, Mohsen Makhsous, Peter Van Roy, Carolyn Anglin, Jochem Nagels, Andrew R. Karduna, Kevin McQuade, Xuguang Wang, Frederick W. Werner, and Bryan Buchholz. Isb recommendation on definitions of joint coordinate systems of various joints for the reporting of human joint motion–part ii: shoulder, elbow, wrist and hand. *Journal of Biomechanics*, 38,5: 981–992, 2005. URL https://doi.org/10.1016/j.jbiomech.2004.05.042.

[273] Donna C Boone and Stanley P Azen. Normal range of motion of joints in male subjects. *JBJS*, 61(5):756–759, 1979.

[274] Ilaria Pacifico, Alessandro Scano, Eleonora Guanziroli, Matteo Moise, Luca Morelli, Andrea Chiavenna, Duane Romo, Stefania Spada, Giuseppe Colombina, Franco Molteni, et al. An experimental evaluation of the proto-mate: a novel ergonomic upper-limb exoskeleton to reduce workers' physical strain. *IEEE Robotics & Automation Magazine*, 27(1):54–65, 2020. URL https::/www.doi.org/10.1109/MRA.2019.2954105.

[275] Talita Pinto, Fabio dos Anjos, Taian Vieira, Giacinto Luigi Cerone, Rachele Sessa, Fabrizio Caruso, Gabriele Caragnano, Francesco Saverio Violante, and Marco Gazzoni. The effect of passive exoskeleton on shoulder muscles activity during different static tasks. In Tomaz Jarm, Aleksandra Cvetkoska, Samo Mahnič-Kalamiza, and Damijan Miklavcic, editors, *8th European Medical and Biological Engineering Conference*, pages 1087–1091, Cham, 2021. Springer International Publishing. ISBN 978-3-030-64610-3. URL https://doi.org/10.1007/978-3-030-64610-3_122.

[276] Hyun-Ho Lee, Kyung-Taek Yoon, Hyun-Ho Lim, Won-Kyu Lee, Jae-Hwan Jung, Seung-Beom Kim, and Young-Man Choi. A novel passive shoulder exoskeleton using link chains and magnetic spring joints. *IEEE Transactions on Neural Systems and Rehabilitation Engineering*, 32:708–717, 2024. URL https://www.doi.org/10.1109/TNSRE.2024.3359658.

[277] Domenico Buongiorno, Edoardo Sotgiu, Daniele Leonardis, Simone Marcheschi, Massimiliano Solazzi, and Antonio Frisoli. Wres: A novel 3 dof wrist exoskeleton with tendon-driven differential transmission for neuro-rehabilitation and teleoperation. *IEEE Robotics and Automation Letters*, 3(3):2152–2159, 2018. URL https://www.doi.org/10.1109/LRA.2018.2810943.

[278] C. Camardella, M. Germanotta, I. Aprile, G. Cappiello, Z. Curto, A. Scoglio, S. Mazzoleni, and A. Frisoli. A decision support system to provide an ongoing prediction of robot-assisted rehabilitation outcome in stroke survivors. In *2023 International Conference on Rehabilitation Robotics (ICORR)*, pages 1–6, 2023. URL https://www.doi.org/10.1109/ICORR58425.2023.10304700.

[279] Greta Vazzoler, Cristian Camardella, Massimiliano Gabardi, Simone Marcheschi, Massimiliano Solazzi, Giovanni Berselli, and Antonio Frisoli. Evaluating efficacy of continuous assistance control during orientation tasks with an active wrist exoskeleton.

In *2023 21st International Conference on Advanced Robotics (ICAR)*, pages 545–550. IEEE, 2023.

[280] Cristian Camardella, Vittorio Lippi, Francesco Porcini, Giulia Bassani, Lucia Lencioni, Christoph Mauer, Christian Haverkamp, Carlo Alberto Avizzano, Antonio Frisoli, and Alessandro Filippeschi. User-centered evaluation of the wearable walker lower limb exoskeleton; preliminary assessment based on the experience protocol. *Sensors (Basel, Switzerland)*, 24(16), 2024.

[281] *Positive Feedback in Powered Exoskeletons: Improved Metabolic Efficiency at the Cost of Reduced Stability?*, volume Volume 5: 6th International Conference on Multibody Systems, Nonlinear Dynamics, and Control, Parts A, B, and C of *International Design Engineering Technical Conferences and Computers and Information in Engineering Conference*, 09 2007. doi: 10.1115/DETC2007-35657. URL https://doi.org/10.1115/DETC2007-35657.

[282] Elvira Pirondini, Martina Coscia, Simone Marcheschi, Gianluca Roas, Fabio Salsedo, Antonio Frisoli, Massimo Bergamasco, and Silvestro Micera. Evaluation of the effects of the arm light exoskeleton on movement execution and muscle activities: a pilot study on healthy subjects. *Journal of neuroengineering and rehabilitation*, 13:1–21, 2016.

[283] Andrea d'Avella, Philippe Saltiel, and Emilio Bizzi. Combinations of muscle synergies in the construction of a natural motor behavior. *Nature neuroscience*, 6(3):300–308, 2003.

[284] Vincent CK Cheung, Andrea Turolla, Michela Agostini, Stefano Silvoni, Caoimhe Bennis, Patrick Kasi, Sabrina Paganoni, Paolo Bonato, and Emilio Bizzi. Muscle synergy patterns as physiological markers of motor cortical damage. *Proceedings of the national academy of sciences*, 109(36):14652–14656, 2012.

[285] Jinsook Roh, William Z Rymer, and Randall F Beer. Evidence for altered upper extremity muscle synergies in chronic stroke survivors with mild and moderate impairment. *Frontiers in human neuroscience*, 9:124339, 2015.

[286] A. Scano, A. Chiavenna, M. Caimmi, M. Malosio, L. M. Tosatti, and F. Molteni. Effect of human-robot interaction on muscular synergies on healthy people and post-stroke chronic patients. In *2017 International Conference on Rehabilitation Robotics (ICORR)*, pages 527–532, 2017. doi: 10.1109/ICORR.2017.8009302.

[287] Tjeerd W. Boonstra, Alessander Danna-Dos-Santos, Hong-Bo Xie, Melvyn Roerdink, John F. Stins, and Michael Breakspear. Muscle networks: Connectivity analysis of emg activity during postural control. *Scientific Reports*, 5(1):17830, Dec 2015. ISSN 2045-2322. doi: 10.1038/srep17830.

[288] Pascal Fries. A mechanism for cognitive dynamics: neuronal communication through neuronal coherence. *Trends in Cognitive Sciences*, 9(10):474–480, Oct 2005. ISSN 1364-6613. doi: 10.1016/j.tics.2005.08.011. URL https://doi.org/10.1016/j.tics.2005.08.011.

[289] Tjeerd W Boonstra. The potential of corticomuscular and intermuscular coherence for research on human motor control, 2013.

[290] Rory O'Keeffe, Seyed Yahya Shirazi, Sarmad Mehrdad, Tyler Crosby, Aaron M. Johnson, and S. Farokh Atashzar. Perilaryngeal-cranial functional muscle network differentiates vocal tasks: A multi-channel semg approach. *IEEE Transactions on Biomedical Engineering*, 69(12):3678–3688, 2022. URL https://www.doi.org/10.1109/TBME.2022.3175948.

[291] P Brown. Cortical drives to human muscle: the piper and related rhythms. *Progress in Neurobiology*, 60(1):97–108, 2000. ISSN 0301-0082. URL https://doi.org/10.1016/S0301-0082(99)00029-5.

[292] Rory O'Keeffe, Jinghui Yang, Sarmad Mehrdad, Smita Rao, and S. Farokh Atashzar. Lower-limb non-parametric functional muscle network: Test-retest reliability analysis. *IEEE Transactions on Neural Systems and Rehabilitation Engineering*, 31:2953–2963, 2023. URL https://www.doi.org/10.1109/TNSRE.2023.3291748.

[293] Tie Liang, Huacong Miao, Hongrui Wang, Xiaoguang Liu, and Xiuling Liu. Surface electromyography-based analysis of the lower limb muscle network and muscle synergies at various gait speeds. *IEEE Transactions on Neural Systems and Rehabilitation Engineering*, 31:1230–1237, 2023. doi: 10.1109/TNSRE.2023.3242911.

[294] Yuejiang Luo, Tianxiao Guo, Rui Wang, Siqi Mu, and Kuan Tao. Decoding invariant spatiotemporal synergy patterns on muscle networks of lower-limb movements via surface electromyographic signals. *Biomedical Signal Processing and Control*, 91:106033, 2024. ISSN 1746-8094. URL https://doi.org/10.1016/j.bspc.2024.106033.

[295] Jennifer N. Kerkman, Coen S. Zandvoort, Andreas Daffertshofer, and Nadia Dominici. Body weight control is a key element of motor control for toddlers' walking. *Frontiers in Network Physiology*, 2, 2022. ISSN 2674-0109. doi: 10.3389/fnetp.2022.844607.

[296] Xiaoguang Liu, Boxiong Yang, Tie Liang, Jun Li, Cunguang Lou, Hongrui Wang, and Xiuling Liu. Muscle compensation analysis during motion based on muscle functional network. *IEEE Sensors Journal*, 22(3):2370–2378, 2022. doi: 10.1109/JSEN.2021.3131320.

[297] Hao Guo, Peihao Gong, Yiming Wang, Fei Qi, Chunguang Li, Juan Li, and Lining Sun. Complex network properties analysis of muscle fatigue based on semg signals. *IEEE Sensors Journal*, 23(4):3859–3869, 2023. doi: 10.1109/JSEN.2022.3233047.

[298] BINGYU PAN and TIANSHU LIU. Coherence networks of bilateral upper limb motions in chronic stroke patients. *Journal of Mechanics in Medicine and Biology*, 23(02):2350024, 2023. doi: 10.1142/S0219519423500240.

[299] Michael Houston, Xiaoyan Li, Ping Zhou, Sheng Li, Jinsook Roh, and Yingchun Zhang. Alterations in muscle networks in the upper extremity of chronic stroke survivors.

IEEE Transactions on Neural Systems and Rehabilitation Engineering, 29:1026–1034, 2021. doi: 10.1109/TNSRE.2021.3075907.

[300] Jinping Li, Ying Hou, Juan Wang, Huitian Zheng, Chengfan Wu, Na Zhang, and Ke Li. Functional muscle network in post-stroke patients during quiet standing. In *2021 43rd Annual International Conference of the IEEE Engineering in Medicine & Biology Society (EMBC)*, pages 874–877, 2021. doi: 10.1109/EMBC46164.2021.9630003.

[301] Francesca Sylos-Labini, Valentina La Scaleia, Germana Cappellini, Arthur Dewolf, Adele Fabiano, Irina A. Solopova, Vito Mondì, Yury Ivanenko, and Francesco Lacquaniti. Complexity of modular neuromuscular control increases and variability decreases during human locomotor development. *Communications Biology*, 5 (1):1256, Nov 2022. ISSN 2399-3642. doi: 10.1038/s42003-022-04225-8. URL https://doi.org/10.1038/s42003-022-04225-8.

[302] Kunkun Zhao, Yizhou Feng, Liang Li, Yuxuan Zhou, Zhisheng Zhang, and Jianqing Li. Muscle synergies and muscle networks in multiple frequency components in post-stroke patients. *Biomedical Signal Processing and Control*, 95:106417, 2024. ISSN 1746-8094. URL https://doi.org/10.1016/j.bspc.2024.106417.

[303] Jennifer N. Kerkman, Andreas Daffertshofer, Leonardo L. Gollo, Michael Breakspear, and Tjeerd W. Boonstra. Network structure of the human musculoskeletal system shapes neural interactions on multiple time scales. *Science Advances*, 4(6):eaat0497, 2018. doi: 10.1126/sciadv.aat0497.

[304] Tjeerd W. Boonstra and Michael Breakspear. Neural mechanisms of intermuscular coherence: implications for the rectification of surface electromyography. *Journal of Neurophysiology*, 107(3):796–807, 2012. doi: 10.1152/jn.00066.2011.

[305] Nicholas J Ward, Simon F Farmer, Luc Berthouze, and David M Halliday. Rectification of emg in low force contractions improves detection of motor unit coherence in the beta-frequency band. *Journal of neurophysiology*, 110(8):1744–1750, 2013.

[306] Daniel D Lee and H Sebastian Seung. Learning the parts of objects by non-negative matrix factorization. *nature*, 401(6755):788–791, 1999.

[307] Domenico Buongiorno, Giacomo Donato Cascarano, Cristian Camardella, Irio De Feudis, Antonio Frisoli, and Vitoantonio Bevilacqua. Task-oriented muscle synergy extraction using an autoencoder-based neural model. *Information*, 11(4), 2020. ISSN 2078-2489. URL https://www.mdpi.com/2078-2489/11/4/219.

[308] Craig G. Mcdonald, Benjamin J. Fregly, and Marcia K. O'Malley. Effect of robotic exoskeleton motion constraints on upper limb muscle synergies: A case study. *IEEE Transactions on Neural Systems and Rehabilitation Engineering*, 29:2086–2095, 2021. doi: 10.1109/TNSRE.2021.3118591.

[309] Cristian Camardella, King Chun Tse, Antonio Frisoli, and Raymond Kai-Yu Tong. Investigating muscle synergies changes after rehabilitation robotics training on stroke survivors: a pilot study. In *2020 42nd Annual International Conference of the IEEE Engineering in Medicine & Biology Society (EMBC)*, pages 3731–3734, 2020. doi: 10.1109/EMBC44109.2020.9175726.

[310] Mikail Rubinov and Olaf Sporns. Complex network measures of brain connectivity: Uses and interpretations. *NeuroImage*, 52(3):1059–1069, 2010. ISSN 1053-8119. doi: https://doi.org/10.1016/j.neuroimage.2009.10.003. URL https://www.sciencedirect.com/science/article/pii/S105381190901074X. Computational Models of the Brain.

[311] Duncan J Watts and Steven H Strogatz. Collective dynamics of 'small-world'networks. *nature*, 393(6684):440–442, 1998.